



universität  
wien

# DISSERTATION / DOCTORAL THESIS

Titel der Dissertation /Title of the Doctoral Thesis

„Dislocation Mechanisms With Respect To Thermal  
Relaxation And Plastic Deformation In Semicrystalline  
Polymers“

verfasst von / submitted by

Mag. Gerald Polt

angestrebter akademischer Grad / in partial fulfilment of the requirements for the degree of  
Doktor der Naturwissenschaften (Dr. rer. nat)

Wien, 2016 / Vienna 2016

Studienkennzahl lt. Studienblatt /  
degree programme code as it appears on the student  
record sheet:

A 791 411

Dissertationsgebiet lt. Studienblatt /  
field of study as it appears on the student record sheet:

Physik

Betreut von / Supervisor:

ao. Univ.-Prof. Dr. Michael Zehetbauer



# Abstract

The present work focuses on the investigation and clarification of dislocation-based micromechanical processes being active at the yield and during the post-yield stage in semicrystalline polymers. In this context, the presence, density and interaction of dislocations is studied, particularly with respect to the properties of the amorphous phase and its interaction with the crystalline one. For the proof and the quantification of the dislocations as well as of the crystalline lamellae, a special X-ray diffraction method, called Multiple X-ray line Profile Analysis (MXPA), has been used.

In the first part of this thesis, the influence of the amorphous phase on dislocation kinetics was studied by means of in-situ heating experiments during simultaneous X-ray diffractometry in combination with the methods of the Dynamic Mechanical Analysis. This allowed to correlate the thermally induced changes of the dislocation density with those of the molecular relaxations. A second group of experiments consisted in in-situ compression MXPA tests below and beyond the glass temperature, thus selectively modifying the rigidity of the amorphous phase. Thereby also the rotational degrees of freedom of the crystalline lamellae could be systematically varied, thus allowing the investigation of different micromechanical deformation mechanisms.

A third goal of the work was to study the dislocation dynamics in Polyethylene during macroscopic plastic deformation. As the standard-MXPA methods fail here due to the low number of Bragg reflections, the so-called momentum method has been applied here for the first time to a semicrystalline polymer. As in the case of MXPA, this method allows to separate size from distortion effects and to uniquely attribute the latter to the presence of dislocations and/or to their multiplication during further deformation.



# Kurzfassung

Die vorliegende Arbeit befasst sich mit der Untersuchung und Aufklärung versetzungsbasierender mikromechanischer Prozesse, welche zu Beginn der plastischen Verformung und danach in semikristallinen Polymeren ablaufen. Dabei werden die Existenz, die Dichte und die Wechselwirkung der Versetzungen studiert, insbesondere hinsichtlich der Eigenschaften der amorphen Phase und deren Wechselwirkung mit der kristallinen Phase. Für den Nachweis und die Quantifizierung der Versetzungen als auch der Größe der kristallinen Lamellen wird eine spezielle Röntgendiffraktionsmethode, die sogenannte “Multiple X-ray line Profile Analysis (MXPA)“, eingesetzt.

Im ersten Teil der Arbeit wurde der Einfluss der amorphen Phase auf die Versetzungskinetik untersucht, mittels in-situ Aufheizexperimenten bei gleichzeitiger Röntgendiffraktometrie in Kombination mit den Methoden der Dynamisch-Mechanischen Analyse. Dadurch war es möglich, die thermisch induzierten Änderungen der Versetzungsdichte mit solchen der molekularen Relaxationsvorgänge zu korrelieren.

Der zweite Teil der Experimente bestand in der Durchführung von in-situ Kompressions-MXPA Tests unterhalb und oberhalb der Glasübergangstemperatur, womit die Steifigkeit der amorphen Phase selektiv beeinflusst wurde. Dadurch konnte auch der Rotations-Freiheitsgrad der kristallinen Lamellen systematisch variiert werden, was die Untersuchung unterschiedlicher mikromechanischer Verformungsmechanismen ermöglichte.

Ein drittes Ziel der Arbeit war das Studium der Versetzungsdynamik in Polyethylen während makroskopischer plastischer Verformung. Weil hier wegen der geringen Zahl von Bragg-Reflexen die Standard-MXPA Methoden versagen, wurde erstmals in einem semikristallinen Polymer die sogenannte “Momenten-Methode” angewandt. Ähnlich wie im Fall der MXPA ist diese Methode in der Lage, den Size-Effekt vom Verzerrungseffekt zu trennen und außerdem den letzteren eindeutig der Präsenz von verformungsinduzierten Versetzungen bzw. deren Vervielfachung bei fortgesetzter plastischer Verformung zuzuordnen.



# Contents

<b>1</b>	<b>Introduction</b>	<b>1</b>
<b>2</b>	<b>Aim of the thesis</b>	<b>3</b>
<b>3</b>	<b>Semicrystalline Polymers: State of the art</b>	<b>5</b>
3.1	Structure and Morphology . . . . .	5
3.2	Plasticity of Semicrystalline Polymers . . . . .	7
3.2.1	Deformation of the amorphous phase . . . . .	9
3.2.2	Deformation of the crystalline phase . . . . .	11
3.2.3	Deformation by dislocation motion . . . . .	15
3.3	Molecular relaxations in polymers . . . . .	21
3.3.1	Viscoelastic behaviour of polymers . . . . .	21
3.3.2	Molecular relaxations and transitions . . . . .	24
<b>4</b>	<b>Experimental Details and Methodology</b>	<b>27</b>
4.1	Sample preparation . . . . .	27
4.2	Differential scanning calorimetry (DSC) . . . . .	29
4.3	X-ray Line Profile Analysis . . . . .	30
4.3.1	MXPA and CMWP-fit . . . . .	30
4.3.2	Modified Williamson-Hall analysis . . . . .	31
4.3.3	Momentum-Method . . . . .	32
4.4	Synchrotron Experiments . . . . .	33
4.5	Data Pre-processing . . . . .	35
<b>5</b>	<b>Results</b>	<b>37</b>
5.1	Molecular relaxations occurring during annealing . . . . .	37
5.1.1	Polypropylene . . . . .	37
5.1.2	Polyethylene terephthalate (PET) . . . . .	43

5.2	Crystalline plasticity below and above the glass transition . . . . .	46
5.2.1	Application of the Momentum Method to PE . . . . .	50
<b>6</b>	<b>Discussion</b>	<b>53</b>
6.1	Molecular relaxations and dislocation kinetics . . . . .	53
6.2	Amorphous phase rigidity and dislocation activity . . . . .	61
6.2.1	Application of the Momentum Method on PE . . . . .	64
<b>7</b>	<b>Summary and Conclusions</b>	<b>71</b>
<b>8</b>	<b>Additional works</b>	<b>75</b>
8.1	Influence of molecular weight on $\gamma$ -phase formation . . . . .	75
8.2	Derivation of the Gibbs-Thomson equation . . . . .	83
	<b>References</b>	<b>86</b>
	<b>Appendix</b>	<b>101</b>
	Program codes . . . . .	101
	List of Abbreviations . . . . .	112
	List of Figures . . . . .	116
	List of Tables . . . . .	117
	<b>Curriculum Vitae and Publication List</b>	<b>119</b>
	<b>Acknowledgement</b>	<b>123</b>

# Chapter 1

## Introduction

Polymers have become indispensable in today's economy, industry and science. Especially thermoplastics such as polypropylene and polyethylene experienced a rapid growth in production within the last decades. Reasons for their success are not only because of their low production costs but also due to their simple processability, low weight, chemical resistance, permeability and low conductivity [1].

The microstructural mechanisms of plastic deformation of polymers are not fully clarified yet. However, a detailed understanding of mechanisms which are involved in plastic flow is essential not only to improve nowadays state of technology, e.g. increasing the strength of semicrystalline polymers, but may also become interesting for related disciplines. Although, the idea of dislocation based deformation mechanisms, is nothing new in polymer physics [2–13], it just gained increased attention within the last decade.

In semicrystalline polymers, the crystalline phase itself is a determining factor with respect to macroscopic strength. Previous investigations already focused on the verification of dislocation mechanisms within semicrystalline polymers [14–23]. An indispensable tool which allowed to quantify dislocations and as a consequence, investigate if dislocations play a role in plasticity is a special X-ray technique, called “Multiple X-ray line Profile Analysis” (MXPA) [24–29]. By this tool it could not only be proven that dislocations exist in polypropylene (PP), but do also multiply with increasing deformation [23]. A further verification of dislocations could be given by comparing size distributions obtained from MXPA and Differential Scanning Calorimetry (DSC), while the presence of crystalline defects has to be taken into account in order to achieve correct crystallite size distributions [21]. However, the concept of dislocations and their importance for plasticity can not be applied to all semicrystalline polymers. Some semicrystalline polymers, even the same type of polymer, but crystallized in a different crystal structure, do not show dislocation activity upon deformation [17, 18]. Additionally, the interplay of dislocations

and mechanical properties such as the yield stress was studied on the basis of strain rate jump tests in polyethylene (PE) [16], where a dislocation based model could be used to simulate the yield stress. It was demonstrated that the amount of dislocations being present in the material significantly influences the strength of semicrystalline polymers.

It can therefore be considered as very promising, especially from a technological point of view, if possibilities are found to interfere with dislocation processes in order to control mechanical properties to a certain extent. However, this can only be achieved if a serious understanding of microstructural deformation processes is available.

# Chapter 2

## Aim of the thesis

Investigations of deformation mechanisms which take into account dislocation based processes, concentrate on the crystalline phase. The present work extends this view by focussing on the role of the amorphous phase and its interplay with the crystalline domains with special respect to the dislocation concept, by performing specific temperature dependent in-situ experiments. Therefore, similar to previous studies, the MXPA-technique is used as an important tool in order to get information on the presence and the development of dislocations. If dislocations do play a role during plastic deformation, the mechanisms of dislocation interaction are to be clarified. In case dislocations do only play a minor role during plastic deformation, possible alternative deformation mechanisms are to be considered and discussed.

In the case of PE, it was not possible so far to obtain information about the development of dislocation densities during plastic deformation by conventional X-ray Line Profile Analysis (XLPA) methods due to its low number of independent high intensity reflections. Therefore, an alternative X-ray method had to be applied which allows to obtain information about microstructural parameters such as the dislocation density and the coherently scattering domain size from only a single X-ray line profile.

In order to achieve this goal several synchrotron campaigns using different in-situ setups have been planned. The results obtained from MXPA evaluations are assisted by mechanical and thermal characterizations in order to allow for an interpretation of micromechanical processes being involved in the yield and post-yield stage.



# Chapter 3

## Semicrystalline Polymers: State of the art

### 3.1 Structure and Morphology

Polymers are substances composed of macromolecular chains, which in turn consist of frequently repeating molecules, where the number of their repetitions increases up to several thousands. Depending on the arrangement of substituents on the chain, its tacticity is called isotactic, syndiotactic or atactic. However, in order to form a crystalline phase, which is characterized by a long range order, polymers need to be either isotactic or at least syndiotactic. In the semicrystalline state, the molecular chains form crystalline lamellae with a thickness of 5 to about 25 nm and up to several tenth of  $\mu\text{m}$  in lateral direction [30, 31] depending on the crystallization conditions and the type of polymer.

In most cases, the crystalline structure is characterized by a parallel arrangement of the macromolecular chains, where one chain can be folded several times, depending on the molecular weight of the material. This was concluded from the fact that the length of the macromolecules by far exceeds the thickness of the crystalline domains [32, 33]. Semicrystalline, melt crystallized samples are commonly characterized by a superstructure known as spherulites, build up by the crystalline lamellae which nucleate from a common center radially to the outside, with the crystals being embedded in an amorphous matrix (figures 3.1 and 3.2). The crystal growth is stopped on contact with neighbouring spherulites, which results in straight interfaces and a polygon like spherulitic shape in the fully crystallized sample.

The crystallographic structure of a semicrystalline polymer is usually not limited to a single phase. Polypropylene, for example, is polymorphic in its nature since it can crystallize in three different crystalline forms, which are the monoclinic  $\alpha$ , the hexagonal  $\beta$  and the orthorhombic  $\gamma$ -phase, at which the  $\alpha$ -phase is its most common crystal modification. Similar to many other polymers, the crystalline lamellae of the  $\alpha$ -phase of polypropylene show a parallel

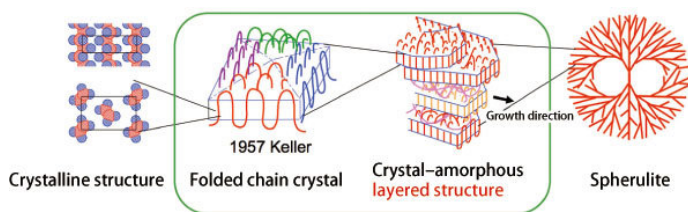


**Figure 3.1:** Morphological hierarchy of a semicrystalline polymer [34].

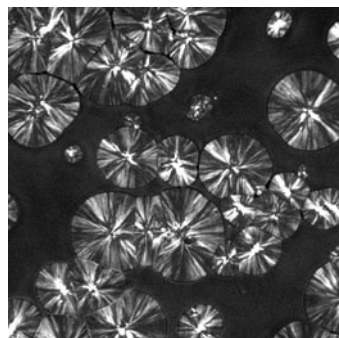


**Figure 3.2:** Optical micrograph showing spherulites [35].

chain arrangement. A unique characteristic of this phase is its lamellar branching or so called cross-hatched morphology. This crystallographic exception, which is obtained during almost all crystallization conditions, was first observed in the 1960s [36]. The lamellar branching is characterized by radial (“mother” lamellae) and nearly tangential (“daughter” lamellae) lamellar growth within the spherulites (figure 3.3). The origin of the crosshatching phenomenon could successfully be attributed to epitaxial interactions including (010) crystallographic planes [37, 38], where the daughter lamellae incline an angle of  $80^\circ$  to  $100^\circ$  with respect to the mother lamellae.

An efficient method in crystallizing PP containing significant amounts of  $\beta$ -modification or pure  $\beta$ -iPP is by adding  $\beta$ -nucleation agents [39–41]. Due to its lower surface free energy compared to  $\alpha$ -crystals and the presence of advantageously located secondary nucleation sites,  $\beta$ -lamellae posses an increased growth rate, however its primary nucleation rate is lower compared to the  $\alpha$ -phase. Hence, special  $\beta$ -nucleators are needed to obtain pure  $\beta$ -iPP [39, 41–43].

The orthorhombic  $\gamma$ -phase shows a quite unusual arrangement of the macromolecules within the unit cell. Instead of being arranged in a parallel manner as observed in most semicrystalline polymers, the chains form parallel bilayers, each bilayer tilted at an angle of approximately  $80^\circ$  to  $100^\circ$  against each other (figure 3.4) [44–46], very similar to the orientation of mother and daughter lamellae in branched  $\alpha$ -iPP, and about  $40^\circ$  with respect to the crystallographic  $b$  axis [47, 48].

A common method in crystallizing PP solely in its  $\gamma$ -modification is the application of high pressures during crystallization. While crystallizing iPP at pressures below 200 MPa both, the  $\alpha$  and  $\gamma$ -modification is observed, an increase in pressure above 200 MPa results in crystallization of  $\gamma$ -phase exclusively. Recently, it could be demonstrated that crystallization of the  $\gamma$ -phase can even be stimulated by adding  $\alpha$ -nucleation agents [49], caused by either direct nucleation of  $\gamma$ -crystals on the nucleating agents, or by enhanced nucleation of the  $\alpha$ -phase which serves as a “seed” since it is considered as an ideal substrate for epitaxial growth of  $\gamma$ -lamellae [38, 48–50].



**Figure 3.3:** Electron micrograph of a thin  $\alpha$ -iPP film, exhibiting lamellar branching at angles of  $80^\circ$  to  $100^\circ$  [38].

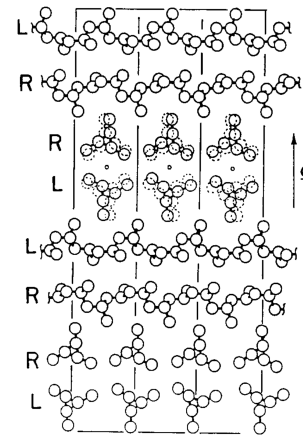


**Figure 3.4:** Unit cell packing of  $\gamma$ -iPP, in top view of the (110) plane [51].

## 3.2 Plasticity of Semicrystalline Polymers

Due to the complex structure and the presence of several phases with a large difference in their physical properties, but also due to changes in morphology with increasing strain, different deformation mechanisms, operating at the microscopic scale, are activated with proceeding deformation. Hence, in order to understand the deformation behaviour on the macroscopic scale, the phase specific micromechanisms of deformation have to be considered. This essentially comprises deformation of the amorphous and the crystalline phase.

The tensile test is a good example where different deformation mechanisms can be observed at different degrees of deformation (figure 3.5). This change in the deformation mechanisms was found to be activated at specific transition points for a large range of semicrystalline polymers, also being independent of chain architecture, drawing temperature and crystallinity [52, 53]. An important finding is that these transition points are triggered by the applied strain instead of stress [53]. Recently, Bartczak et al. [54] demonstrated that the deformation scheme can also be observed during plane-strain compression experiments, as demonstrated on the basis of a variety of polyethylene samples, also having different lamella sizes and crystallinities. The deformation scheme could be summarized as follows [52–54]:

(A) Transition from elastic to plastic deformation. Up to this point most of the strain is carried by the amorphous phase.

(B) The macroscopic yield point is reached and lamellar rotation occurs. Crystalline deformation changes from a localized slip of few lamellae with advantageous orientation with respect to the applied strain, to a more diversified distribution of crystallites.

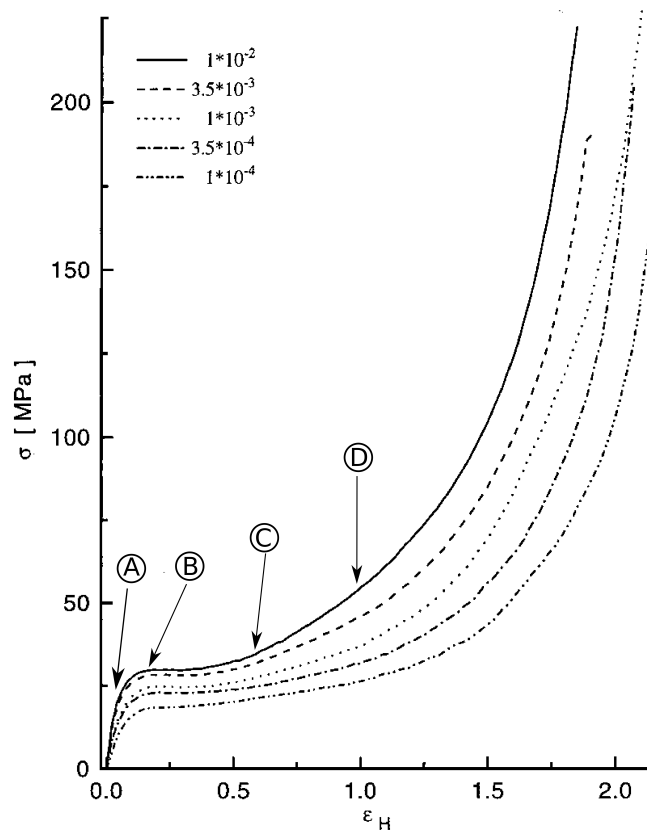


**Figure 3.5:** True stress-true strain relations for HDPE at different constant strain rates  $\dot{\epsilon}$ . Modified from [52]

(C) Molecules emerging from crystallites generating the amorphous network, such as tie-molecules, are highly strained. This leads to a transmission of stresses to the crystalline lamellae which encounter partial fragmentation.

(D) The amorphous fraction becomes fully stretched, resulting in pronounced strain hardening. The continuous fragmentation and the accompanied release of constraints enables the formation of a final fibrillar structure.

### 3.2.1 Deformation of the amorphous phase

While the crystalline phase is mainly formed by the repetitive folding of macromolecules, there is also a substantial amount of chains which do not fold back into the same lamella. Instead, these chains do also enter other crystalline lamellae, neighbouring spherulites, or the chain ends simply protrude from the crystal. All of these possible configurations together build up the amorphous phase in which the crystalline lamellae are embedded.

The amorphous phase plays an important role during the deformation since it adds additional degrees of freedom to the system. Three deformation modes have been postulated to take place during deformation in the amorphous phase, which is i) interlamellar shear, ii) interlamellar separation and iii) lamellae stack rotation [53, 55] which is shown schematically in figure 3.6.

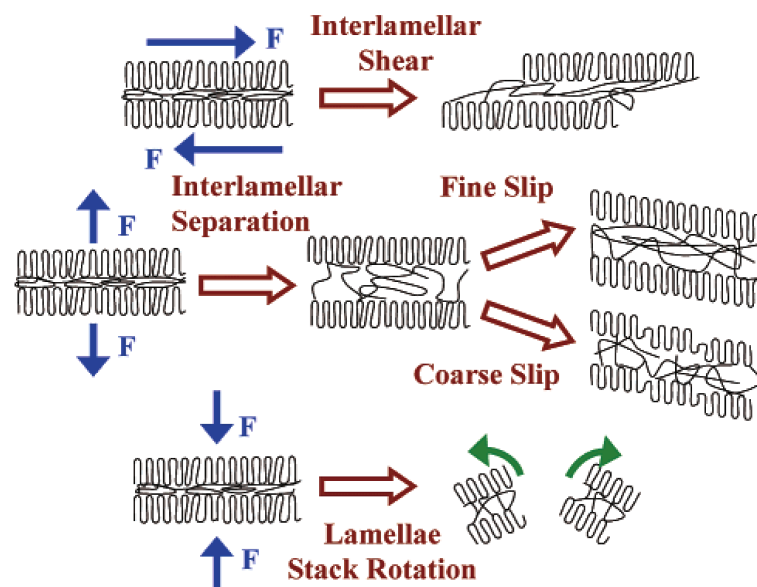


**Figure 3.6:** Plastic deformation mechanisms in semicrystalline polymers  $T_g < T_m$  [56]. The mechanisms of fine and coarse slip are discussed in section 3.2.2

*Interlamellar shear* or slip is characterized by a relative translation between lamellae crystals against each other, while the shear direction is aligned parallel to the lamellae. This deformation mechanism was found also to be recoverable [52]. The reason are tie-molecules connecting adjacent lamellae, but also a strong network of entangled chains, which retract the sheared crystals upon unloading.

When a tensile stress acts on two or more parallel lamellae, with its direction normal to the lamellae surfaces, these crystals experience *interlamellar separation*. This mode of deformation is distinguished by an increase in the distance of two parallel lamellae. Since a change in volume of the rubber like amorphous phase is difficult to perform, regions where interlamellar separation takes place are usually a source of cavitation which may in further consequence

lead to voids and crazes [53]. The resistance to this deformation mode strongly depends on the number of chains connecting the lamellae (taut-tie-chains), experiencing separation and the entanglement density within the amorphous phase. Alternatives to the formation of cavities have been discussed such as that surrounding material from the amorphous phase fills these gaps by simply “flowing” into them [57, 58]. However this alternative was also considered to be unlikely since it would require tie-molecules to break apart [32]. Instead it was suggested that the deformation can be accompanied by bending of the lamellae [32, 59].

In case of *lamellae stack rotation*, several layers of parallel lamellae rotate as a unit.

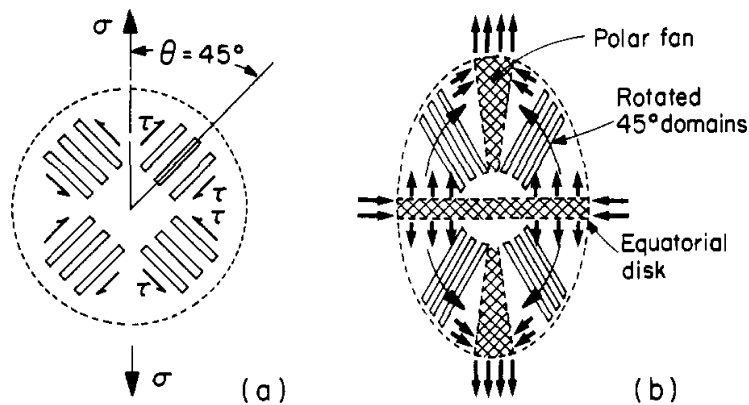


**Figure 3.7:** Possible deformation modes within a spherulite, depending on the location of the region with respect to the applied stress. (a) the  $45^\circ$  domains in an undeformed spherulite, (b) lattice rotations due to simple shear in  $45^\circ$  domains subject equatorial regions to enhanced tension and radial compression and polar regions to enhanced compression (modified from [55])

Considering uniaxial deformation these mechanisms appear simultaneously depending on the region within the spherulite with respect to the applied stress (figure 3.7). In general it can be observed that, in the case of e.g. tensile deformation, lamellar stack rotation occurs primarily in the equatorial regions of the spherulites, while the amorphous regions are tilted by  $45^\circ$  towards the applied stress and mainly experience interlamellar shear accompanied by a rotation of the crystalline lattice. In the polar regions however, the dominant mechanism is supposed to be interlamellar shear, while the lamellae are extended by a set of kinks which potentially form cavities with increasing deformation [55, 60].

### 3.2.2 Deformation of the crystalline phase

In contrast to the amorphous phase, the crystalline phase is characterized by a long range order on the molecular scale and a first order transition which is melting. It is well known that the yielding is strongly determined by the presence and deformation of the crystalline phase [54]. Even more interesting is the fact that especially the thickness of the crystalline lamellae is decisive for the yield point, in other words, the strength of the material [16, 61–63]. While at small strains, deformation mainly operates via the amorphous phase by shear within small microdomains, which multiply and finally end up in a macroscopic flow, this mechanism is quickly exhausted and deformation also involves the crystalline phase.

The exact mechanism of crystal plasticity was controversially discussed while three major models were formulated to describe the whole deformation path.

#### Peterlin's model of micronecking

Observations on plastically cold drawn polymers which experience necking depicted a transformation from the initial spherulitic, chain folded lamellar morphology to a strongly oriented fiber structure with a new long period. This experimental certainty was used by Peterlin to develop a model which should give an explanation of these considerable rearrangements on the molecular scale.

The model was divided into three deformation steps which contained, a) "*The continuous plastic deformation of the spherulitic structure before the neck*", b) "*The discontinuous transformation in the neck from the spherulitic to the fibre structure*" and c) "*Plastic deformation of the fibre structure after the neck*" [64]. The proposed deformation mechanisms in stage a) and c) do not differ severely from nowadays accepted explanations which involve in the case of a) inter and intracrystalline shear (slip) processes, lamellar stack rotation or phase transformations, and in the case of c) interlamellar shear and stretching of tie molecules leading to strain hardening. The proposed mechanism b), however, was exposed to justified criticism.

It was proposed that during stage b), the chain folded crystalline lamellae are transformed to a bundle of microfibrils, by so called "micronecking", which are the basic element of the final fiber structure. Hereby, small crystalline blocks should be "broken off" the lamellae at a microcrack (figure 3.8) [64] and rearrange with their chain axis parallel to the shear direction to a partially unfolded fibrillar chain structure with a regular amorphous spacing between the crystalline blocks (figure 3.9). However, Bartczak et al. [53] clearly pointed out that a basic requirement for this micronecking model is cavitation, otherwise a block rotation can not be performed due to the mechanical constraints by the neighbouring crystallites but also due to the



**Figure 3.8:** Microfibrils pulled out at the crack of polyoxymethylene (POM) single crystals [64]

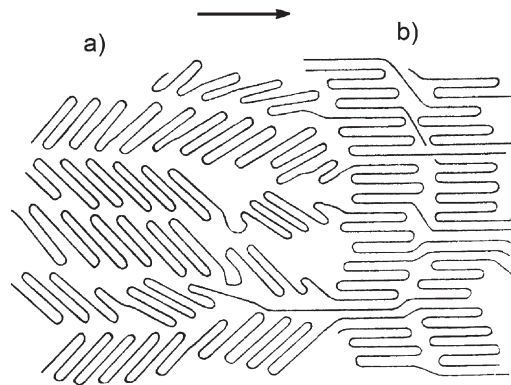


**Figure 3.9:** Peterlin's micronecking model [53]

amorphous phase (figure 3.9). Nevertheless, cavitation is only characteristic for tensile deformation modes (such as drawing), hence the micronecking model applies to deformation mechanisms in tension, but it fails if cavitation free deformation modes are considered, such as plain strain and uniaxial compression, where also a change from an initially isotropic, spherulitic structure to a microfibrillar fiber structure can be observed under the formation of a new long period [65]. The microstructural mechanisms operating during this deformation modes were clarified by taking into account crystallographic slip processes [65], which will be discussed in detail in section 3.2.2.

### The melting recrystallization model

A few years after Peterlin published his model, already considering the possibility of partial melting of the lamellae [64], Flory and Yoon [66] expanded the idea to the melting-recrystallization model taking into account data from neutron scattering. They concluded that as large irreversible deformations, as appear during cold drawing and plastic flow, must either include breakage of the macromolecular chains or destruction of pre-existing crystalline domains by melting [66]. Since plastic flow, in general is not accompanied by a decrease in molecular weight, mechanism one was excluded. Instead, they suggested that localized melting processes of small crystalline regions, followed by subsequent recrystallization to a new crystalline region in a pattern compliant with the prevailing stress. A problem of this model is that it does not sufficiently explain the yielding process. By taking into account crystallographic slip however, it

was possible to model the whole plastic strain range up to chain rupture. Additionally, it was experimentally confirmed that crystallographic processes are active at the yield. Séguéla [67] discussed these two processes pointing out that melting-recrystallization is not a necessity for plastic deformation but rather a consequence of chain unfolding, whereas crystallographic slip is present at all stages of deformation.

### Crystallographic slip

Basically, a crystalline lamella can be deformed by twinning, martensitic phase transformations and crystallographic slip, while the latter is the most important since it is present at all stages of deformation and can accommodate large plastic strains [68]. Crystallographic slip occurs, if two parts of a crystal separated by a common slip plane undergo a relative translation against each other which occurs, similar to metals, in the closest packed planes. Slippage within a crystal starts if the necessary critical resolved shear stress (CRSS) on such a slip plane is reached. However, it was found that the theoretically calculated shear stress being necessary to initiate slip is increased by an order of magnitude compared to the measured ones. The reason is that the crystal is not sheared at once, which would correspond to a simultaneous movement of all atoms within the slip plane against each other, instead the movement of atoms occurs consecutively. Within a crystal this mechanism corresponds to a movement of a dislocation, further discussed in section 3.2.3. If a force acts on a dislocation within a slip plane in direction of its Burgers vector, dislocation movement occurs. Hence, the resulting shear stress in this slip plane is essential for the dislocation mobility, if the critical resolved shear stress (CRSS)  $\tau_0$  is overcome. In case of uniaxial deformation with a stress  $\sigma$ , the resolved shear stress  $\tau$  can be calculated using Schmid's law:

$$\tau = \sigma \cos \kappa \cdot \cos \varphi = m\sigma \quad (3.1)$$

where  $\kappa$  and  $\varphi$  are the angles between the slip plane normal and the slip direction with respect to the uniaxial stress respectively (figure 3.10). The factor  $m = \cos \kappa \cdot \cos \varphi$  is the Schmid factor and can vary within  $0 \leq |m| \leq 0.5$ . This implies that at a given stress  $\sigma$ , the slip plane with the highest Schmid factor experiences the highest shear stress  $\tau$ . If this shear stress exceeds the critical resolved shear stress  $\tau_0$ , crystal slip will take place governed by dislocation motion.

In order to achieve homogeneous deformation of a crystal, at least five independent slip systems are required [69]. In polymers the number of possible slip systems is usually less than five due to its long chain structure. Instead, the soft amorphous phase acts as an additional slip system where the lamellae can rearrange. Two basic mechanisms of crystallographic slip are

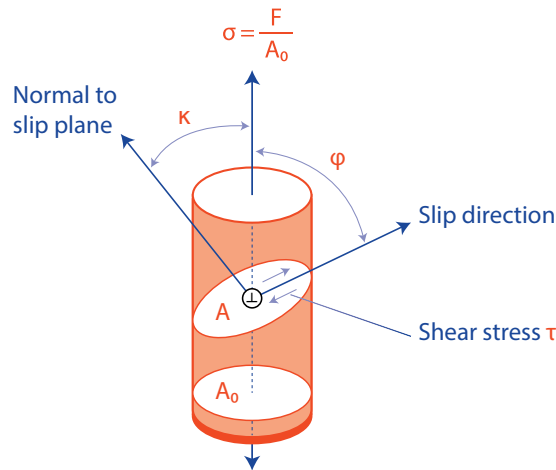


**Figure 3.10:** Crystallographic slip occurs if the shear stress exceeds a critical value on a slip plane. The shear stress depends on the orientation of the slip plane normal and the slip direction with respect to the applied stress.

observed, which is chain slip and transverse slip (figure 3.11). In case of chain slip, the slip direction is parallel to the chain direction. Chain slip already occurs at small plastic strains due to its low CRSS [60]. This was also supported by Shadrake and Guiu [9] who calculated line energies of various types of straight dislocations for polyethylene. A slip is called transverse, if the slip direction is perpendicular to the chain axis. Due to its higher CRSS, this type of slip commonly appears at higher deformations [22]. Crystallographic slip with the slip plane perpendicular to the chain axis would require chain rupture which is not possible due to the strong covalent bonds in the macromolecular chains (figure 3.11c).

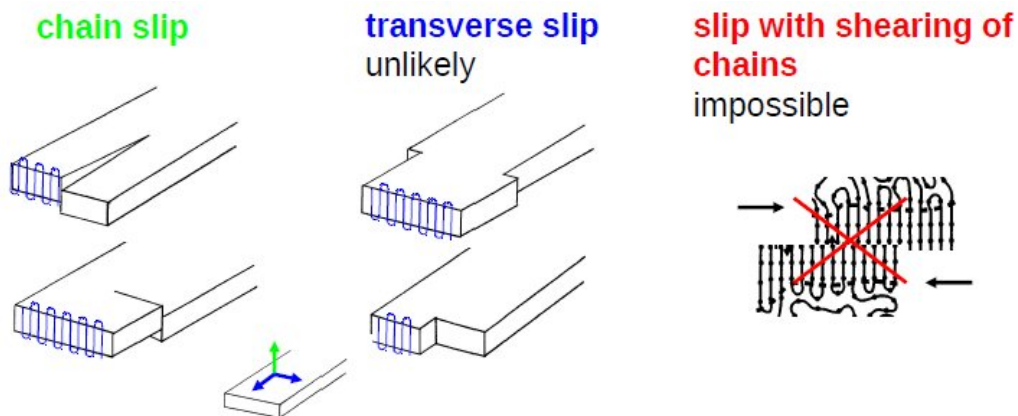


**Figure 3.11:** Chain slip is the preferred type of crystallographic slip, especially at small deformations due to its low CRSS. With increasing deformation, shear stress increases accordingly resulting in an additional activation of transverse slip. Due to strong covalent bonds in the chain, slip involving shearing of the chain is impossible.

On the basis of wide angle and small angle X-ray scattering (WAXS and SAXS) it is possible to determine the alignment of the molecular chain axis and the normal of the lamellar surface. This enables to differentiate between two modes of chain slip, which is fine slip and coarse slip. Considering fine slip, slip occurs on many parallel oriented planes simultaneously. This type of slip is characterized by an increase of the angle between the normal vector of the lamellae surfaces and the chain axis as deformation proceeds (figure 3.12b). In the case of coarse slip, less parallel slip planes are activated, though they experience much greater slip, while the angle between the normal vector of the lamellae and the chain axis does not change during deformation (figure 3.12c).

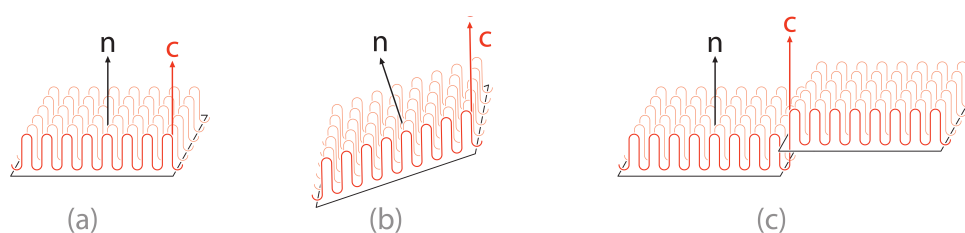


**Figure 3.12:** The lamella in its undeformed state (a) can deform by two types of chain slip, which is (b) fine slip, where an increase in the angle between normal vector of lamella surface and chain axis occurs, and coarse slip (c) where the angle between the two vectors remains uninfluenced.

As mentioned above, crystallographic slip is accompanied by dislocation generation and movement. The following chapter will elucidate the role of dislocations during deformation in more detail and discuss their basic principles.

### 3.2.3 Deformation by dislocation motion

The presence of dislocation was already postulated several decades ago in metal physics since the calculated stress required to deform a crystal plastically was much higher than the measured stress during the experiment. This discrepancy could be resolved by taking into account the presence of dislocations, facilitating the plastic flow. In polymers however, the presence of dislocations was controversial for a long time. Although, there existed already a large amount of literature which proved the existence of grown-in dislocations from solution grown single crystals [70, 71], the verifications of dislocations in melt grown semicrystalline polymers was rather challenging, amongst others, due to its multiphase morphology. Nevertheless, the presence of dislocations in melt-crystallized PP could be verified by Wilhelm et al. [23] using a special X-ray technique discussed in detail in section 3.2.3. It was possible to show that not only dislocations are present in the material, but also that their number multiplies with increasing deformation. This was a first direct experimental evidence that dislocations do play a role dur-

ing plastic deformation processes, at least in the  $\alpha$ -phase of PP. Continulative studies, also based on X-ray evaluations, concentrated on semicrystalline polymers with a non parallel chain alignment such as the  $\gamma$ -phase of PP, which develops at crystallization pressures above 200 MPa. In this case, similar to experiments of Wilhelm et al. the development of the dislocation density with increasing strain was investigated [17]. Surprisingly, instead of a permanent increase in the number of dislocations with proceeding deformation, its increase was much smaller. This certainty pointed at a different deformation mechanism being active in the material, instead of crystallographic slip guided by dislocation motion like in the case of  $\alpha$ -iPP, the primary deformation mechanism in the case of  $\gamma$ -iPP was interlamellar shear of the amorphous layers due to the non-parallel chain arrangement in the crystals leading to a higher CRSS [17, 48]. However, a small increase in dislocation density at higher degrees of deformation accompanied by a steady decrease in CSD-size could be observed. This process may be understood in terms of geometrically necessary misfit dislocations located between the boundaries of the crystalline blocks within the lamellae. Using a simple model [72], the dislocation density could be estimated on the basis of the crystalline block size [17]. The presence of dislocations could also be verified by more direct methods such as SEM and AFM [73]. In this case, high pressure crystallized PE was plastically deformed and investigated by SEM and AFM while dislocations could be observed at the side faces of the crystalline lamellae. Very recently, model predictions of the yield strength as function of strain rate for different amounts of dislocation density being present in the material were made, emphasizing the role of dislocations for plasticity [16]. In this work it could be shown that the yield strength, amongst the thickness of the crystalline lamellae, can be controlled by the number of dislocations present in the material. All these examples point at the importance of dislocations with respect to plasticity, which is also the reason why many plasticity models take into account a dislocation approach [3, 62, 63, 74]. Hence, the basic principles should be explained in the following sections.

### Theory of dislocations

Dislocations can be differentiated between two types that are, edge and screw dislocations, however in practice, dislocations were found to have qualities of both types, meaning that they are mixed. An edge dislocation can be constructed schematically by introducing an additional half plane of atoms in an undistorted, defect free crystal lattice, with the dislocation line being at the bottom of the extra half plane (figure 3.13). In order to construct a screw dislocation, one side of the crystal has to be shifted relative in one direction with respect to the opposite side (figure 3.14). The type of dislocation is usually determined by the angle or orientation of the Burgers vector with respect to the dislocation line. The Burgers vector determines the

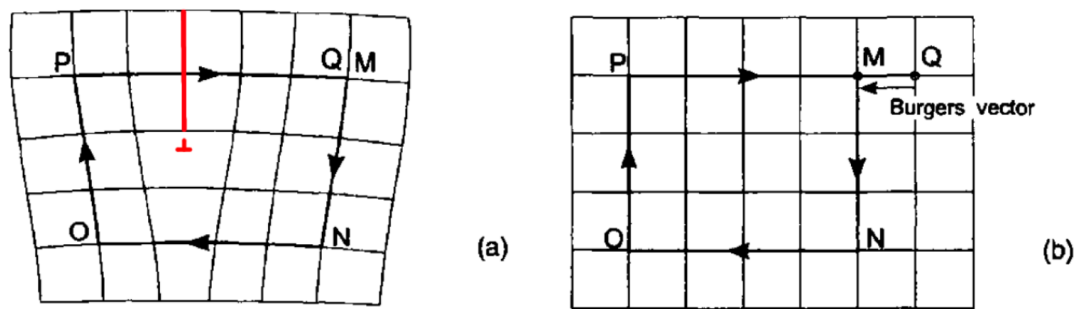


**Figure 3.13:** (a) An edge dislocation is constructed by adding an extra half plane of atoms in a crystal lattice (indicated by the red line). The Burgers circuit is shown by arrows around the edge dislocation with the positive line sense of the dislocation line into the paper. (b) Transferring the same circuit in the undistorted lattice yields the Burgers vector by the closure failure (modified from [75]).

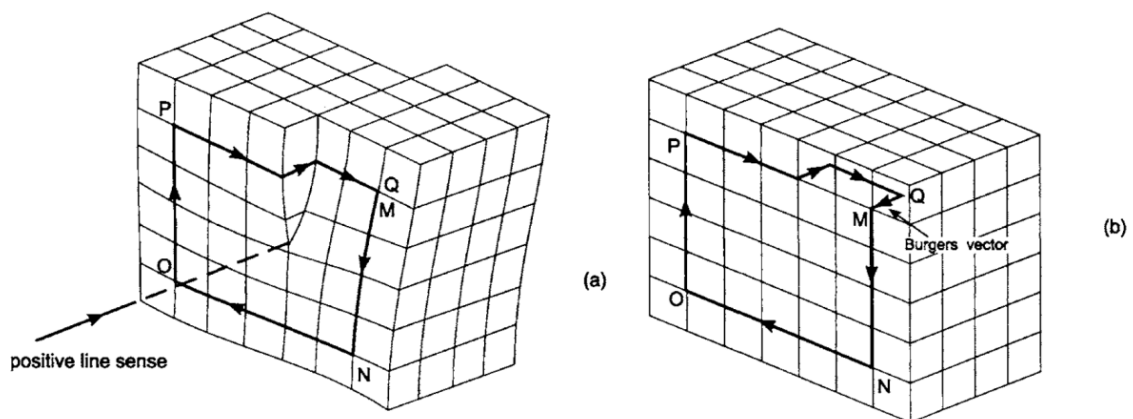


**Figure 3.14:** (a) A screw dislocation is obtained by shifting one side of a crystal with respect to its opposite side. The Burgers circuit is drawn around around the screw dislocation. (b) Transferring the same circuit in the undistorted lattice yields the Burgers vector by the closure failure [75].

magnitude and direction of the relative shift experienced by the two crystal parts. In case of an edge dislocation, Burgers vector and dislocation line are oriented perpendicular, for screw dislocations their orientation is parallel.

Many authors take into account a dislocation approach in modelling the flow stress of semicrystalline polymers. These models assume that the yielding is controlled by the energy being necessary to nucleate a screw dislocation with the Burgers vector being parallel to the chain axis within the crystalline lamellae, in other words, that shear stresses together with thermal fluctuations generate dislocations on the lamellae edges [9, 10, 12].

It has been shown that the required energy to generate a screw dislocation under a shear stress  $\tau$  is given by [9, 10]:

$$\Delta G = \frac{Kb^2l}{2\pi} \ln\left(\frac{r}{r_0}\right) - \taublr \quad (3.2)$$

which is composed of a term related to the stored elastic line energy per unit length for a pure screw dislocation and a term originating from the work supplied by external shear forces respectively, with  $K$  the crystalline shear modulus related to (hk0)[001] slip, the thickness of the crystalline lamellae  $l$ , the Burgers vector  $b$ , the core radius of the dislocation  $r_0$  (neglecting any contribution from the dislocation core) and the distance from the dislocation line to the lamella edge (radius of the dislocation)  $r$ . The critical dislocations radius, thus maximizing  $\Delta G$  is obtained by the first derivative of  $\Delta G$  with respect to  $r$  and setting it to zero resulting in

$$r_c = \frac{Kb}{2\pi\tau}. \quad (3.3)$$

The obtained critical Gibbs free energy will then read as:

$$\Delta G_c = \frac{Kb^2l}{2\pi} \ln\left(\frac{r_c}{r_0}\right) - \taublr_c = \frac{Kb^2l}{2\pi} \left[ \ln\left(\frac{Kb}{2\pi\tau r_0}\right) - 1 \right] \quad (3.4)$$

The shear stress at yield  $\tau_{yield} = \tau_y$  is thus obtained by rearranging equation 3.4

$$\tau_y = \frac{Kb}{2\pi r_0} \left[ \exp\left(\frac{2\pi\Delta G_c}{lKb^2} + 1\right) \right]^{-1} \quad (3.5)$$

In order to calculate the tensile yield stress  $\sigma_y$ , the validity of the Tresca yield criteria  $\tau_y = \sigma_y/2$  was assumed and applied to equation 3.5 resulting in

$$\sigma_y = \frac{Kb}{r_0\pi} \left[ \exp\left(\frac{2\pi\Delta G_c}{lKb^2} + 1\right) \right]^{-1}. \quad (3.6)$$

Considering that  $r_0 = 10 \pm 1 \text{ \AA}$  [9], which corresponds to twice the distance of neighbouring chains we can set  $r_0 \approx 2b$  [6] and

$$\sigma_y = \frac{K}{2\pi} \left[ \exp\left(\frac{2\pi\Delta G_c}{lKb^2} + 1\right) \right]^{-1}. \quad (3.7)$$

From equation 3.7 it can be seen that the yield stress is directly related to the thickness of the crystalline lamellae  $l$  (lamellae thickness) and on the test temperature by  $\Delta G$ .  $\Delta G$  has to be applied by thermal fluctuations and is proportional to  $kT$  with the Boltzmann constant  $k$  and the absolute temperature  $T$  [6]. This mechanism was initially proposed by Peterson [13] and developed further by Young [10] and also Shadrake and Guiu [9]. However, according to

this model, the yield strength increases monotonously with increasing lamella thickness which was disproved by Kazmierczak et al [61] by compression experiments on PE with lamellae thicknesses between  $l= 20$  nm and 170 nm (figure 3.15). Argon et al [62] were able to solve this discrepancy by assuming that edge and screw dislocation half loops nucleate on the surfaces of the lamellae being independent of the lamellae thickness. By this approach they could model the observed transition from a yield stress increasing with lamella thickness to one of constant development for high lamellae thicknesses (above ca. 20 nm). Another problem of the classical crystal plasticity approach (equation 3.2) is, that it is unable to fit both, the temperature and crystal thickness dependence of the yield stress. Brooks and Mukhtar [76] assumed that the core energy term (elastic strain energy of a screw dislocation within the core radius  $r_0$ )  $E_0$  cannot be ignored within the original formulation. By considering the core energy  $E_0$ , equation 3.2 becomes [76]:

$$\Delta G = \frac{Kb^2l}{2\pi} \ln \left( \frac{r}{r_0} \right) + E_0 - \tau blr. \quad (3.8)$$

Analogue to the steps performed above, the tensile yield strength results in:

$$\sigma_y = \frac{K}{\pi} \alpha(T) \exp - \left( \frac{2\pi \Delta G_c}{lKb^2} + 1 \right) \quad (3.9)$$

with the temperature dependent function

$$\alpha(T) = \frac{b}{r_0} \exp \left( \frac{2\pi E_0}{lK(T)b^2} \right). \quad (3.10)$$

By this approach they could model the yield stress in a temperature range from -60 to 60°. However, as Nikolov and Raabe pointed out [63], the approach suggested by Brooks and Mukhtar yields a negative core energy at elevated temperatures.

Nikolov and Raabe could solve this problem assuming nucleation and propagation of [001] screw dislocations as a result of 180° chain twist defects with a Burgers vector of  $c/2$ . This type of molecular twist mechanism had already been proposed by several authors [6, 8, 74, 77, 78] and will be discussed in section 3.3. The core energy of a twist defect is composed of, similar to above, the elastic energy from distortion within the misfit zone  $E_0$ , but also a term related to the energy change  $\delta U$  due to the twist motion.

Similar to the model to Brooks and Mukhtar the change in the free energy  $\Delta G$  originating from the nucleation of a pair of screw dislocations was calculated as [63]:

$$\Delta G = \frac{Kb^2l}{2\pi} \ln\left(\frac{r}{r_0}\right) + 2(E_0 + \delta U) - \taublr. \quad (3.11)$$

For the stress induced twist motion they suggested an Eyring activated rate process, also introducing a parameter  $\beta$  which takes into account surface and chain end effects. Their model for the yield stress could successfully describe the experimental data of Kazmierczak et al. [61] including the overshoot of the yield stress at a lamellae thickness of about 50 nm (figure 3.15). However, in case of temperature dependence, the model underestimates the yield stress for low temperatures below the glass transition temperature [61]. This is reasonable since the amorphous phase significantly contributes to the yield stress below the glass transition temperature and can therefore not be neglected.

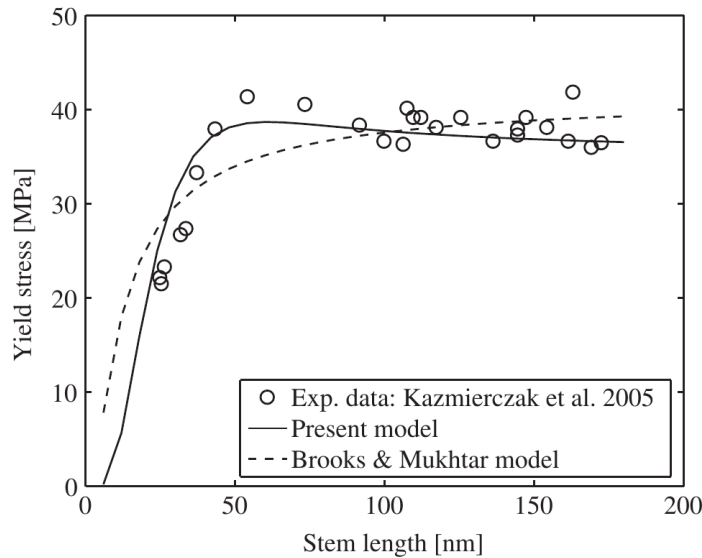


**Figure 3.15:** Yield stress as a function of lamellae thickness [63]

## 3.3 Molecular relaxations in polymers

### 3.3.1 Viscoelastic behaviour of polymers

Upon deformation, polymers show a viscoelastic behaviour, which can be described by an elastic and viscous component. During elastic deformation, the material changes its shape when subjected to an external force until it reaches a new equilibrium state. The energy which is applied during the deformation process is stored in the material and is available to restore the original shape of the material during unloading. Contrary, viscous behaviour, such as in viscous liquids change their shape irreversible upon an external load. Thus, due to their viscoelastic nature, polymers in general, but also an arbitrary given polymer type can exhibit both characteristics dependent of the considered time, frequency and temperature scale [79]. In contrast to purely elastic materials, viscoelastic materials do dissipate energy when an external force is applied and removed. This is reflected in a hysteresis loop when plotting the applied stress acting on the sample as a function of strain. The area of this loop is a measure of the energy lost during this cycling step [80]. Viscoelastic materials are characterized by a strong strain rate dependence. Depending whether the stress changes linearly or nonlinearly under the applied strain rate, it is differentiated between linear and non-linear viscoelasticity respectively. Principally, linear viscoelasticity occurs if a material is subjected to deformation that is either very small or very slow. This allows the application for various mathematical models based on the assumption that the total deformation is the sum of elastic (Hookean) and viscous (Newtonian) components in order to predict the response of the material under different loading conditions [81]. In order to study viscoelastic behaviour and in further consequence molecular relaxations and transition points, data are required for a wide range of frequency and/or temperature. A common method, beside stress-relaxation and creep experiments, is the application of dynamic mechanical analysis .

#### Dynamic Mechanical Analysis (DMA)

In this experimental procedure, the sample is subjected to an alternating, usually sinusoidal, strain while simultaneously measuring the stress. In a purely elastic scenario, stress  $\sigma$  and strain  $\varepsilon$  will be in phase, while in a purely viscous case, strain lags behind stress by  $\pi/2$ . Hence, in the viscoelastic case, the behaviour will be somewhere between these two extremes.

This behaviour is expressed by

$$\varepsilon = \varepsilon_0 \sin \omega t \quad (3.12)$$

and

$$\sigma = \sigma_0 \sin(\omega t + \delta) \quad (3.13)$$

with the angular frequency  $\omega$  and the phase lag  $\delta$ .

Applying the addition theorem for trigonometrical functions on equation 3.13 yields [81]:

$$\sigma = \sigma_0 \cos \delta \sin \omega t + \sigma_0 \sin \delta \cos \omega t. \quad (3.14)$$

If we rewrite equation 3.14 in a more simple form by substituting  $A = \sigma_0 \cos \delta$  and  $B = \sigma_0 \sin \delta$  we see that the stress is composed of two components: with the first term being in phase with strain and the second term being  $90^\circ$  out of phase with the strain:

$$\sigma = \underbrace{A \sin \omega t}_{\text{in phase with } \varepsilon} + \underbrace{B \cos \omega t}_{\pi/2 \text{ out of phase with } \varepsilon}. \quad (3.15)$$

We can expand equation 3.14 by  $\varepsilon_0$  to

$$\sigma = \varepsilon_0 \frac{\sigma_0}{\varepsilon_0} \cos \delta \sin \omega t + \varepsilon_0 \frac{\sigma_0}{\varepsilon_0} \sin \delta \cos \omega t = \quad (3.16)$$

$$= \varepsilon_0 E' \sin \omega t + \varepsilon_0 E'' \cos \omega t \quad (3.17)$$

with

$$E' = \frac{\sigma_0}{\varepsilon_0} \cos \delta \quad E'' = \frac{\sigma_0}{\varepsilon_0} \sin \delta \quad (3.18)$$

where  $E'$  is called the *storage modulus*, since it is a measure of the elastic energy stored within the material and is in phase with the strain, while  $E''$ , which is out of phase with the strain is known as *loss modulus* and can be related to a dissipation of energy during deformation by internal friction, molecular motion and relaxation processes [80].

Together with

$$\varepsilon = \varepsilon_0 \exp\{i\omega t\} \qquad \sigma = \sigma_0 \exp\{i(\omega t + \delta)\} \qquad (3.19)$$

the complex modulus  $E^*$  can be calculated:

$$E^* = \frac{\sigma}{\varepsilon} = \frac{\sigma}{\varepsilon} e^{i\delta} = \frac{\sigma}{\varepsilon} (\cos \delta + i \sin \delta) = E' + iE'' \qquad (3.20)$$

Figure 3.16 shows the phase diagram for the complex modulus including the phase angle  $\delta$ .

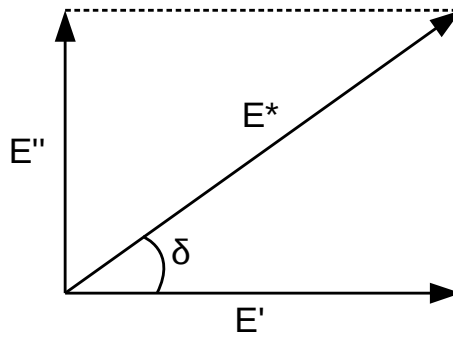


**Figure 3.16:** Complex modulus  $E^*$

The tangent of the phase angle is also called damping or loss factor and is a measure of how efficiently the material loses energy due to molecular relaxations and friction. According to figure 3.16 it is seen that it is the ratio of the loss and the storage modulus and is independent of sample geometry [79]:

$$\tan \delta = \frac{E''}{E'} = \frac{G''}{G'} = \frac{\eta''}{\eta'} \qquad (3.21)$$

where, similar to the complex modulus  $E^*$ ,  $G''$  and  $G'$  are the components of the complex shear modulus  $G^*$  and  $\eta''$   $\eta'$  of the complex viscosity  $\eta^*$  [79, 81].

### 3.3.2 Molecular relaxations and transitions

A big advantage of DMA is its high sensitivity in contrast to other methods such as differential scanning calorimetry (DSC) or differential thermal analysis (DTA), where transition temperatures, e.g. the glass transition temperature  $T_g$ , are often undetectable. Moreover, in combination with a temperature scan at constant frequency or alternatively, a frequency scan at constant temperature, molecular relaxations and transitions can be studied.

Molecular relaxations are usually labelled  $\alpha$ ,  $\beta$ ,  $\gamma$  etc. in order of their appearance with decreasing temperature. Thus, in amorphous polymers, the transition at the highest temperature is commonly the  $\alpha$ -transition also known as glass transition. The glass transition is characterized by large scale chain motion (in the order of up to 100 carbon atoms [82]) being accompanied by a drastic change in the elastic modulus. Relaxation orders at lower temperatures originate from a steady decreasing number of mobile chain segments.

In case of semicrystalline polymers however, an additional transition can be observed above  $T_g$ . This  $\alpha$ -transition was frequently attributed to originate from both, the amorphous and the crystalline phase [83, 84] which can further be subdivided into an  $\alpha_1$  and  $\alpha_2$  transition [83, 85]. Measurements on cold drawn and annealed high density polyethylene (HDPE) sheets showed [86] that a maximum loss in the  $\tan \delta$  curve occurs at the  $\alpha$ -transition when the lamellae incline an angle of about  $40^\circ$  with respect to the applied stress. This leads to a maximum resolved shear stress parallel to the crystals which undergo an interlamellar shear. Consequently, this transition was associated to interlamellar shearing processes. The authors Stachurski and Ward [86] and Ward and Sweeney [81] concluded that the molecular origin of this process was attributed to shear in the crystallographic  $c$  direction ( $c$ -shear) together with chain motion on the lamellae surface. However, in case of low density polyethylene (LDPE),  $c$ -shear and interlamellar shear are two different types of relaxations, which were attributed to the  $\alpha$  and  $\beta$ -relaxation respectively due to their large difference in activation energy [87]. More recently, Hoyos et al. [84] investigated the correlation between the  $\alpha$ -relaxation and the crystalline morphology in iPP, pointing out that a key mechanism determining the intensity of this transition is, irrespective of the exact molecular mechanism involved, the exchange of isotactic sequences between the crystalline and amorphous phase.

A possible molecular mechanism which could explain this exchange of chain segments was proposed first by Renecker et al. [88] and then refined by Mansfield and Boyd [89]. This mechanism involves a twisted region accomplished by rotation of a macromolecular chain by  $180^\circ$  that propagates along the chain axis through the crystal [89] (figure 3.17). After this point defect passed through the crystal, a translation of the whole chain stem occurs by a distance of  $b=c/2$ , which not only results in a rearrangement of the crystal surface but also in a modification

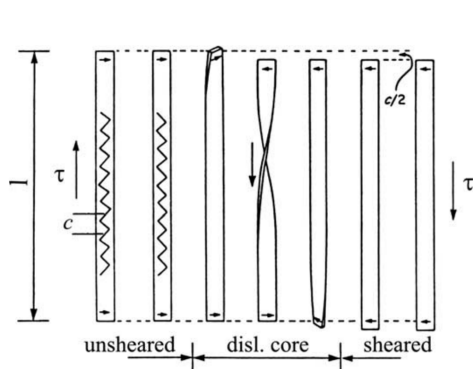


**Figure 3.17:** Under the application of a shear stress  $\tau$ , crystal slip occurs with a Burgers vector  $b=c/2$  occurs due to propagation of a  $180^\circ$  chain twist defect [63, 77].

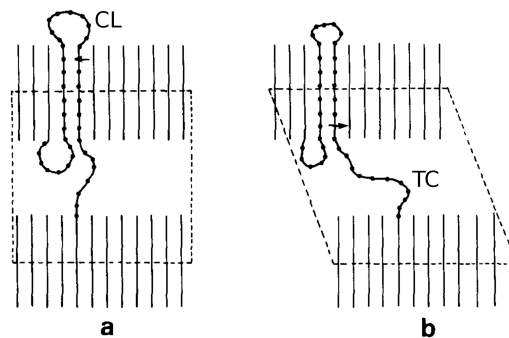


**Figure 3.18:** Reorganization of the crystal interface occurs by (a) shortening of chain loops (CL), which permits (b) lengthening of tie chains (TC) permitting additional deformation of the amorphous phase (modified from [77])

of the tie chains, connecting the crystalline with the amorphous phase. Figure 3.18 demonstrates this process by means of chain loop shortening. The propagating twist defect leads to translational mobility within the crystal, resulting in a surface modification by shortening of two loops. This in return allows for an extension of tie chains which allows for further softening of the interlamellar material [77].

Some semicrystalline polymers such as polyethylene terephthalate (PET) and isotactic polystyrene (iPS) do not possess an  $\alpha$ -relaxation. It is supposed that this is due to their bulky side groups which strongly increase the necessary energy for the formation of such a defect [77].

Similar to amorphous polymers, the  $\beta$  (glass-rubber) relaxation  $T_g$  or  $T_\beta$  in semicrystalline polymers is attributed to large molecular rearrangements within the amorphous phase solely. In case of PP Jawad and Alhaj-Mohammad [90] studied the  $\beta$ -relaxation in samples subjected to different draw ratios. They reported a decrease in the loss factor ( $\tan \delta$ ) upon drawing and attributed this phenomena to the hindered mobility of the amorphous regions, thus relating it to the glass transition temperature. These findings are also supported by the relatively high difference in activation energies between the  $\alpha$  and the  $\beta$ -relaxation. The glass transition represents a major transition for many polymers being accompanied with drastic changes in the physical properties of the material e.g.: a strong decrease in the Young's modulus upon heating. The  $\gamma$ -relaxation is characterized by only short ranged rotations and motions. Such mechanisms were attributed to sub-glass transitions in general, also called crankshaft motions, since it involves rotations of only a few bonds. The simplest rotations, in terms of minimal energy requirement, that leave the chain stems in place are the three bond [91] and the five bond motion [92] (figure 3.19).

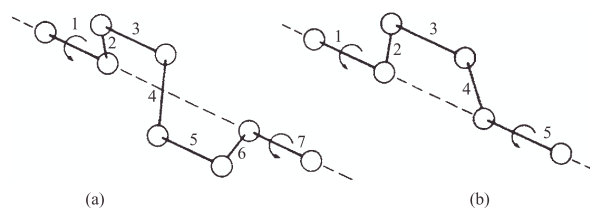


**Figure 3.19:** Three and five bond crankshaft motion

Dielectric relaxation measurements on PP also show a weak  $\delta$ -transition located at a temperature of approximately  $-240^{\circ}\text{C}$  to  $-173^{\circ}\text{C}$ . As expected, the reported activation energies for this processes were rather small being in the range of 1 kJ/mol to 5 kJ/mol [85, 93], while its molecular mechanism was attributed to hindered rotations of  $\text{CH}_3$  groups [93, 94].

# Chapter 4

## Experimental Details and Methodology

### 4.1 Sample preparation

The main focus of this work was dedicated to polypropylene, especially its  $\alpha$ -modification, since it is not only a model material for the application of X-ray line profile analysis methods, but it is also known to show strong dislocation activity upon plastic deformation [16–19, 21–23]. As additional materials polyethylene terephthalate (PET) and polyethylene (PE) were chosen due to their relatively high crystallinity. The experiments presented in chapter 5 include (i) in-situ annealing experiments and (ii) in-situ deformation experiments, both during simultaneous X-ray diffraction.

(i): For the in-situ annealing studies, compression molded boards were also cut and afterwards cold rolled to different strains in order to introduce a large number of dislocations (see section 5). The in-situ annealing itself was performed using a heating stage located within a vacuum chamber (figure 4.4) which allowed to span the relevant temperature range from  $-180^{\circ}\text{C}$  up to  $400^{\circ}\text{C}$ .

In case of (ii), uniaxial compression was chosen as deformation mode, which allows to reach high strains, simultaneously minimizing crazing. A specially designed miniature compression machine was used for this purpose which can directly be mounted next to the particle detectors at the beamline (figure 4.3). The samples used for the in-situ compression studies were first cut from compression molded plates to rectangular blocks using a “*Struers - Accutom*” precision cut-off machine with water cooling and were then turned to cylinders with approximately 8 mm in diameter. Since all compression experiments were performed in transmission, a low sample diameter was essential to minimize absorption.



**Figure 4.1:** Compression chamber used for the production of  $\gamma$ -samples

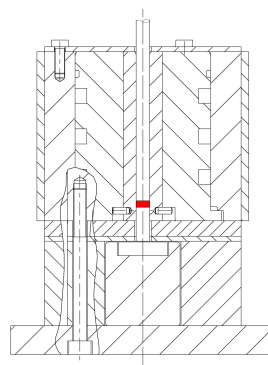


**Figure 4.2:** Construction drawing of the compression chamber. The position of the sample is highlighted in red.

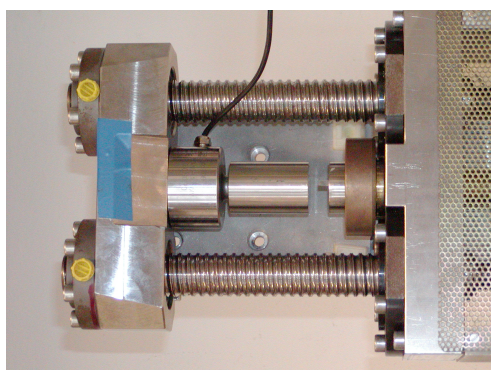


**Figure 4.3:** Miniature compression machine used in an in-situ setup

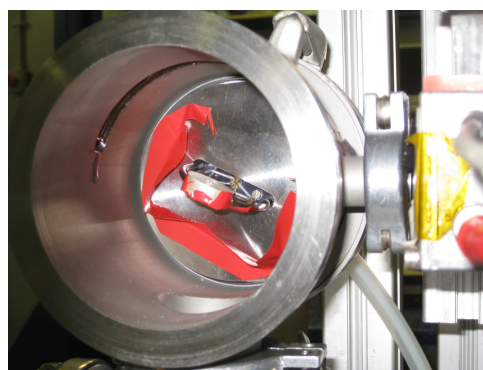


**Figure 4.4:** Heating stage mounted to the vacuum chamber

Additionally it was investigated in how far the molecular weight of iPP has an impact on its  $\gamma$ -phase crystallization (chapter 8.1). Therefore, a specially designed compression chamber was used for the production of  $\gamma$ -samples, which was mounted to an ultimate tensile testing machine of the type “shimadzu” (figure 4.1 and 4.2). The device allowed for production of samples with 8 mm in diameter and a maximum height of about 4 cm. The necessary pressure for crystallization was controlled by software within an accuracy of 0.02 MPa. Heating was achieved by a ceramic heating band mounted on the upper part of the compression chamber allowing for a maximum heating rate of 12 °C/min. The temperature was controlled by an “Eurotherm 3216N” PID temperature controller, equipped with a sensor support for a Type J thermocouple. An implemented RS232 serial interface allowed for a computer connection and to predefine a temperature program via software. Cooling from the melt to the crystallization temperature was achieved by aircooling using ventilators with an average cooling rate of approximately 4.5 °C/min and watercooling was used for cooling down to room temperature. A more detailed explanation of the experimental procedures is given in the corresponding chapters 5 and 8.1.

## 4.2 Differential scanning calorimetry (DSC)

Differential scanning calorimetry, together with differential thermoanalysis (DTA) are the dominant analytical methods for studying thermal behaviour of materials. In general, calorimetry determines the quantity of heat which is generated, or has to be generated for a physical or chemical transition to occur, which goes along with a change in the inner energy of the substance, also referred to as enthalpy in case of constant pressure [95].

A key parameter in characterization of transitions is the change in enthalpy at a transition between two states. Such transitions can lead either to an increase in enthalpy such as occurs during melting or at the glass transition, or to a decrease during crystallization or decomposition [95, 96].

Basically DSCs can be differentiated between two different operational methods, that are heat-flux and power compensation. In case of heat flux DSC the samples and a reference which does not show any transition temperatures, are located in the same heating chamber, subjected to the same temperature program. If a phase transition, e.g. melting occurs in the sample, where its temperature stays constant until the transition is finished, the resulting temperature difference leads to a change in heat flow which is proportional to the heat capacity.

However, during power compensation, sample and reference are located in different heating chambers. If the sample experiences a transition, the resulting temperature difference to the reference has to be balanced to zero by either heating or cooling. Here, the difference in heating power between sample and reference corresponds to the heat flow. Power compensated DSCs are considered to be more accurate since reaction processes can be resolved better, due to the small heating chambers and the fast response of the electrical components.

A power compensated DSC of the type “Perkin Elmer 8500” was used for DSC studies. Beside determination of first and second order transitions such as the melting and glass-transition, DSC is ideally suited for determining crystallinity or the thickness of crystalline domains, the lamellae thickness. The overall crystallinity of a polymer is obtained by the ratio of the melting enthalpy and the melting enthalpy of the theoretically 100% crystalline material. However, it has to be taken care of, that a potential recrystallization peak originating from e.g.: too fast cooling during the measurement, has to be subtracted.

In contrast to single crystalline low molecular weight substances, which exhibit a clearly defined melting temperature, semicrystalline polymers, are characterized by a broad melting interval. While the shape of the melting peak depends on the size distribution and morphology of the crystals, the position of the melting peak is determined by the finite thickness of the crystalline lamellae. In contrast to an infinitely large ideal single crystal with a equilibrium melting tem-

perature  $T_m^0$ , the melting temperature of a “real” semicrystalline polymer is located at a lower temperature. This behaviour is expressed by the Gibbs-Thomson equation [97] (section 8.2):

$$T_m = T_m^0 \left( 1 - \frac{2\sigma_e}{\Delta h_f \cdot \lambda} \right) \quad (4.1)$$

with the surface energy  $\sigma_e$ , the enthalpy of fusion for the crystalline phase  $\Delta h_f$  and the lamellar thickness  $\lambda$ .

### 4.3 X-ray Line Profile Analysis

The analysis of X-ray diffraction profiles and patterns in terms of their broadening and shape is generally known as X-ray Line Profile Analysis (XLPA or XPA). These methods allow for a determination of microstructural parameters such as the presence and density of dislocations and the thickness of crystalline lamellae by considering the broadening of X-ray line profiles. This broadening can be attributed to the limited crystal size on the one hand and to strains within the crystal lattice, which cause a deviation from the perfect atomic order on the other hand. The most advanced version of XLPA allows for a reliable separation of strain and size related peak broadening by taking into account multiple X-ray profiles and their upper harmonics and is thus called Multireflection X-ray line Profile Analysis (MXPA) [27].

#### 4.3.1 MXPA and CMWP-fit

The measured intensity distribution of a Bragg reflection can be described by a convolution of the size and strain related intensity distributions known as the Warren and Averbach equation [98, 99]:

$$A(L) = A^S(L)A^D(L) = A^S(L) \exp(-2\pi^2 g^2 L^2 \langle \varepsilon_L^2 \rangle) \quad (4.2)$$

with the variable of the Fourier transform  $L$  the size coefficients  $A^S(L)$  and distortion coefficient  $A^D(L)$  which depends on the length of the diffraction vector  $g$  and the mean square strain  $\langle \varepsilon_L^2 \rangle$ . Krivoglaz [100] and Wilkens [101, 102] were able to derive the mean square strain under the assumption that it is caused by the strain field of dislocations:

$$\langle \varepsilon_L^2 \rangle = \left( \frac{b}{2\pi} \right)^2 \pi \rho C f \left( \frac{L}{R_e^*} \right) \quad (4.3)$$

with the Burgers vector  $b$ , the dislocation density  $\rho$ , the contrast factor of dislocations  $C$  and the Wilkens function  $f(L/R_e^*)$ . The Wilkens function depends on the Fourier length  $L$  and

the outer cut off radius of dislocations  $R_e^*$  which determines the range of the distortion fields of the dislocations. The size coefficient is calculated under the assumption of a lognormal size distribution of the crystals [103]. The contrast factor of dislocations  $C$  considers the anisotropy of lattice distortions generated by dislocations or more generally, the influence of dislocations on the peak broadening, and depends on the relative orientation of the Burgers vector, line vector and diffraction vector. Thus, the dislocation related peak broadening also depends on the orientation of the diffraction vector and will therefore be varying for different reflections, the peak broadening is anisotropic. While in single crystals, the contrast factor  $C$  can be determined experimentally, an average contrast factor  $\bar{C}$  is used in case of polycrystals, by averaging over the possible slip systems [104]. The most advanced version of MXPA fits ab-initio physical functions directly to the measured data, called ‘‘Convolution Multiple Whole Profile - fitting’’ or ‘‘CMWP-fit’’. The corresponding software package available at <http://csendes.elte.hu/cmwp/>, developed by Ribarik et al. [103] has been used as a major tool for the evaluation of diffraction profiles throughout this work. The theoretical profile is basically composed of a polynomial function  $BG(2\theta)$  which describes the diffuse scattering, e.g. due to the amorphous phase, or air scattering, and a profile  $I^{hkl}$  which models the individual peaks

$$I_{theoretical} = BG(2\theta) + \sum_{hkl} I_{MAX}^{hkl} I^{hkl}(2\theta - 2\theta_0^{hkl}) \quad (4.4)$$

where  $I_{MAX}^{hkl}$  is the intensity of the corresponding Bragg-reflection located at  $2\theta_0^{hkl}$ . Instrumental peak broadening and the functions describing the peak broadening due to dislocations, size effects and planar faults is included within the mathematical formulation of  $I^{hkl}$ .

### 4.3.2 Modified Williamson-Hall analysis

The Williamson-Hall (WH) analysis [105] and especially its modified version (MWH) [27] are fast methods for an estimation of the dislocation density and the crystallite size, where, instead of the whole peak profile, only the peak broadening or the integral breadth is used as input parameter for the evaluation procedure. The general equation for the Williamson-Hall plot, using the full width at half maximum (FWHM) for the peak broadening is given by

$$\Delta K = 0.9/D + \Delta K^D \quad (4.5)$$

where  $D$  is a measure for the average size of the crystalline domains, the coherently scattering domain size (CSD-size) and  $\Delta K^D$  is the strain contribution to the line broadening [27] with  $K = 2 \sin \theta / \lambda$ , where  $\theta$  and  $\lambda$  are the diffraction angle and wavelength respectively. However, the peak width will not always show a monotonic behaviour as a function of the diffraction or-

der  $K$ , which is known as strain anisotropy. Strain anisotropy originates from lattice distortions caused by the presence of dislocations. Ungár et al. demonstrated that this anisotropy can be accounted for by introducing the contrast factor of dislocations  $C$ . Plotting the peak width as a function of  $K\bar{C}^{1/2}$  instead of  $K$  results in the modified Williamson-Hall plot [104], where the peak widths form a monotonous function in  $K\bar{C}^{1/2}$  if the strain induced peak broadening originates from the presence of dislocations:

$$\Delta K = 0.9/D + (\pi M^2 b^2 / 2)^{1/2} \rho^{1/2} K \bar{C}^{1/2} + O(K^2 \bar{C}) \quad (4.6)$$

where  $\bar{C}$  is the average of the contrast factor,  $M$  is a constant depending on the outer cut-off radius of dislocations, the Burgers vector  $b$  and the average dislocations density  $\rho$ .

### 4.3.3 Momentum-Method

In contrast to the multi-reflection-techniques mentioned above, the momentum method allows to extract the same physical quantities out of a single line profile. The method developed by Groma [106–108] is based on the asymptotic behaviour of the second and fourth order restricted moments and can be considered as an advancement of the variance method originally proposed by Wilson [109]. The  $k$ th order restricted moments  $M_k$  are defined as

$$M_k(q') = \int_{-q'}^{q'} q^k I(q) dq / \int_{-\infty}^{\infty} I(q) dq \quad (4.7)$$

where  $I(q)$  is the intensity of the measured profile as a function of  $q = 2/\lambda(\sin\Theta - \sin\Theta_0)$ , with the wavelength  $\lambda$ , the diffraction angle  $\Theta$  and the Bragg angle  $\Theta_0$  [108]. Wilson [109] and Groma [106] calculated the the second order restricted moment, for the case of large  $q$  values as

$$M_2(q) = \frac{q}{\pi^2 \varepsilon_F} - \frac{L}{4\pi^2 K^2 \varepsilon_F^2} + \frac{\Lambda \langle \rho \rangle \ln(q/q_0)}{2\pi^2} \quad (4.8)$$

with  $\varepsilon_F$  as the area weighted particle size [110], the Scherrer constant  $K$ , the taper parameter  $L$  describing the rate of decrease of the cross section area of crystallites [108, 110], the average dislocation density  $\langle \rho \rangle$ , the dislocation contrast factor  $\Lambda$  and the fit parameter  $q_0$  [108]. The fourth order restricted moment reads as:

$$\frac{M_4(q)}{q^2} = \frac{q}{3\pi^2 \varepsilon_F} + \frac{\Lambda \langle \rho \rangle}{4\pi^2} + \frac{3\Lambda^2 \langle \rho^2 \rangle}{4\pi^2 q^2} \ln^2(q/q_1) \quad (4.9)$$

where  $\langle \rho^2 \rangle$  is the square of the average dislocation density and  $q_1$  is again a fitting parameter.

## 4.4 Synchrotron Experiments

A large extent of this work is based on in-situ deformation and temperature controlled experiments during simultaneous X-ray diffraction, while the recorded diffraction patterns were evaluated using the techniques explained in chapter 4.3. Due to their multi-phase nature, semicrystalline polymers exhibit a viscoelastic behaviour. This is reflected in stress relaxation tests for example, where stress decreases monotonously when constant deformation or strain is applied on the sample. Especially during in-situ diffraction experiments, this is an undesired effect, since stress relaxation is also coupled to microstructural changes, particularly in terms of dislocation kinetics. Therefore, measurement times during such experiments must be kept at a minimum which requires high intensity light sources, however, this requirement is usually not fulfilled by conventional laboratory X-ray sources. Another problem with many conventional diffractometers is the initial peak broadening due to instrumental conditions (instrumental broadening). Since copper is commonly used as anode material, not only the desired  $K_\alpha$ , but also  $K_\beta$  radiation together with a continuous Bremsstrahlungs-spectrum are emitted. In case of a copper anode, the two latter are often filtered by a nickel filter with its absorption edge between the  $K_\alpha$  and  $K_\beta$  lines, thus eliminating the  $K_\beta$  radiation. A better solution is the use of monochromator single crystals with a well known lattice spacing. Under the utilization of the Bragg condition, a better monochromatic radiation in terms of  $\frac{\Delta\lambda}{\lambda}$  is obtained compared to a nickel filter for example.

In order to meet the requirements of high intensity, combined with monochromatic radiation, synchrotron light sources are an ideal experimental tool. The diffraction experiments within this work were primarily performed at the synchrotron light laboratory “*ELETTRA*” in Trieste, Italy, SAXS-Beamline (5.2L). This beamline offers the possibility to measure at three different discrete energies of 5.4, 8 and 16 keV adjustable by a double-crystal monochromator containing three pairs of asymmetrically cut flat Si(111) crystals, each optimized for the mentioned energies [111]. An adjustable slit system allows to modify the spotsize on the sample down to dimensions of about  $30 \mu\text{m}^2$  with a flux density at the sample of  $1 \cdot 10^{12} \text{ ph s}^{-1} \text{ mm}^{-2}$  at a beam current of 400 mA and 8 keV. The photon flux, thus allows to study samples with several mm in diameter at relatively short measurement times. This is an important feature, since most diffraction experiments were performed in a transmission setup. The reason is that a larger sample volume is investigated, which minimizes artefacts originating from local inhomogeneities. The application of XLPA methods, especially MXPA, requires the detection of as many diffraction orders as possible, hence an appropriate detector system is required. In the following experimental sections, two types of detectors were used. First, an *INEL CPS-590* position sen-

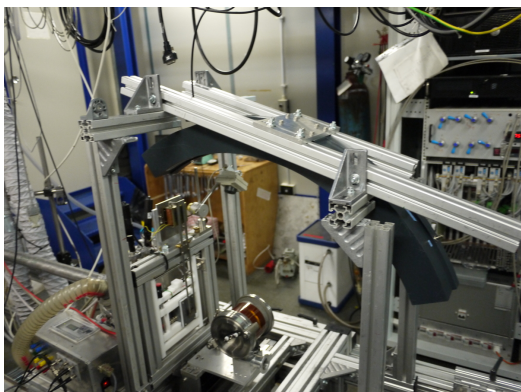


**Figure 4.5:** Inel detector used in the synchrotron setup



**Figure 4.6:** Two dimensional Pilatus detector

sitive linear detector curved by an angle of  $90^\circ$ . This curvature is part of a circle with a diameter of 500 mm, with the sample located in the center (figure 4.5).

A *PILATUS* hybrid pixel detector was used as an alternative detector (figure 4.6). In contrast to metals, polymers not only show broader diffraction peaks, but also a significant increase in diffuse scattering due to the amorphous phase. This generally results in a higher value of integral counts (photons striking the detector per time interval). Since this detector type has a very low readout time due to its solid-state sensors, compared to gas based detectors, measurements can be performed at higher integral count rates, thus again decreasing the measurement time. However, the two dimensional detector area was limited to  $83.8 \times 33.5 \text{ mm}^2$ , thus the available angular range was smaller compared to the *INEL* detector.

In order to minimize diffuse scattering, which is already considerably larger in polymers compared to metals due to the presence of an amorphous phase, the primary X-ray beam, was encapsulated by lead (Pb) panels along the distance, sample - slit system. During some experimental setups, special equipment such as a miniature uniaxial-deformation machine (figure 4.3), heating chamber (figure 4.4) or cryostream cooler were used. Those devices, very often contain components which are made of iron or titanium and thus can contaminate the diffraction pattern by secondary scattering. This certainty had to be taken care of by covering critical parts of the devices by lead to keep pollution of the recorded diffraction patterns at a minimum.

## 4.5 Data Pre-processing

### Calibration

Data recorded by particle detectors contain two parameters, the number of particles striking the detector (number of events) and the positions or locations where these events occurred (channel number). Hence, before any evaluation step can be performed it is necessary to determine the  $2\Theta$  angle of the corresponding channel number. Therefore, a material with well separated Bragg-reflections, where its exact positions are well known has to be measured. A common material for calibration is  $\text{LaB}_6$ , however, the same quality could be obtained by the use of standard thermoplasts like polypropylene or polyethylene terephthalate (PET). In case of two dimensional data acquisition using the PILATUS detector, determination of the beam center and detector tilt was performed in addition using the software “fit2D” [112–114]. Especially taking into account the tilt of the detector around the horizontal beam axis is important since this allows to correct for possible distortions of the diffraction patterns [114] which may lead to inaccurate values obtained by XLPA.

In case of the INEL detector, the conversion from the channel numbers to  $2\Theta$  diffraction angles was undertaken by a computer program written in the programming language *OCTAVE* [115, 116]. In this case, distortions of the diffraction profiles are already at a minimum since the detector covers the sample in a curved  $90^\circ$  angular range where the sample is located in its center.

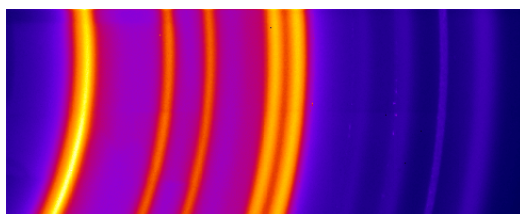


**Figure 4.7:** Recorded 2D “raw” data of  $\alpha$ -iPP on the *PILATUS* detector. The Bragg-reflections are represented by Debye-Sherrer rings.

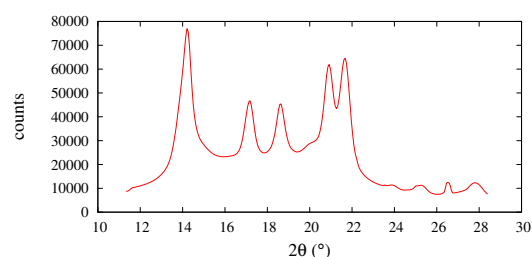


**Figure 4.8:** After calibration and integration of the raw data, a final diffraction pattern for  $\alpha$ -iPP is obtained with the number of counts as function of the diffraction angle  $2\Theta$ .

### Phase separation

As already mentioned in chapter 3, semicrystalline polymers often have a multiphase crystalline structure. Commonly only a single phase shall be investigated, therefore each phase of the diffraction patterns has to be modelled separately while only the phase of interest is used for further evaluations. Since many different patterns are generally recorded during an in-situ experiment, an evaluation script has been written in the Bash Unix shell and command language, in order to speed up the phase separation process (section 8.2). This script uses the command-line program “*Gnuplot*“ [117] for two dimensional plots and the program “*fityk*” [118], both freely available.

The program is optimized for handling of polypropylene, since this was the main material of interest in this work. At the beginning, the supporting points for the background function can be set individually in each diffraction pattern which are then transferred to “*fityk*” where the background is subsequently fitted by a polynomial fifth order. It has to be mentioned that this background model is just provisional to ensure a reliable fit of the Bragg reflections. The final diffuse background scattering is taken care of in the evaluation using CMWP-fit. After all phases have been modelled, the phase of interest is obtained by subtracting the remaining phase from the diffraction pattern and exported to a separate file.

It turned out to be very valuable to perform a modified Williamson and Hall analysis (section 4.3) on the phase separated diffraction pattern. A corresponding software package is available [115] which not only allows to check the influence of a different background fit on the result, and give a first rough estimation about crystallite size and dislocation density, but also provides a first determination of the fit parameters for the average dislocation contrast factor  $\bar{C}$ . This fit parameters are then used as starting parameters and are refined in the following whole profile fitting approach (CMWP).

During the CMWP evaluation a more accurate determination of microstructural parameters of the material, such as the dislocation density, median of grain size distribution, outer cut-off radius of dislocations and grain ellipticity is obtained. It was taken care that the outer cut-off radius of dislocations is fixed well below the thickness of the crystalline lamellae. As final evaluation step the “multi-eval” extension to CMWP-fit was used [119]. Hereby, different starting values for the microstructural parameters are set, while each possible permutation of those parameters is used for an evaluation of CMWP-fit. The program analyses all results with respect to their residuals, by which the global minimum is obtained, followed by calculating the average and standard error for each parameter [119].

# Chapter 5

## Results

### 5.1 Molecular relaxations occurring during annealing

#### 5.1.1 Polypropylene

In order to study the thermal stability of deformation induced dislocations, in-situ heating experiments were performed using synchrotron radiation. Therefore polypropylene of the type “BE50” (MFI 0.3 g/10 min at 230 °C, 2.16 kg) containing  $\alpha$ -nucleating agents was severely pre-deformed to a plastic true strain of  $\varepsilon = 1.2$  by cold rolling in steps of  $\varepsilon \cong 0.15$  in order to introduce a high number of dislocations. After the rolling process, the sample was immediately stored in a bath of liquid nitrogen ( $T=77$  K). This prohibited any relaxation of the material followed by a potential reduction in defect concentration.

Before the sample, still at liquid nitrogen temperature, could be mounted to the sample stage, it had to be ensured that first, the stage is also cooled to  $T=77$  K and second, the fixing of the sample to the stage occurs at the same low temperature. This was achieved by cutting a block of expanded polystyrene (EPS) to rectangular dimensions, so that the part of the stage on which the sample will be mounted is fully immersed in liquid nitrogen. A temporary sealing of the EPS block and the metal cylinder was achieved by an adhesive tape (figure 5.1 and 5.2). After liquid nitrogen was put in the EPS block, the sample was quickly transferred from the storage container to the bath and mounted above the pinhole of the sample stage. The transfer time of the sample was kept below one second, thus it can be assumed that warming of the sample and consequential relaxations were negligible.

The sample stage was then mounted to the heating chamber and connected to the temperature controller (figure 5.3). After starting the vacuum pump, the EPS block was removed and the heating chamber was closed immediately. This procedure guaranteed that the sample was at

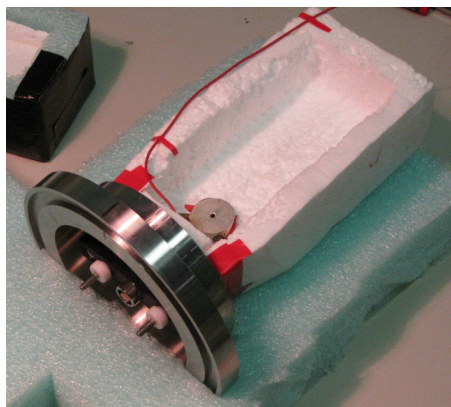


**Figure 5.1:** The sample stage was embedded in a block of polystyrene which served as pool for liquid nitrogen. A temporary tightening was achieved by a simple adhesive tape. This had the advantage that the EPS block could quickly be removed from the stage prior the measurement.

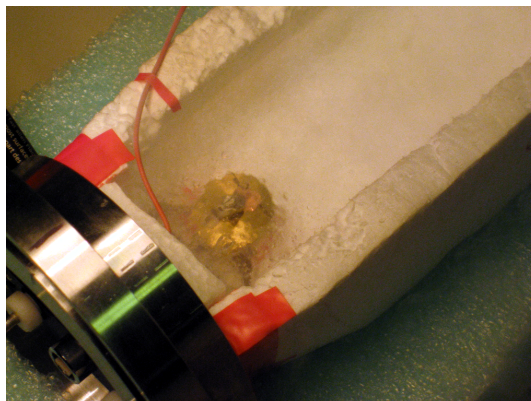


**Figure 5.2:** In order to avoid warming of the sample, it was mounted to the stage in a bath of liquid nitrogen.

low temperatures during the whole transfer process and undesired formation of ice which could lead to additional peaks in the diffraction pattern was avoided by measuring in vacuum. Figure 5.4 shows the transmission measurement setup with the sample stage mounted to the heating chamber. The red line represents the incoming beam which is diffracted by the sample and exits through the pinhole to the detector.

Wide Angle X-ray Diffraction (WAXD) patterns were then recorded at different annealing temperatures starting from  $-180\text{ }^{\circ}\text{C}$  up to  $165\text{ }^{\circ}\text{C}$ . When a target temperature was reached, it was waited for 10 min for the sample to obtain thermal equilibrium. Afterwards each annealing temperature was kept constant for 600 s, simultaneously performing X-ray diffraction, before heating to the next temperature. After a diffraction pattern was recorded above the melting temperature of  $165\text{ }^{\circ}\text{C}$ , the sample was cooled to room temperature of  $T=22\text{ }^{\circ}\text{C}$  and an additional pattern was recorded for the recrystallized sample.

Figure 5.5 and 5.6a show the diffraction patterns recorded at different annealing temperatures up to the melt. The sample relaxation is clearly visible by the shift of the reflection peaks to smaller  $2\Theta$  angles, especially for the (040) and (130) reflection (figure 5.6b). It can already be seen in figure 5.5 that the amount of  $\gamma$ -phase in the material is marginal (about 5%), however, since only the monoclinic  $\alpha$ -phase shows dislocation mediated deformation mechanisms [17, 19, 23] and is therefore of interest, the  $\gamma$ -fraction was modelled and removed from the diffraction pattern.

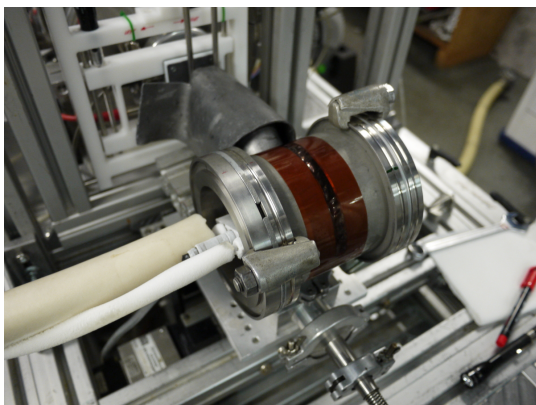


**Figure 5.3:** The sample stage, still attached to the EPS block, mounted to the heating chamber. Before the EPS block can be removed, the stage has to be connected to the temperature controller ensuring a LN2 flow to the sample. If this is accomplished, the LN2 bath can be removed, followed by immediately closing the heating chamber in order to build up vacuum.

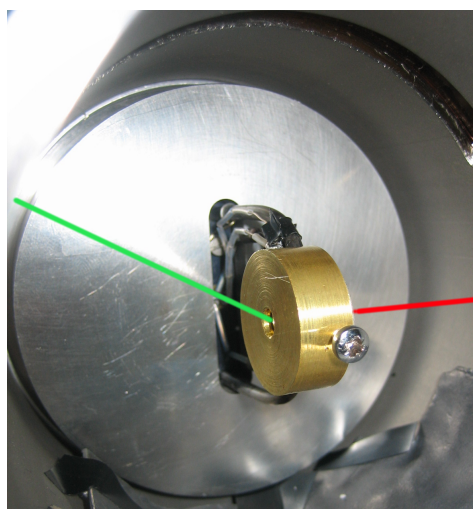


**Figure 5.4:** The transmission setup with the sample holder mounted to the heating chamber. The red line represents the incoming beam, while the green line indicates an arbitrary reflection from the sample

The obtained diffraction patterns were then evaluated by the MXPA method, providing the development of the dislocation density and CSD-size as a function of annealing temperature (figure 5.7 and 5.8). It is noted at this point that the error bars in figure 5.7 and 5.8 represent a numerical error originating from the evaluation process. A small error bar indicates low residuals of the resulting convergent fit obtained from a rough scan of the starting value parameter space [119]. Three distinct drops in the dislocation density development can be found in figure 5.7. During the first drop, a decrease from  $\rho = 1 \times 10^{16} \text{ m}^{-2}$  to about  $\rho = 8.5 \times 10^{15} \text{ m}^{-2}$  reaching a temperature of  $-100 \text{ }^\circ\text{C}$  is observed. The dislocation density then stays constant up to the glass transition temperature of PP ( $T_g \approx 10 \text{ }^\circ\text{C}$ ), followed by a significant decrease by about  $2.5 \times 10^{15} \text{ m}^{-2}$  where a small plateau is reached. Exceeding a temperature of  $100 \text{ }^\circ\text{C}$  is again accompanied by a pronounced change in the dislocation density which leads to its reduction to a value as low as  $\rho = 0.9 \times 10^{15} \text{ m}^{-2}$ . After the sample was heated above its melting temperature, it was cooled to room temperature where, in its recrystallized state, a dislocation density of  $\rho = 0.4 \times 10^{15} \text{ m}^{-2}$  was obtained.

The coherently scattering domain size changes insignificantly over a wide temperature range (figure 5.8). A slight change within 12 and 14 nm can be observed from  $-180 \text{ }^\circ\text{C}$  to about  $100 \text{ }^\circ\text{C}$ , followed by an increase to about 16 nm. After the sample was recrystallized from the melt, a CSD-size of 14 nm was obtained.

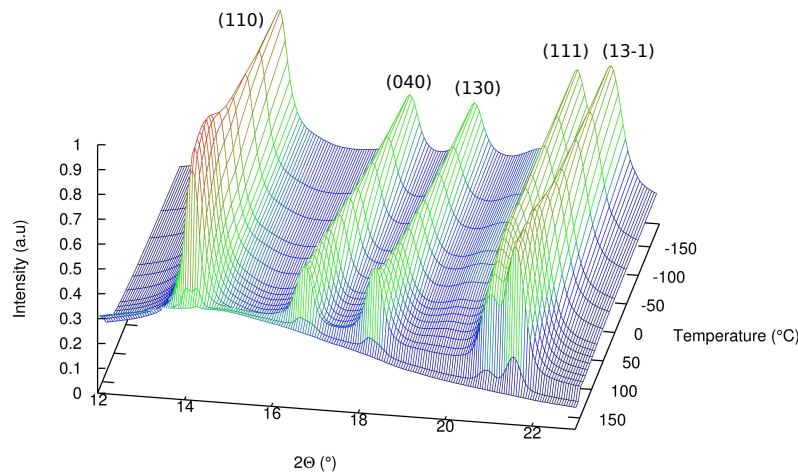


**Figure 5.5:** Diffraction patterns were recorded for various annealing temperatures, up to the melting temperature.

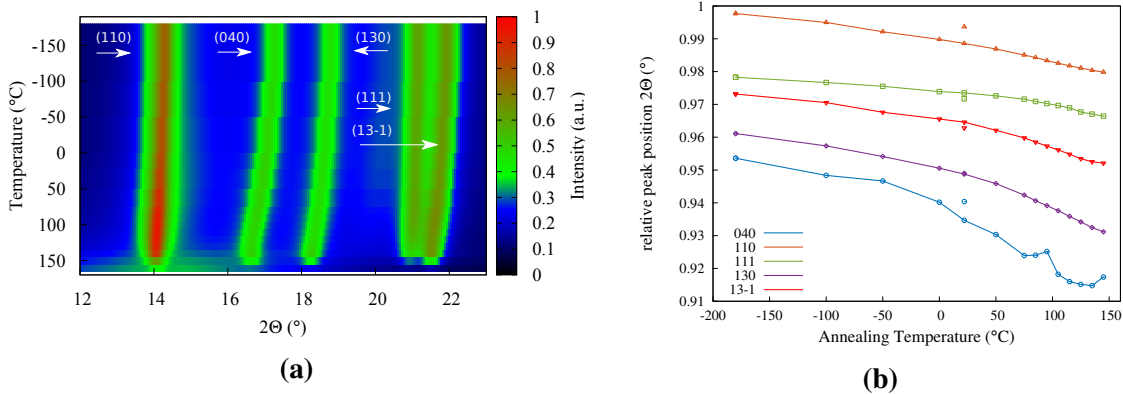


**Figure 5.6:** (a) and (b): A peak shift to lower  $2\theta$  angles is observed, which is caused by sample relaxation. The positions of the recrystallized samples are plotted as separate points

### Dynamic Mechanical Thermal Analysis (DMTA)

Additional DMTA measurements were performed which allow to correlate changes in the dislocation density to molecular relaxations. Methods for determining the complex modulus  $E^*$  comprised the usage of an “ANTON PAAR MCR301” and a “Perkin Elmer Pyris” device operated in torsion and compression mode. Measurements were carried out on undeformed and deformed samples (figure 5.9a). In case of the latter, a compression molded PP plate was cold rolled to a true strain of  $\varepsilon = 1.2$  and was then carefully cut using a “Struers-Accutom” precision saw with water cooling and low rotations. Measurements were carried out at frequencies of 0.5, 1 and 10 Hz within a temperature range from  $-140\text{ }^\circ\text{C}$  to  $155\text{ }^\circ\text{C}$  using a heating rate of  $2\text{ }^\circ\text{C}/\text{min}$  (figure 5.9b). Additionally, measurements of the loss modulus and the storage modulus were performed (figure 5.10), as a function of temperature measured at three different frequencies. However, the molecular relaxations occurring during annealing are seen best in the loss tangent

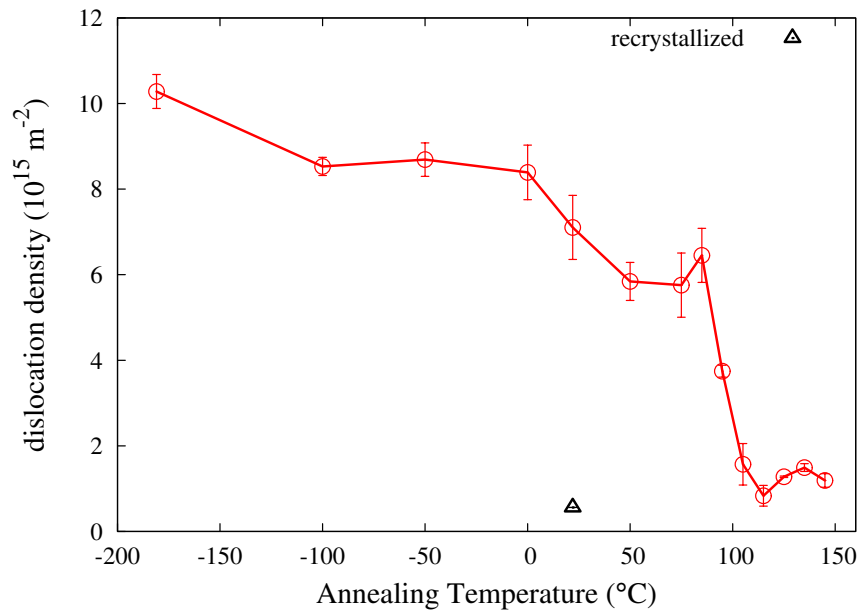


**Figure 5.7:** The development of the dislocation density as a function of annealing temperature. A significant drop in the defect concentration can be observed exceeding a temperature of  $T=10$  °C and beyond 85 °C.

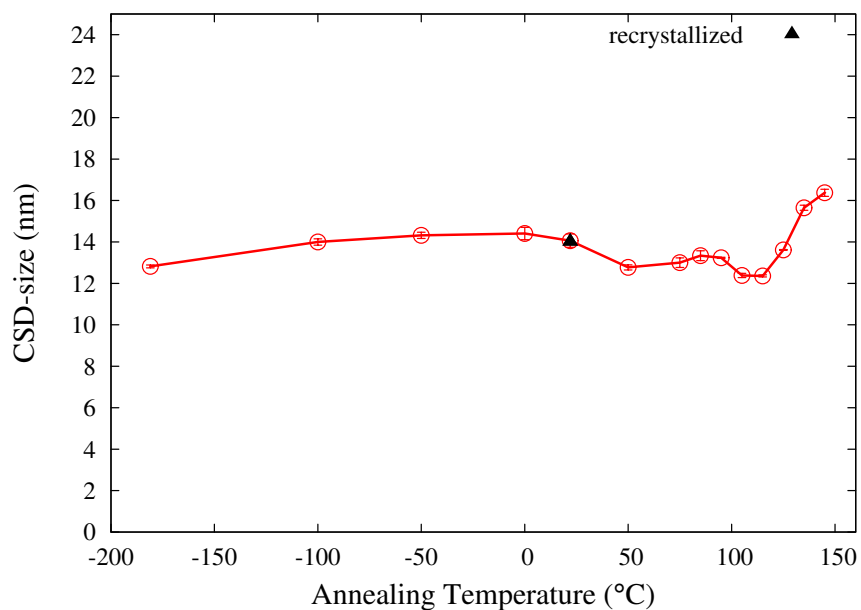


**Figure 5.8:** The domain size only changed slightly up to about 100 °C which can be considered to be within the experimental error. The error bars are in point size, which indicates well converging fits for the different starting parameters.

delta curves, not mentioned that this quantity is not dependent on sample geometry like the two other ones. To ensure that measurements are carried out within the viscoelastic regime a small dynamic strain of 0.05% amplitude was applied.

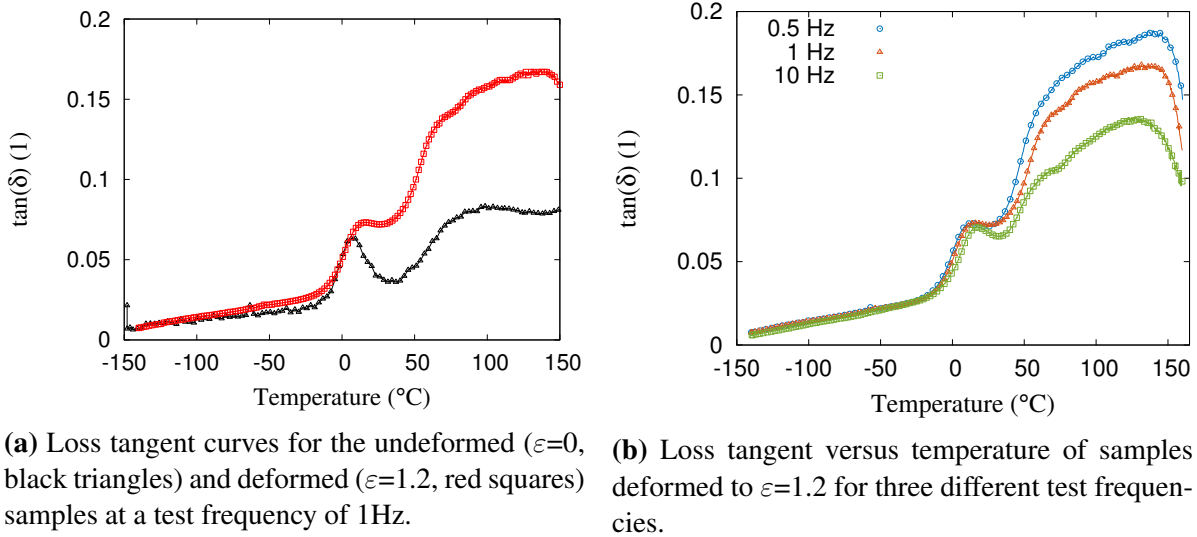


Figure 5.9

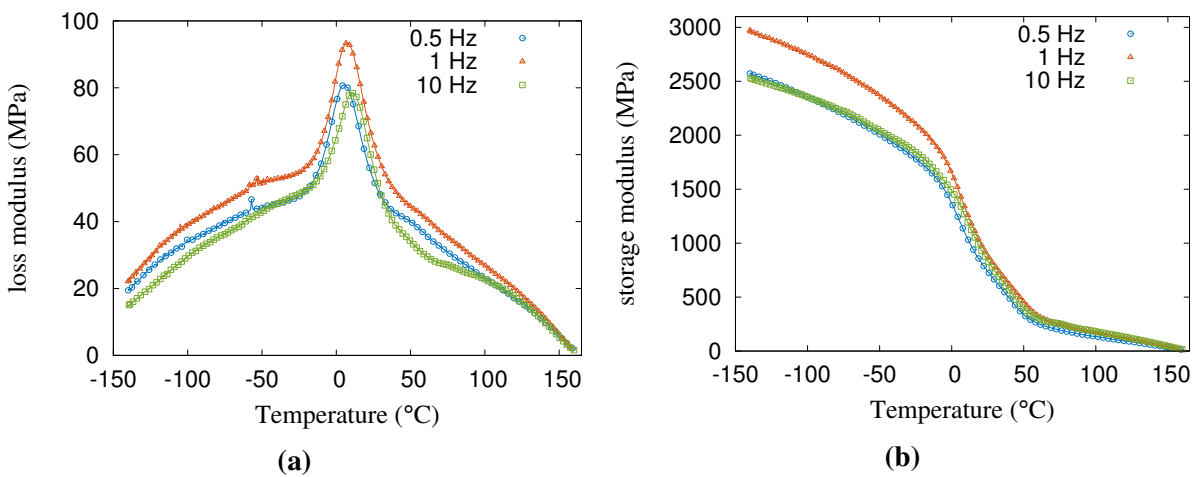


Figure 5.10: (a) Loss and (b) storage modulus measured at test frequencies of 0.5, 1 and 10 Hz.

### 5.1.2 Polyethylene terephthalate (PET)

In-situ annealing studies were also performed on PET. However, the relatively complex molecular structure of the material and the lower symmetry of the triclinic unit cell [120] impeded the evaluation of diffraction patterns. Since PET is, amongst carbon and hydrogen, also composed of oxygen, the absorption during X-ray diffraction is drastically increased compared to PP. Therefore it was necessary to keep the sample thickness low in order to reduce absorption. Furthermore, the evaluation of the dislocation density was performed by an improved version of the modified WH-analysis [22], since triclinic structures can not be accounted for by the CMWP-package.

**Table 5.1**

	lamellae thickness (nm)	crystallinity (%)	glass transition (°C)
PET extruded	18.3	8.5	73.1
PET annealed	21.7	37.1	66

As raw material, extruded bands were provided by the "Laboratory of Polymer Engineering LKT-TGM, Austria". The DSC traces in figure 5.11 show that crystallinity was very low after the extrusion process. A value of 8.5% was obtained after subtracting the recrystallization peak, which is not high enough in order to perform profile analysis. Therefore the sample was crystallized for 5 hours at a temperature of 185 °C, which increased the crystallinity to 37.1%. A side effect of the annealing process was that the lamellae size distribution was narrowed, meaning that the thickness of the lamellae were in a closer range. Table 5.1 shows the parameters obtained from DSC before and after annealing. The lamellae thickness was calculated according to the Gibbs-Thomson equation [97] using following parameters for PET: fold surface energy  $\sigma_e=0.106 \text{ J/m}^2$  [121], equilibrium melting point of purely crystalline PET  $T_m^0=564 \text{ K}$  [121], heat of fusion of an ideally crystalline sample  $\Delta H^0=140 \text{ J/g}$  [122], based on the density of perfect crystalline PET  $\rho_c=1.514 \text{ g/cm}^3$ . Interestingly, the glass transition temperature is strongly reduced upon crystallization.

Similar to the experiment with PP, the sample was pre-deformed by cold rolling to a true strain of  $\varepsilon=0.6$ , subsequently storing it in liquid nitrogen. After mounting it to the temperature stage, it was then measured at different annealing temperatures while each temperature was kept constant for 600s. Figure 5.12 shows a selection of diffraction patterns, which undergo a peak shift to smaller  $2\Theta$  angles caused by a relaxation of the lattice.

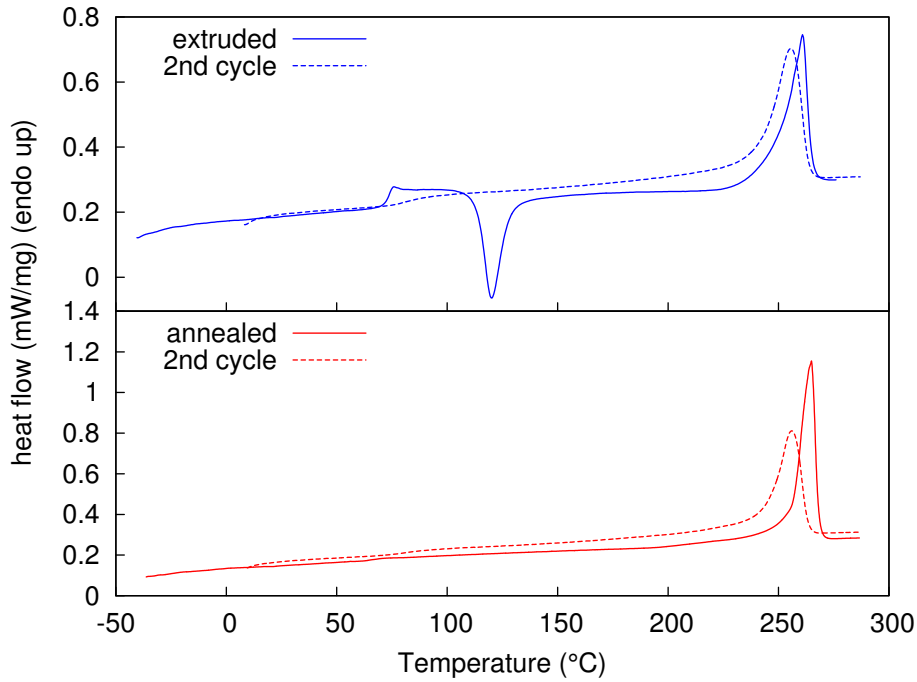


**Figure 5.11:** DSC traces of the as received, extruded sample (blue), and the same material after crystallization for 5h at 185 °C.

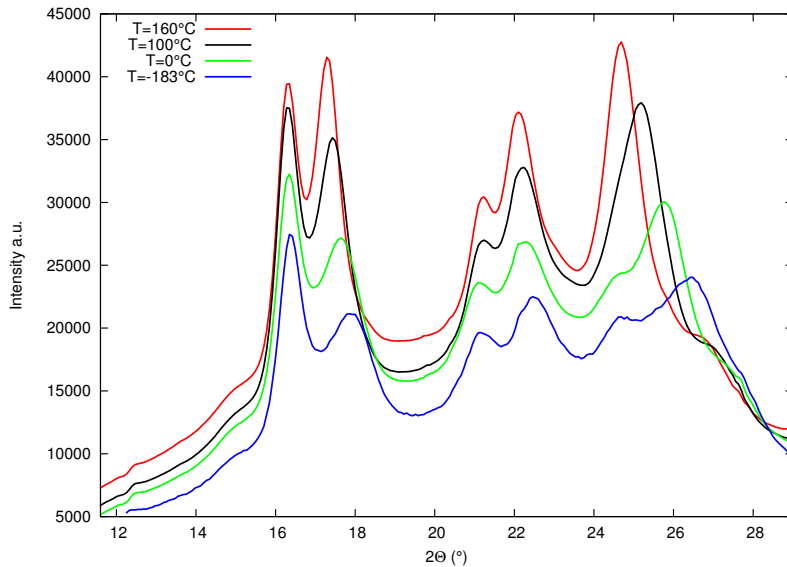


**Figure 5.12:** A peak shift is observed with increasing annealing temperature due to relaxation of the crystalline lattice.

After the phase separation process, and the XLPA evaluation, dislocation density and CSD-size were obtained as a function of annealing temperature (figure 5.13 and 5.14). Compared to other semicrystalline polymers, such as  $\alpha$ -iPP, the initial dislocation density of the highly strained, pre-deformed sample, is comparatively low with  $\rho = 3.5 \times 10^{15} \text{ m}^{-2}$ , indicating that the contribution of dislocations to crystalline plasticity is less pronounced. Nevertheless, a

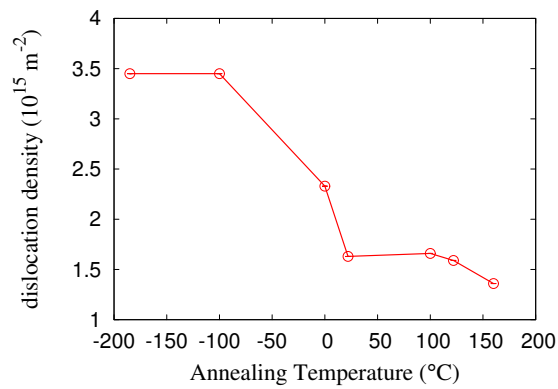


**Figure 5.13:** A drop in dislocation density is observed reaching a temperature of 25 °C, most probably due to a reduction in backstresses of the amorphous phase. Errors are in the order of the point size.

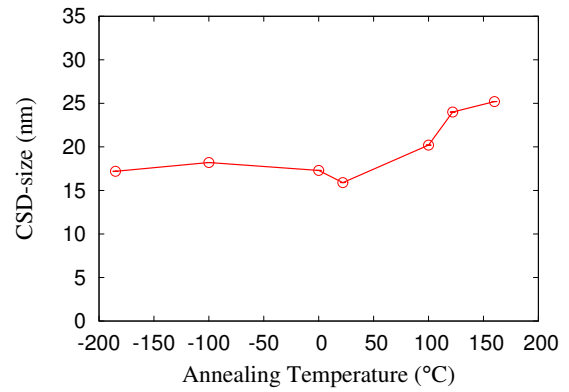


**Figure 5.14:** The CSD-size stays relatively constant up to  $T=25$  °C, followed by an increase to 25 nm as a result of crystallization processes, or recrystallization of small angle grain boundaries. Errors are in the order of the point size.

significant decrease of the dislocation density can be observed when a temperature of approximately  $T=25$  °C is reached. The CSD-size depicted in figure 5.14 indicates an initial value of 17 nm which stays constant up to 25 °C. Reaching an annealing temperature of 100 °C the domain size increases up to 25 nm.

## 5.2 Crystalline plasticity below and above the glass transition temperature

This section concentrates on the investigation of the role of the amorphous phase and its interplay with the crystalline domains during high plastic deformation, by selectively varying the rigidity of the amorphous phase. Therefore, in-situ compression experiments were performed on isotactic polypropylene below the glass transition temperature during simultaneous X-ray diffraction using synchrotron radiation. Isotactic polypropylene with a high content of  $\alpha$ -phase was used for the investigation, since it could be shown in previous studies, that dislocations strongly contribute to its deformation mechanism [17–19, 23]. For the experimental setup, the curved *INEL CPS 590* detector was chosen, while the sample was compressed using the miniature compression machine (figure 4.3). During the whole experiment, the sample was kept below its  $T_g$  of 10 °C at -5 °C using an *Oxford Cryostream* cooler. The deformation mode was compression, which allowed to reach high strains, simultaneously avoiding the occurrence of cavitation. The sample was then deformed stepwise to different degrees of deformation, up to a true strain of  $\varepsilon = 0.8$  at a true strain rate of  $\dot{\varepsilon} = 10^{-3} s^{-1}$ , while the deformation was interrupted every time a diffraction pattern was recorded. Additionally, a diffraction pattern was recorded of the undeformed sample at a room temperature of 24.8 °C before it was cooled below its  $T_g$ . The development of the microstructural parameters obtained by the MXPA-method were then compared to the same experiment, performed at room temperature, above  $T_g$ .

The recorded diffraction patterns were first analysed with respect to their phases using the procedures and programs mentioned in section 4.5. Hereby the small amount of  $\gamma$ -phase was modelled (figure 5.15) and then removed for the subsequent XPA evaluation.

The yield stress found during compression below  $T_g$  was 120 MPa, considerably higher compared to similar experiments performed above  $T_g$  which can be attributed to the increased stiffness of the amorphous phase.

Prior the MXPA evaluation, all diffraction patterns were analysed using the Williamson-Hall and its modified version. Figure 5.16 shows the WH and MWH plot for the sample deformed below  $T_g$ . Two representative strains were chosen for the plot, which are  $\varepsilon_{true} = 0$  for the undeformed sample and the highly deformed sample with  $\varepsilon_{true} = 0.8$ . The non-monotonous behaviour of the peak width with increasing diffraction order already points at lattice distortions, caused by the presence of dislocations. This is confirmed in the MWH-plot where a linearisation is achieved by introducing the dislocation contrast factor. According to equation 4.6, the dislocation density is proportional to the slope of the fit, while the CSD-size is determined by the intercept of the fit with the ordinate.

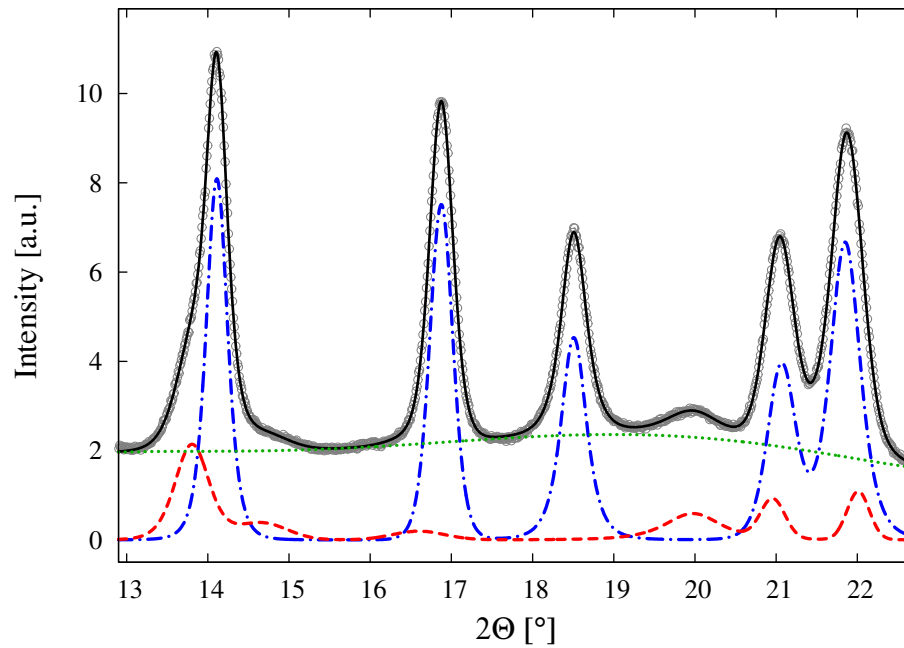


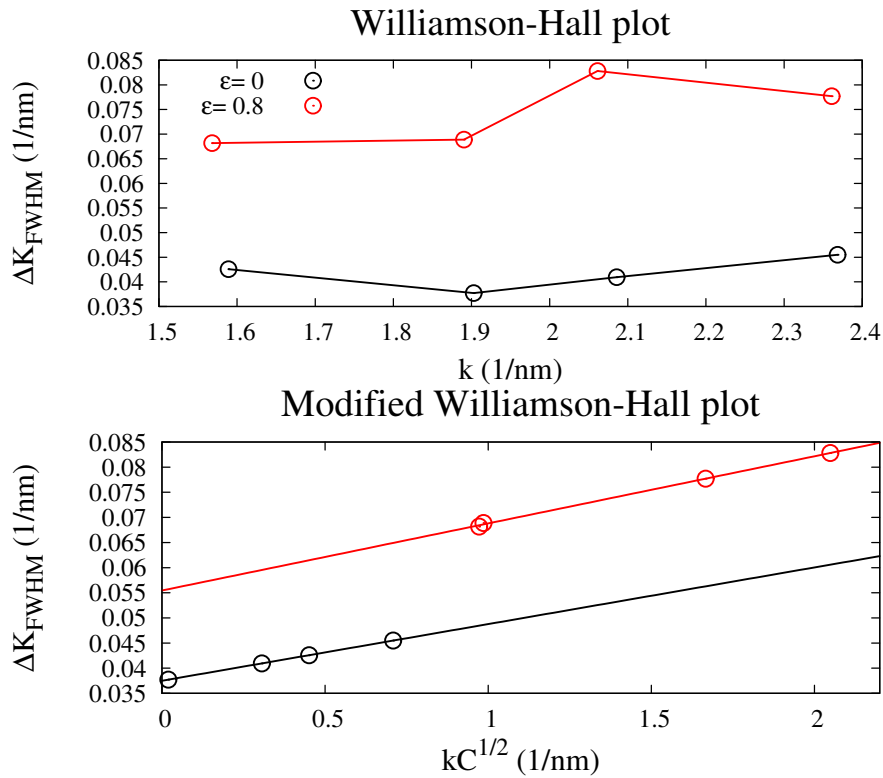
**Figure 5.15:** WAXS pattern of undeformed iPP below  $T_g$ . Measured data (o), fit (full line),  $\alpha$ -phase (dash-dotted line),  $\gamma$ -phase (dashed line) and amorphous phase (dotted line).

Interestingly, it is found that the undeformed and highly deformed sample have only marginally differing dislocation densities, which is  $\rho = 1.7 \cdot 10^{15} \text{ m}^{-2}$  and  $\rho = 2.3 \cdot 10^{15} \text{ m}^{-2}$  for the undeformed and deformed sample respectively. The change in the CSD-size, however, is found to be more significant, since a decrease from initially 24nm to 16nm is obtained by the modified WH-analysis (figure 5.16).

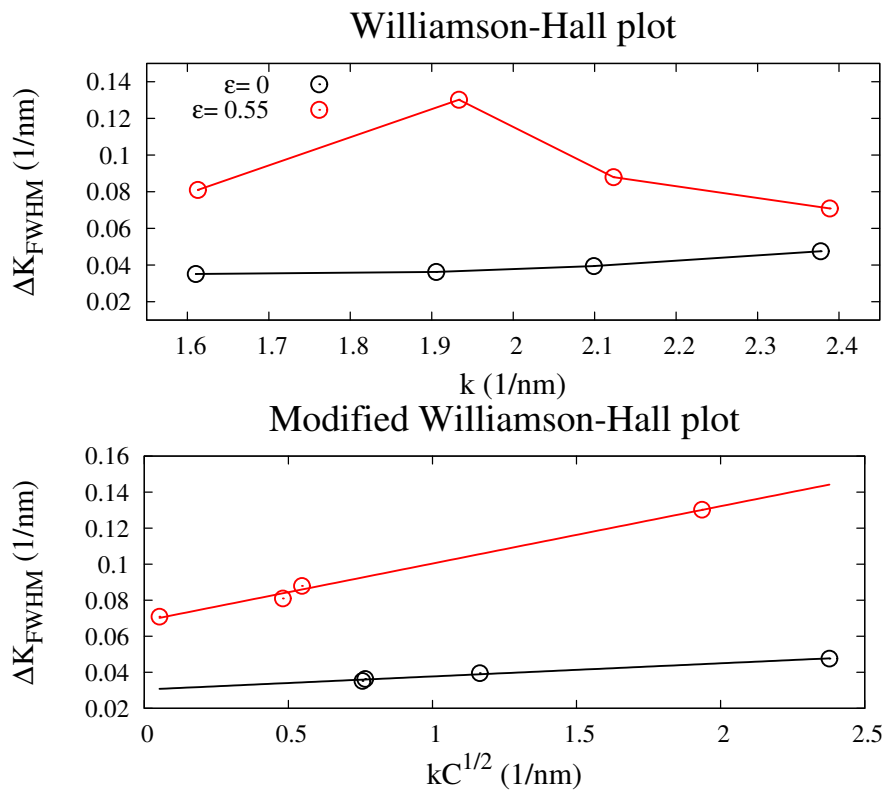
If these results are compared to the experiments performed above  $T_g$  (figure 5.17), a different behaviour can be observed. Here, the undeformed sample shows an increase in dislocation density from  $\rho = 6.6 \cdot 10^{14} \text{ m}^{-2}$  to  $\rho = 1.4 \cdot 10^{16} \text{ m}^{-2}$  for the sample deformed to a true strain of  $\varepsilon = 0.55$ , accompanied by a decrease in CSD-size from 29nm to 13nm.

Figure 5.18 shows the final result of the dislocation density development obtained from each recorded diffraction profile, using the MXPA method. Considering the sample deformed at room temperature (above  $T_g$ ), a pronounced increase starting at a true strain of approximately  $\varepsilon = 0.2$  from  $\rho = 0.5 \cdot 10^{15} \text{ m}^{-2}$  to  $\rho = 1.6 \cdot 10^{16} \text{ m}^{-2}$  is observed. The change of the dislocation density for the sample deformed below  $T_g$ , in spite, is only moderate, revealing an increase from  $\rho = 1 \cdot 10^{15} \text{ m}^{-2}$  to about  $\rho = 2.6 \cdot 10^{15} \text{ m}^{-2}$ . The dislocation densities obtained by the MXPA-method are very close to the results obtained from the MWH-evaluation, for both experiments.

A decrease of the CSD-size was found at both deformation temperatures, from 20nm to 12nm for the sample deformed above  $T_g$  and from 23 nm to 14 nm for the low temperature experiment (figure 5.19).



**Figure 5.16:** WH and MWH-plot for the undeformed and deformed sample cooled below  $T_g$ , showing a similar dislocation density in both cases



**Figure 5.17:** In contrast to the sample deformed below  $T_g$ , an increase in dislocation density is observed at higher degrees of deformation in case of the room temperature experiment

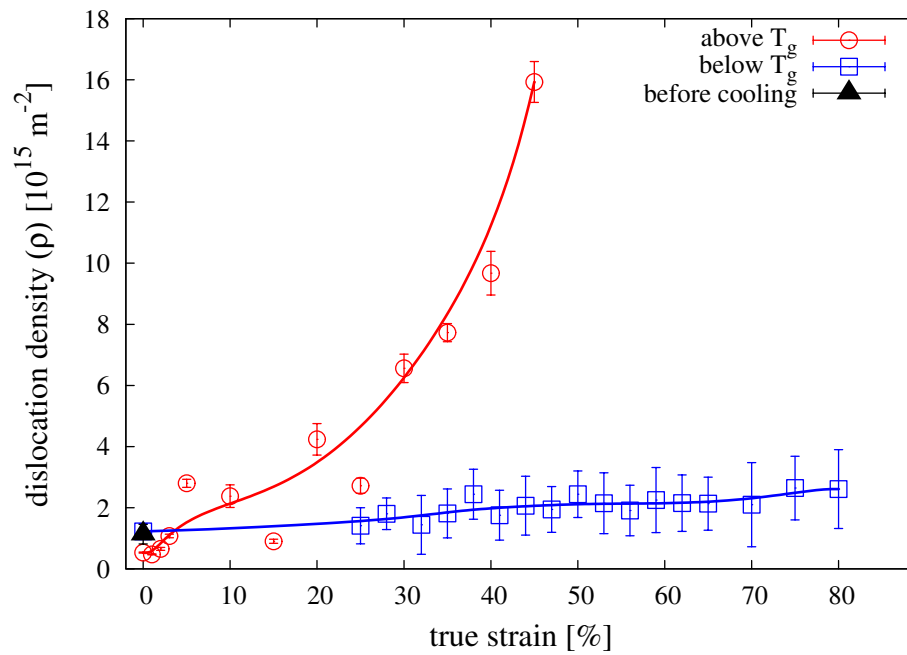


**Figure 5.18:** Development of the dislocation density of  $\alpha$ -iPP at room temperature and below its glass transition. The black triangle indicates the dislocation density obtained for the unloaded sample at a temperature of 24.8 °C before cooling below  $T_g$ .

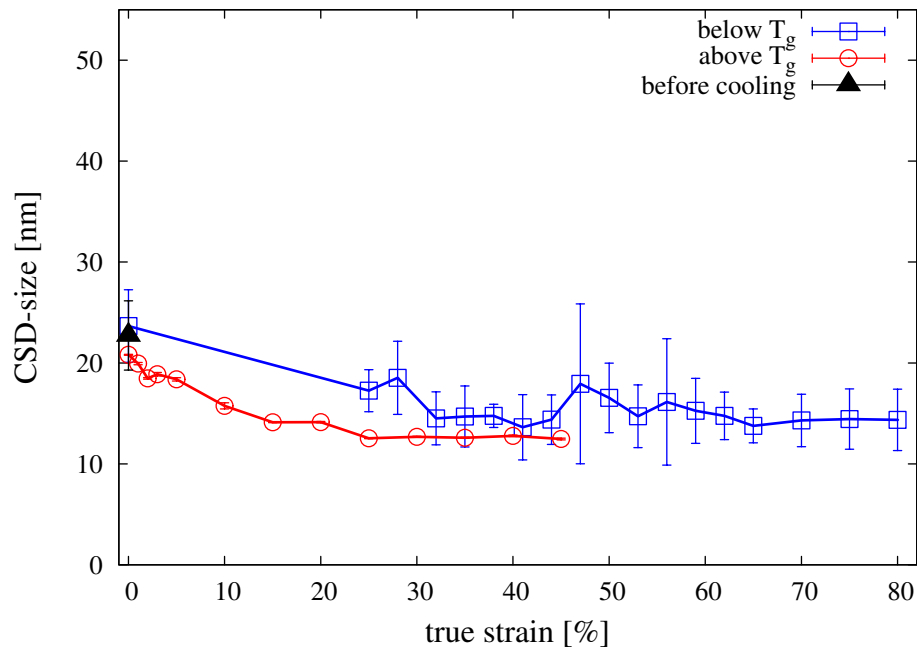


**Figure 5.19:** Coherently scattering domain size (CSD-size) as a function of true strain. The black triangle indicates the CSD-size obtained for the unloaded sample at a temperature of 24.8 °C before cooling below  $T_g$ .

Crystallinity as evaluated from X-ray diffractograms was found to decrease from initially 66 % to a value of 52 % at a plastic deformation of  $\varepsilon = 0.8$  for the sample deformed below  $T_g$  and from 56 % to 43 % for the room temperature experiment.

### 5.2.1 Application of the Momentum Method to PE

In contrast to PP, the diffraction pattern of PE only shows two high intensity peaks in case of an undeformed state, which is the (110) and (200) reflection [123] (figure 5.20). Due to the presence of only two peaks, multi-reflection methods including CMWP cannot be applied, here the momentum method is the appropriate tool, since it allows to determine the same physical quantities out of a single line profile (section 4.3.3).

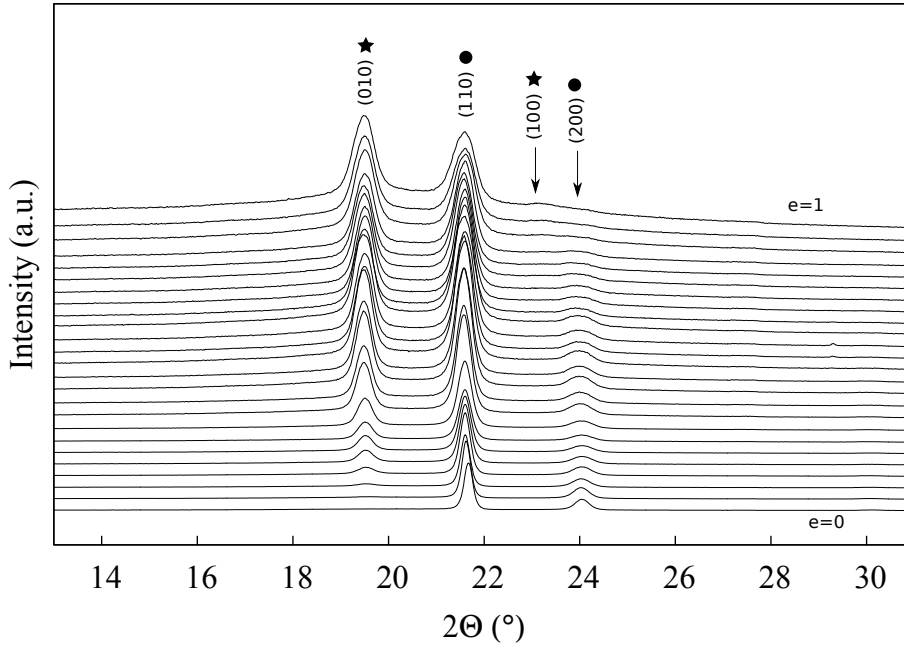


**Figure 5.20:** Comparison of diffraction patterns obtained for the undeformed and highly strained sample (background subtracted). The formation of a hexagonal phase was already observed at a true strain of  $\varepsilon = 0.05$ . (hexagonal phase (☆), orthorhombic phase (●))

PE was compressed in-situ during simultaneous X-ray diffraction using synchrotron radiation. Similar to the experiment in section 5.2, diffraction patterns were recorded at different degrees of plastic strain, while the sample was still under load. The experimental setup consisted of a miniature compression machine and a curved INEL CPS 590 detector (section 4.4), while the sample was deformed up to a true strain of  $\varepsilon = 1$  using a strain rate of  $\dot{\varepsilon} = 10^{-3} \text{ s}^{-1}$ . After each deformation step, the measurement was just started after the first sudden decrease in stress occurred.

Figure 5.20 shows diffraction patterns obtained at different strains. While in the undeformed case only two reflections of the orthorhombic phase can be observed, an additional phase appears already at a true strain of  $\varepsilon = 0.05$ . It is known that a hexagonal phase is obtained during high pressure crystallization as a result of chain extended growth [124], a monoclinic phase was reported in the case of pressures exceeding 300 MPa and/or deformation by rolling [125].

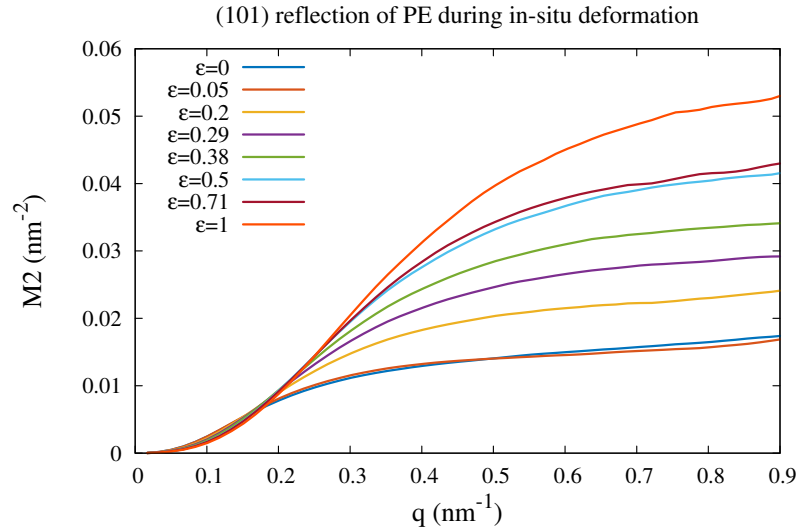


**Figure 5.21:** Development of the second order moment for different true strains.

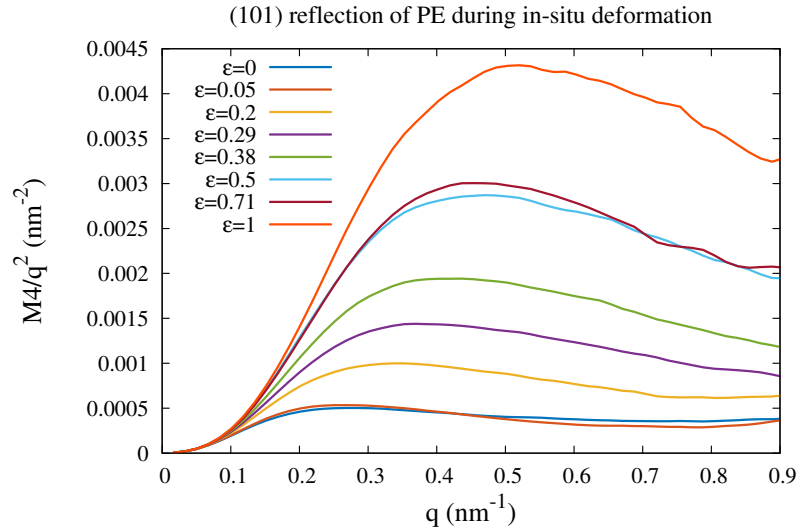


**Figure 5.22:** Development of the fourth order moment divided by  $q^2$  for different degrees of deformation.

Due to its high intensity, the orthorhombic (110) reflection was used for the XLPAs evaluation. The  $k$ th order restricted moments are obtained according to equation 4.7, discussed in section 4.3. Figures 5.21 and 5.22 show the individual plots for M2 and M4 respectively as a function of  $q = 2/\lambda(\sin\Theta - \sin\Theta_0)$  obtained for PE compressed to different true strains. Considering M2 in figure 5.21, a logarithmic behaviour is found, while an increase of the M2 signal is obtained with increasing deformation. Figure 5.22 shows the fourth order restricted moments of the (110) reflection at different degrees of deformation. Similarly to M2, an increase in magnitude of the M4 signal is found with increasing deformation.



# Chapter 6

## Discussion

### 6.1 Meaning of molecular relaxations with special respect to dislocation movement

In section 3.2 it was already pointed out that plastic deformation is governed by dislocation movement and generation. However, there are some exceptions like the  $\gamma$ -phase of PP, where the non-parallel chain structure leads to an increased CRSS and hence the interlamellar shear becomes the predominant deformation mechanism [17]. A similar behaviour was found in the case of poly(3-hydroxybutyrate) (P3HB), where the dislocations density does marginally change with increasing deformation [18, 20]. This behaviour could be related to bulky side groups, which hinder the crystallographic slip and as well result in a high brittleness of the material. These experiments have in common, that they investigated the evolution of the dislocation density at room temperature. The following section will discuss the temperature dependent in-situ experiments as introduced in section 5.1 giving insight in dislocation kinetics at polymer specific transition temperatures. This allows to study the interplay of the crystalline and amorphous phase in a new context and also the role of molecular relaxations by combining XLPA with DMA data.

#### **Influence of transition temperatures on the dislocation density**

By plotting the dislocation density obtained by the MXPA evaluation (figure 5.7 from section 5.1) together with the loss factor ( $\tan(\delta)$ ) obtained by DMTA at 1 Hz (figure 5.9b from section 5.1), changes in defect concentration can be observed at specific transition temperatures originating from molecular relaxations. As mentioned in subsection 3.3.2, molecular relaxations have already been rigorously investigated for PP while three main transitions,  $\alpha$ ,  $\beta$  and  $\gamma$ , could

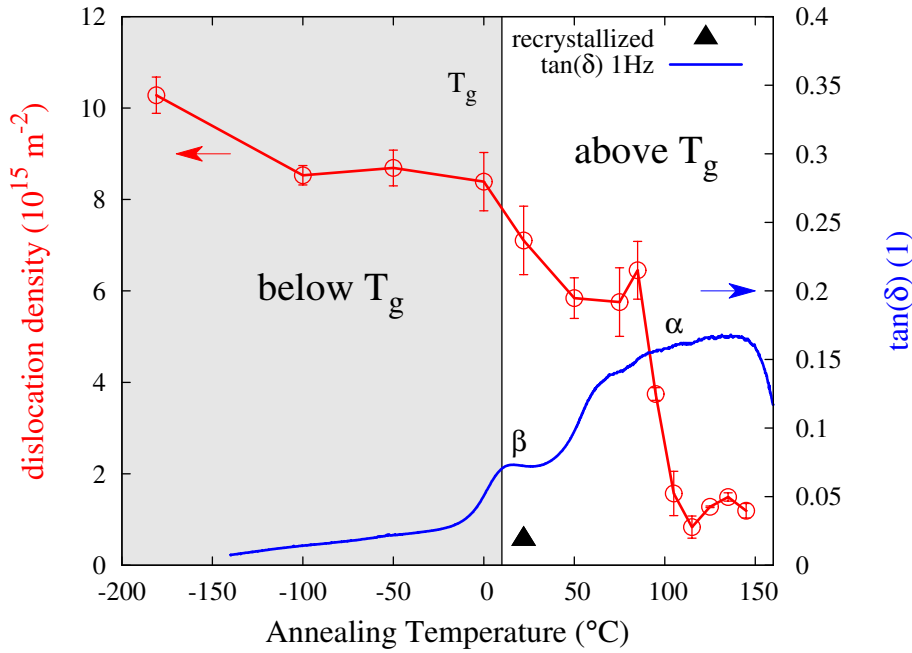


**Figure 6.1:** Comparison of the loss tangent signal and the evolution of the dislocations density as a function of annealing temperature. A significant drop in the defect concentration can be observed at the glass transition temperature  $T_g = 10^\circ\text{C}$  and beyond  $85^\circ\text{C}$  (red curve), which correspond to the  $\beta$  and  $\alpha$ -relaxation respectively. Loss factor  $\tan(\delta)$  measured by DMTA with a frequency of 1Hz (blue curve). The error of the recrystallized sample (black triangle) is in the order of the point size.

be identified in this order with decreasing temperature [126]. Using dielectric spectroscopy a fourth relaxation located at a temperature below 100 K was reported known as the  $\delta$ -relaxation [85, 93, 94].

However, in the  $\tan(\delta)$  curve of the deformed sample in figure 6.1 only two transitions, the  $\alpha$  and the  $\beta$ -transition could be detected, while the weak  $\delta$ -transition could not be resolved during mechanical spectroscopy. The origin of the  $\alpha$ -transition can be attributed to both, the amorphous and the crystalline phase, when it is supposed that the intensity of this transition is controlled by an interchange of chain segments between the crystalline and the amorphous phase. A possible explanation of such a mechanism is given by a molecular model based on chain twist defects (figure 6.2), already discussed in section 3.3.2. Such a defect-based relaxation mechanism within the crystalline phase may cause a strong reduction of the dislocation density when the defect propagates along the chain axis into the adjacent amorphous phase. As a consequence, a translation of the chain stems occurs by the distance of a Burgers vector, resulting in a surface modification consisting of shortening of the chain loops (figure 6.3). This in further consequence allows for an extension of tie chains permitting additional deformation of the amorphous phase resulting in an increase in the  $\tan(\delta)$  signal [77, 127, 128].

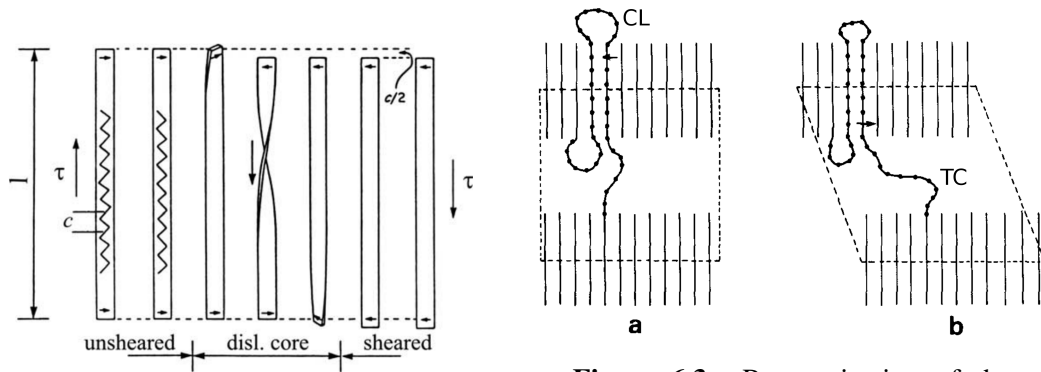


**Figure 6.2:** Under the application of a shear stress  $\tau$ , crystal slip occurs with a Burgers vector  $b=c/2$  occurs due to propagation of a  $180^\circ$  chain twist defect [63, 77].

**Figure 6.3:** Reorganization of the crystal interface occurs by (a) shortening of chain loops (CL), which permits (b) lengthening of tie chains (TC) permitting additional deformation of the amorphous phase (modified from [77])

This explanation is supported by figure 6.4 which shows a comparison of the  $\tan(\delta)$  signal for an undeformed and deformed sample. It is apparent that the intensity of the signal is strongly increased in case of the deformed sample. Considering that the mechanical  $\alpha$ -process can be related to inter- and intralamellar shear processes which stimulate the transfer of chain segments from the crystalline to the amorphous phase, it is plausible that the peak broadening and/or increase in intensity occurs for one or both of the corresponding  $\alpha_1$  and  $\alpha_2$  relaxations in the mechanical loss spectra [83]. The higher the initial dislocation density is in the deformed sample, more chain segments are being transported to the amorphous phase via propagating twist defects. However, the stronger  $\alpha$ -signal may also be caused by the higher initial fraction of the amorphous phase since it is well known that crystallinity decreases with increasing deformation.

However, it has to be considered that the chain twist mechanism only operates in chain direction, along the c-axis. Yet, previous investigations show that with increasing deformation also dislocations with screw and edge character operating in transverse direction are activated [22]. Consequently, and according to figure 6.1, it is possible not only that the reduction in dislocation density, but also the intensity of this  $\alpha$ -transition is not only caused by dislocations with chain character, but also by dislocations with transverse character.

While the  $\alpha$ -transition is attributed to an interplay of the amorphous and crystalline phase, the  $\beta$ -transition was related to relaxations in the amorphous component solely [90]. The assignment of the  $\beta$ -relaxation to the glass transition temperature in PP was also supported by the higher activation energy compared to the  $\alpha$ -relaxation (table 6.1). The decrease of the dislocation density around the glass transition temperature can be explained in terms of a reduction in

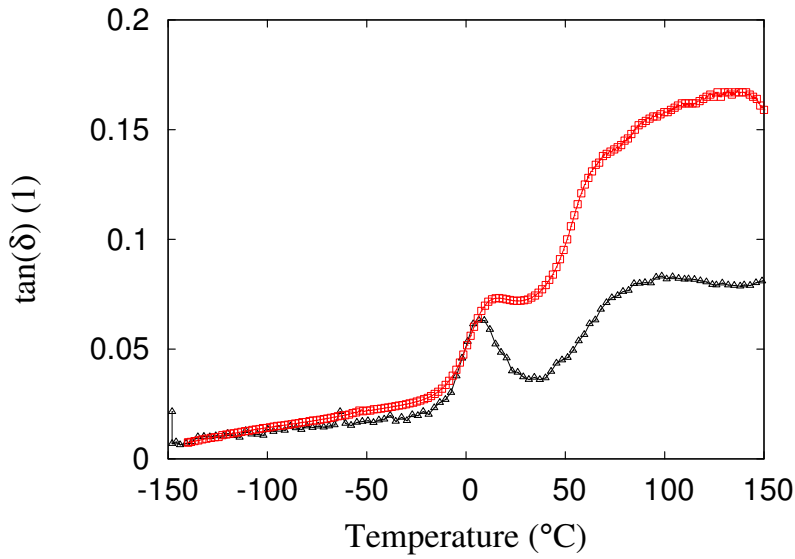


**Figure 6.4:** Loss factor curves for the undeformed ( $\varepsilon=0$ , black triangles) and deformed ( $\varepsilon=1.2$ , red squares) samples at a test frequency of 1Hz.

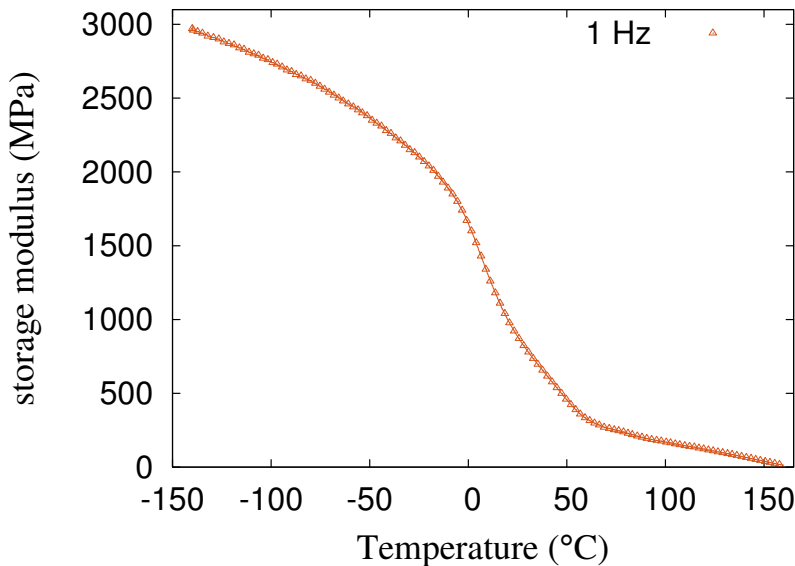


**Figure 6.5:**  $E'$  measured at 1 Hz at a heating rate of 2 °C/min

backstresses acting on the crystalline phase. Below  $T_g$ , the material is still highly strained from the rolling procedure. The fact that the sample was subsequently cooled to  $-180^\circ$  after deformation prohibited any intermittent sample relaxation, thus, “freezing” a large amount of stresses within the material. It can be assumed that a significant part of these stresses in the amorphous phase is transmitted to the neighbouring crystallites, thus stabilizing the dislocations therein. Increasing the temperature above  $T_g$ , therefore results in an increase of chain mobility and free volume in the amorphous phase accompanied by a simultaneous decrease in its modulus. Figure 6.5 shows the evolution of the storage modulus  $E'$  as a function of temperature. The dissipating

**Table 6.1:** Comparison of activation energies for the  $\alpha$  and  $\beta$ -relaxation process in polypropylene.

$E_{a,\alpha}$ (kJ mol <sup>-1</sup> )	$E_{a,\beta}$ (kJ mol <sup>-1</sup> )	
225	> 400	[129]
158	358-364	[130]
163-205	167-234	[131]
222	246-497	[132]
110-170	380	[82, 133]

backstresses facilitate dislocation mobility, which results in a reduction in dislocation density by their annihilation or propagation into the adjacent amorphous phase.

Here, the activation energy of the process is provided by both, back-stresses and thermal energy, in contrast to the dislocation density reduction at the  $\alpha$ -relaxation, where the whole activation energy is provided thermally.

The activation energy was evaluated for the  $\alpha$  and  $\beta$ -relaxation of the undeformed sample and for the  $\beta$ -relaxation of the deformed sample, by means of a frequency dependence which was found for both transitions due to thermal activation. With increasing frequency a reduction in the intensity of the signal and a shift of the transition temperature to higher temperatures must be observed. The temperature dependence of a relaxation process which occurs at a temperature ( $T$ ) and its excitation frequency ( $f$ ) is therefore used to determine the corresponding activation energy ( $E_a$ ) of this process, which is given by the Arrhenius equation:

$$f = f_0 \cdot e^{-\frac{E_a}{RT}}. \quad (6.1)$$

Here,  $f_0$  is a pre-exponential factor and  $R$  is the gas constant ( $R=8.314 \text{ JK}^{-1}\text{mol}^{-1}$ ). By plotting the logarithm of the different frequencies against the temperature at which the transition is observed, the activation energy is obtained by the slope of a linear fit, which can be seen by logarithmizing equation 6.1 and in figure 6.7.

$$\ln(f) = \ln(f_0) - \frac{E_a}{R} \cdot \frac{1}{T}. \quad (6.2)$$

Table 6.2 shows the values for  $E_a$  obtained for the transition temperatures, which are similar to those reported in literature (table 6.1). A slight increase in the activation energy is found for the  $\beta$ -transition in case of the deformed sample. As can be seen in figure 6.6 for the deformed sample, the  $\alpha$ -relaxation spans a temperature range from about 40 °C up to several degrees below the melting temperature of  $T_m=164.6$  °C (peak temperature), obtained by DSC analysis. This on the one hand implies that this transition is indeed composed of at least two subtransitions, such as the  $\alpha_1$  and  $\alpha_2$ -transition, however, on the other hand, their evaluation in terms of

**Table 6.2:** Activation energies for the  $\alpha$ - and  $\beta$ -relaxation for the undeformed and deformed sample

	$E_{a,\alpha}$ (kJ mol <sup>-1</sup> )	$E_{a,\beta}$ (kJ mol <sup>-1</sup> )
$\varepsilon = 0$	160	368
$\varepsilon = 1.2$	-	409

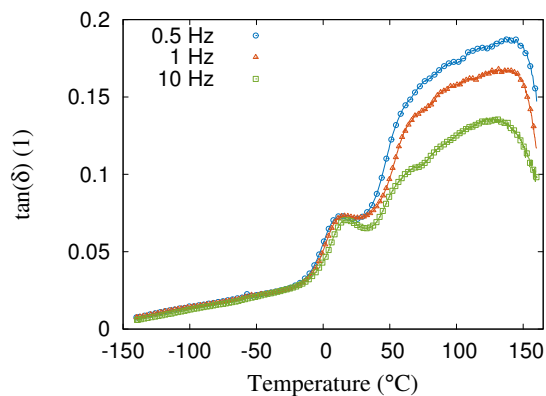


**Figure 6.6:** Loss tangent versus temperature of samples deformed to  $\varepsilon=1.2$  for three different test frequencies.

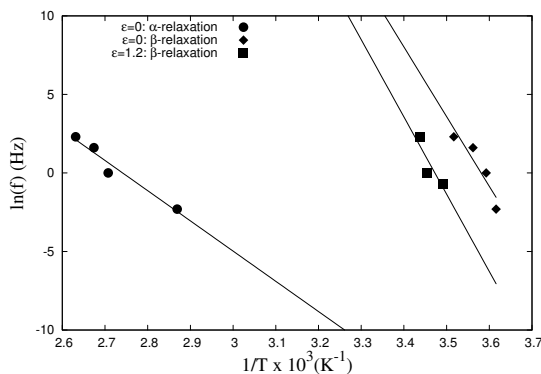


**Figure 6.7:** Arrhenius plot of the  $\alpha$  and  $\beta$ -relaxation for the undeformed and deformed samples.

activation energy is complicated. By fitting the  $\alpha$ -transition by an  $\alpha_1$  and  $\alpha_2$  peak it is found that with increasing frequencies, a shift to lower temperature occurs. According to equation 6.1, this would result in a negative activation energy.

The  $\gamma$  and  $\delta$ -relaxation, usually observed between  $-120$  °C to  $-50$  °C and  $-240$  °C to  $-173$  °C respectively in case of PP [85, 132], could not be resolved by DMTA in torsion mode. Although the initial drop in dislocation density (figure 6.1) is located in the same temperature range as the two transitions below  $T_g$ , it is not clear whether they are the reason for the decrease in defect concentration at this temperature. Especially the  $\delta$ -relaxation with its low activation energy of  $4.2$  kJ mol<sup>-1</sup> to  $5$  kJ mol<sup>-1</sup> which is attributed to small vibrations of  $\text{CH}_3$  groups can not be considered as eligible to represent comparatively large rearrangements which are necessary for dislocation movement such as a chain twist.

While the dislocation density was observed to drastically change between  $-180$  °C and  $100$  °C, the CSD-size changed only slightly over the same temperature range (figure 6.8) which must be considered as being close to the experimental error of the method. The following increase from  $13$  nm to  $16$  nm most probably originates from recrystallization processes. A possible mechanism is the recrystallization of small angle grain boundaries or small misorientations within crystalline lamellae which are formed by geometrically necessary misfit dislocations upon bending of the lamellae during deformation [17].

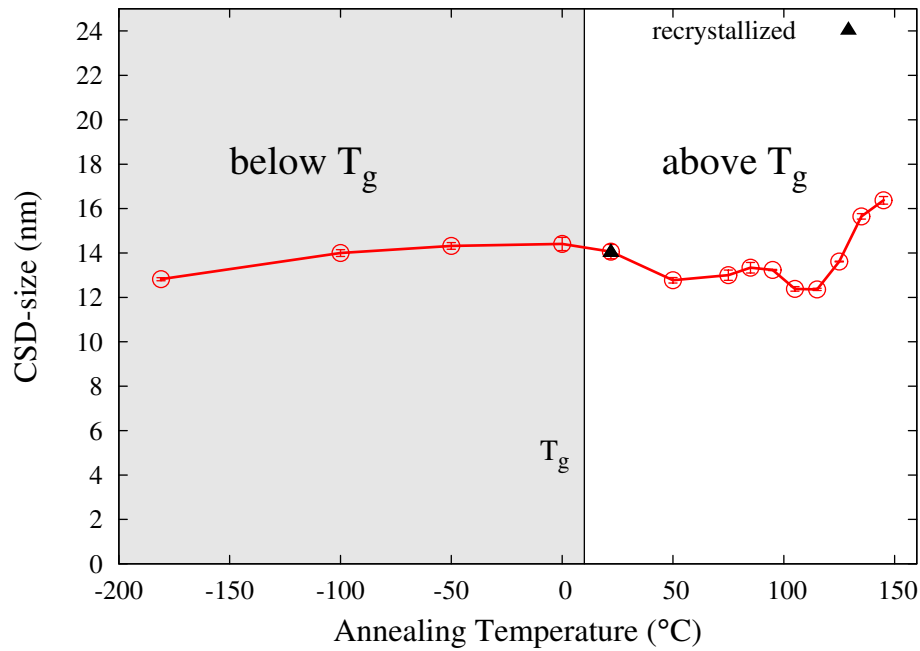


**Figure 6.8:** The domain size only changed slightly up to about 100 °C which can be considered to be within the experimental error. The stronger increase at 100 °C is caused by recrystallization of small angle grain boundaries. The error bars are in point size, which indicates well converging fits for the different starting parameters.

### Polyethylene terephthalate (PET)

In case of PET it was already shown in section 5.1 (figure 5.13) that a significant decrease of the dislocation density from  $\rho = 3.5 \times 10^{15} \text{ m}^{-2}$  to  $\rho = 1.5 \times 10^{15} \text{ m}^{-2}$  is observed upon annealing when reaching a temperature of approximately  $T=25 \text{ }^\circ\text{C}$  (figure 6.10). According to DSC scans this temperature is still below the glass transition of  $66 \text{ }^\circ\text{C}$ , which is somewhat surprising when this result is compared with the strong decrease of dislocation density just occurring at the glass transition temperature in PP. It has to be mentioned here that the modified WH method, where the only input parameter is the FWHM, seems to be distinctly less reliable than the CMWP approach fitting the whole profiles of the entire diffraction pattern, and may show results being markedly different from those of CMWP. This can be seen clearly by a direct comparison of the two methods applied to deformed iPP (figure 6.9). Similarly to the case of PET, an early and smooth decrease of dislocation density can be seen although the CMWP indicates a markedly stepwise annealing behaviour also being in parallelism to the DMA results. So it can be assumed that PET shows a dislocation annealing characteristic being similar to that of PP, at the glass transition temperature. A more direct conclusion is not possible as CMWP does not work for triclinic lattices so far; perhaps the use of DMA may yield further evidence for this conclusion. The CSD-size development in figure 5.14 and figure 6.10 was found to be constant up to a temperature of  $25 \text{ }^\circ\text{C}$ , followed by an increase up to 25 nm approaching 100

°C, most probably due to crystallization processes in the material, or similar to the experiment performed with PP, due to a recrystallization of small angle grain boundaries, leading to larger coherently scattering domains.

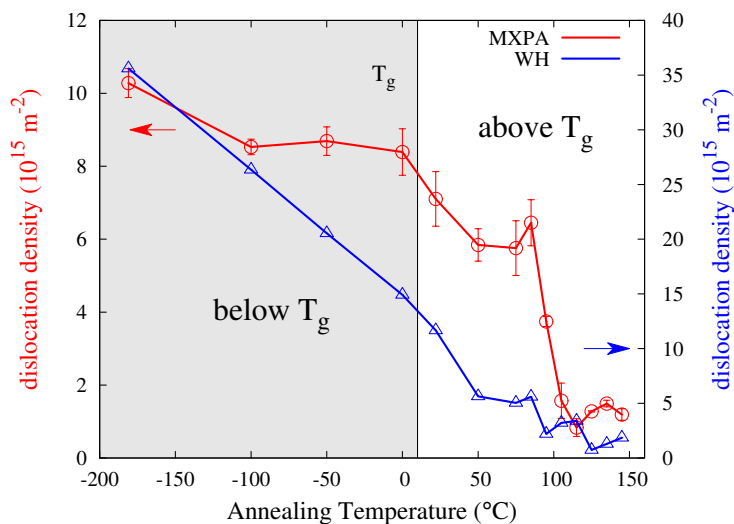


**Figure 6.9:** Comparison of the dislocation density development in PP during annealing, evaluated by the WH-method (blue curve) and by the MXPA-method (red curve).

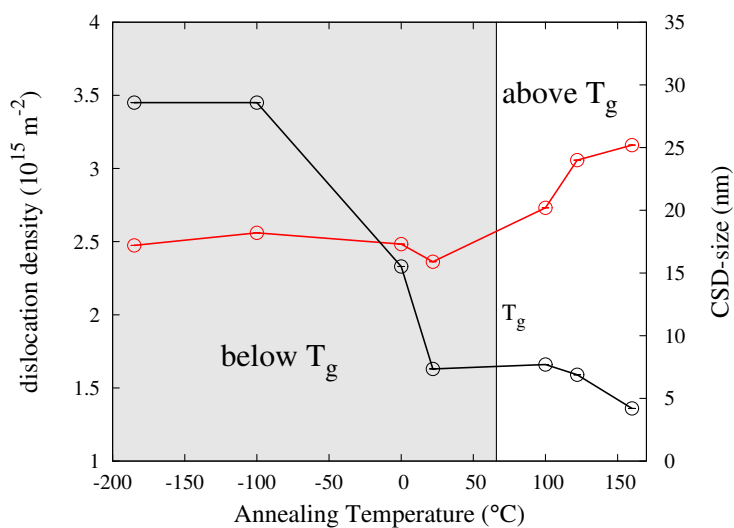


**Figure 6.10:** CSD-size and dislocation density development in PET. Numerical errors are of the order of the point size.

The dislocation density of  $\rho = 3.5 \times 10^{15} \text{ m}^{-2}$  prior to annealing is comparatively low compared to other semicrystalline polymers, such as  $\alpha$ -iPP. This may have several reasons. One possibility is that the complex chain structure involving benzyl groups and oxygen hinder the propagation of crystalline defects. Considering dislocations in terms of chain twist defects, it would be plausible that  $180^\circ$  chain twists cannot be formed due to the bulky side groups.

In case of poly(3-hydroxybutyrate) (P3HB) a similar behaviour could be observed [18]. In this latter case the dislocation density did not change upon in-situ compression, instead, P3HB tended to form macroscopic cracks with increasing deformation which led to destruction of the crystalline lamellae before crystallographic slip could occur.

Another explanation is that the PET-material has been pre-deformed at room temperature of about 22 °C which is markedly below its  $T_g$  of 66 °C. Hence, the amorphous phase is not soft enough in order to allow for interlamellar rotations of the crystalline domains. Thus the rearrangements of lamellae are hindered unless a position is reached where the Schmid-factor is high enough to initiate crystallographic slip, usually accompanied by dislocation generation and motion. More light upon this effect is shed within the following section, where the influence of the amorphous phase on crystalline plasticity is systematically investigated.

## 6.2 Influence of rigidity of amorphous phase to the dislocation activity

It could be shown in the previous section that strains from the amorphous phase (back-stresses), which are transmitted to the crystalline lamellae, stabilize dislocations within the crystalline phase. However, the role of the amorphous phase with special respect to dislocation generation *during* high plastic deformation was unclear so far. In order to clarify this question, the contribution of a dislocation mediated plastic deformation mechanism operating within the crystalline phase, has been investigated with special consideration of the varying rigidity of the amorphous phase. For this purpose in-situ compression experiments during simultaneous X-ray diffraction using synchrotron radiation, were performed on isotactic polypropylene below  $T_g$ .

It was already shown in section 5.2 that considerable differences in the development of the dislocation density can be found when the sample is deformed below or above its  $T_g$  (figure 6.11). This implies that different deformation mechanisms are active at different deformation temperatures.

The importance of dislocations for plastic deformation and the related basic mechanisms were already discussed in section 3.2. However, the key points will be recapitulated throughout this section to ensure a coherent explanation of the results obtained above.

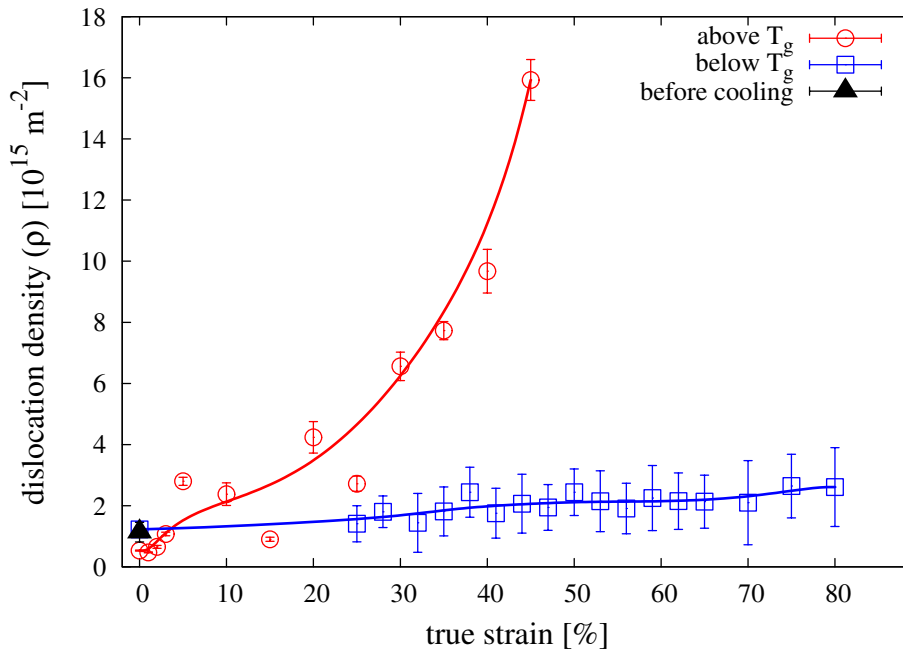


**Figure 6.11:** Development of the dislocation density of  $\alpha$ -iPP at room temperature and below its  $T_g$ . The black triangle indicates the dislocation density obtained for the undeformed sample at a temperature of 24.8 °C before cooling below  $T_g$ .

Due to the multiphase amorphous - crystalline morphology and the presence of tie molecules, acting as additional stress transmitters, both phases are subjected to deformation. An important difference, with respect to the deformation temperature is, that in case of deformation above  $T_g$ , the amorphous phase acts as an additional slip system. Thus, the crystalline lamellae can rearrange by one or more amorphous deformation modes, as discussed in section 3.2.1. From section 3.2 we know that in case of semicrystalline polymers, such as  $\alpha$ -iPP, deformed above its  $T_g$ , crystallographic slip is a basic mechanism operating over the whole strain range, especially within the plastic regime [53, 67]. This crystal slip is further accompanied by dislocation generation and motion. However, dislocations only move if the critical resolved shear stress  $\tau_0$  is reached within the slip plane, which is expressed by Schmid's law and depends on the orientation of the slip plane normal and the slip direction with respect to the applied stress (section 3.2.2). Combining these facts, the development of the dislocation density (figure 6.11), for the sample deformed above  $T_g$  can be explained.

At small strains, one or more of the amorphous deformation modes dominate. Hence, the crystalline lamellae reorganize but not yet deform plastically by a significant amount; thus, dislocation activity is poor. With proceeding deformation, the hard crystalline lamellae still undergo rearrangements as they are embedded in a soft amorphous matrix, therefore, the number of slip planes which reach  $\tau_0$  increases due to lamellae rotation and increasing uniaxial stress. This way an increased crystallographic slip governed by dislocation generation and motion occurs,

particularly when a true strain of  $\varepsilon = 0.25$  is exceeded (figure 6.11).

During deformation below the glass transition, however, the rigidity of the amorphous phase prevents the crystalline lamellae from rotating. As a consequence the crystals cannot rotate to an orientation where the Schmid-factor is high enough to reach or exceed the critical resolved shear stress. Thus, less crystals experience crystallographic slip, reducing the increase in dislocation density compared to the same material deformed above  $T_g$ .

This mechanism can also explain the comparatively small value in dislocation density of PET after its deformation to  $\varepsilon=0.6$  as discussed in section 6.2 (figure 6.10)

Due to inhibited dislocation kinetics below  $T_g$ , the macroscopic plastic strain has to be accommodated by alternative mechanisms, so that deformation can be accompanied e.g. by microcracking and/or shear banding. This behaviour is similar to that of poly(3-hydroxybutyrate) (P3HB) where also no significant increase in dislocation density was found because the lamellae experience fragmentation instead of crystallographic slip [18].

A decrease in the CSD-size can be seen at both deformation temperatures, above and below  $T_g$ . This reduction is caused by any deformation that leads to a misorientation of at least  $1.5^\circ$  within the crystal lattice. Considering deformation below  $T_g$ , it can be assumed that the primary deformation mechanism being active is bending of the lamellae which leads to formation of geometrically necessary misfit dislocations (section 3.2.3) [17]. This, very similar to the behaviour of  $\gamma$ -iPP during plastic deformation, results in a decrease in the domain size, simultaneously increasing the dislocation density slightly. Here, crystallographic slip seems to be negligible due to the hindered mobility of the crystalline domains.

In case of deformation above  $T_g$ , it is assumed that both deformation mechanisms, crystallographic slip and bending of the lamellae are active during the whole deformation path. A reduction in the domain size can preferably be seen up to a true strain of  $\varepsilon = 0.25$ . This can primarily be attributed to increasing crystalline misorientations caused by lamellae bending. However, also crystallographic slip processes contribute to the plastic flow, especially those slip planes with a low  $\tau_0$ . According to previous investigations this corresponds to screw dislocations moving on chain slip planes [22].

If a true strain of  $\varepsilon = 0.25$  is exceeded, deformation by crystalline misorientations becomes less important which is reflected in a more constant development of the CSD-size. In fact crystallographic slip becomes the dominant deformation mode at higher strains. The increasing stress not only increases the number of screw dislocations operating in the chain slip system being involved in the deformation process, but also leads to an activation of transverse slip systems containing dislocations with edge character [15, 22].

### 6.2.1 Evidence for dislocation presence and multiplication from the Momentum Method

The previous sections concentrated on PP since it is well suited for MXPA experiments due to its large number of high intensity Bragg reflections. As already mentioned in previous chapters, not all semicrystalline polymers possess sufficient numbers of Bragg peaks which could be used for the successful application of MXPA. An example of such a material is PE, which represents, due to its simple crystallographic structure, a model material for studying plastic deformation mechanisms. The following section shows how information about microstructural parameters can still be extracted from single PE line profiles applying a special X-ray technique, the so called momentum method [107, 108].

Multi-reflection methods are powerful tools when it comes to determine microstructural parameters in a non-destructive manner, which is indispensable during in-situ investigations. However, a necessity of multi-reflection methods including whole profile fitting approaches is, as the name indicates, the presence of several high intensity reflections. A semicrystalline polymer which does not fulfill these conditions is polyethylene. PE crystallizes in an orthorhombic crystal structure [30, 32, 134, 135] with a lamella thickness of about 20 nm, which can be increased to 160 nm by high pressure crystallization, often accompanied by an increase in crystallinity [124, 136–138].

Since the diffraction pattern of PE only shows two high intensity peaks in case of an undeformed state, multi-reflection methods including CMWP cannot be applied. However, by the use of the momentum method the same physical quantities can be determined out of a single line profile. Still, a basic requirement for the application of this evaluation method is that the background-to-peak-ratio (BGR) is not larger than  $10^{-4}$  [107].

In order to demonstrate the importance of a low BGR, Groma and Szekely [107] demonstrated the influence of different artificially added background levels on the qualitative development of the fourth order restricted moment. According to figure 6.12 it can be seen that the development of the moment changes if the background level is in the order of  $10^{-3}$ . Nevertheless, Groma and Szekely suggested that the relative intensity should be kept below a value of  $10^{-4}$  in order to obtain reliable results. However, according to figure 6.12 it can be seen that the qualitative development of the fourth order moment only changes marginally from a background level of  $10^{-3}$  to  $10^{-4}$  so that a relative intensity of at least  $10^{-3}$  can be accepted (figure 6.12).

While the requirement of a low BGR can be fulfilled rather easily in metallic materials if the peaks are well separated, (by e.g. using synchrotron radiation or increasing the measurement

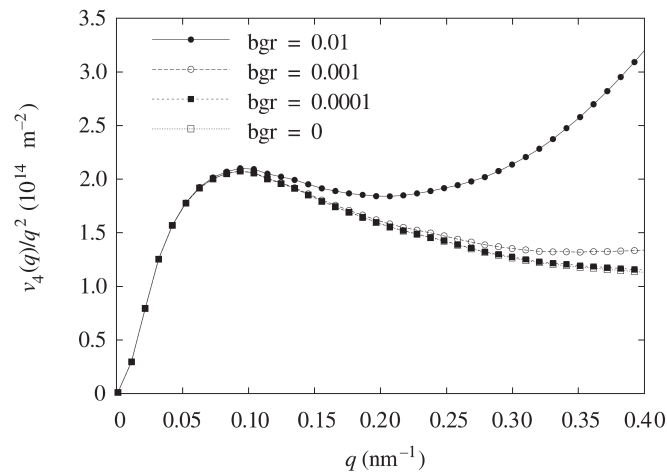


**Figure 6.12:** Effect of relative intensity on the development of the fourth order restricted moment. Exceeding a BGR of  $10^{-4}$  results in a different development of the restricted moments [107].

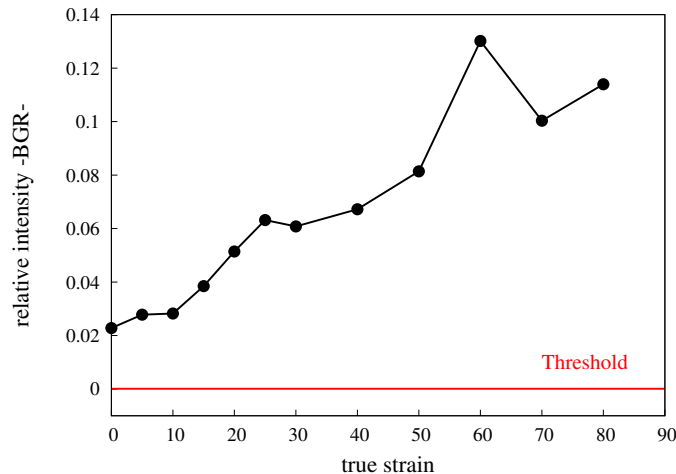


**Figure 6.13:** BGR for the (110) reflection as a function of true strain.

time), it is much more challenging in case of polymers. The limiting factor with respect to relative intensity is the presence of an amorphous phase. In standard thermoplasts such as PP or PE, crystallinity is in the range between 50 % to 70 %, thus a remaining amorphous fraction contributes to the diffraction pattern by increasing the background scattering. Increasing the measurement time is not constructive, since with proceeding time, not only the peak intensity, but also the amorphous halo increases. Figure 6.13 shows the relative intensity for the orthorhombic (110) reflection with increasing deformation. Already in the undeformed state, the BGR is about two orders of magnitudes beyond the suggested threshold which is necessary to perform a quantitative determination of dislocation densities. An increase in relative intensity is observed with proceeding deformation due to amorphization of crystalline domains, most probably caused by extensive shear band formation, therefore a quantitative determination of

dislocation densities is not possible, especially at higher deformations.

However, even if the relative intensity cannot be reached within the given experimental conditions, the following discussion shows how qualitative estimations can be made whether line broadening is dominated by local strains as a consequence of dislocation activity, and/or is due to size effects, and how this situation changes with deformation.

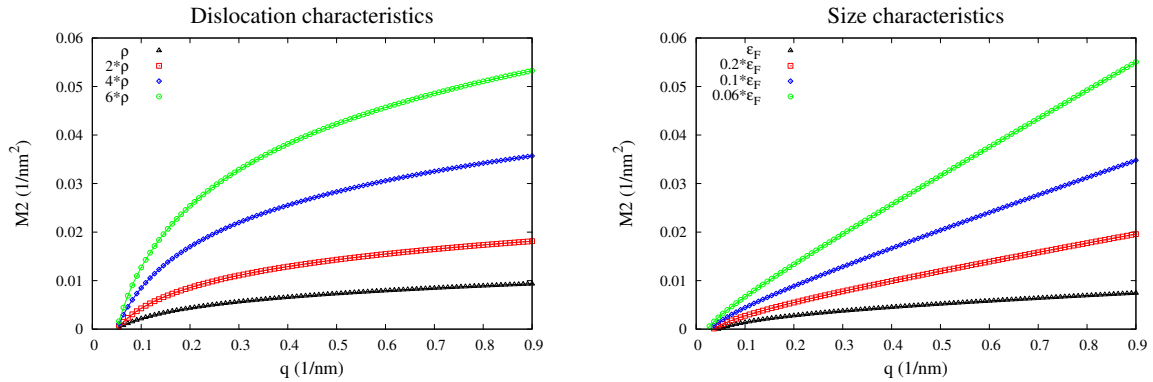
On the basis of equation 4.8 it can be seen that the first term of the second order moment which depends on the finite crystal size, is linear in  $q$ , while the presence of dislocations results in a logarithmic behaviour.

$$M_2(q) = \frac{q}{\pi^2 \varepsilon_F} - \frac{L}{4\pi^2 K^2 \varepsilon_F^2} + \frac{\Lambda \langle \rho \rangle \ln(q/q_0)}{2\pi^2} \quad (4.8)$$

The consequence of line broadening which is solely induced by a small crystal size or internal strains caused by dislocations is shown by a simulation consisting of theoretical plots of the second order moment (equation 4.8) in figure 6.14a and figure 6.14b respectively. In figure 6.14a the crystal size  $\varepsilon_F$  is kept constant, while the dislocation density  $\rho$  was gradually increased. According to equation 4.8, it is obvious that, in figure 6.14a the logarithmic character becomes increasingly pronounced with increasing dislocation density. Contrary, when the dislocation density is held constant, simultaneously decreasing the crystal size, a clear linear behaviour of the second order moment is seen in figure 6.14b. The experimentally determined curves for the second order moments are shown in figure 6.15 calculated according to equation 4.7.

Thus, by comparing the experimental curve (figure 6.15) with the theoretical curves (figure 6.14), it is evident that dislocations are not only dominant in the undeformed sample due to its logarithmic behaviour. Additionally, the increase in magnitude of  $M_2$  at higher deformations in figure 6.15 is a strong indication that an increase in dislocation density occurs with proceeding deformation.

An even better distinction between strain and size related broadening can be made by means of the fourth order restricted moment (equation 4.9), where the difference between the logarithmic and linear development is much more striking. Here, similar to the second order restricted moment, the theoretical function 4.9 was plotted by varying  $\rho$  and  $\varepsilon_F$  in figure 6.17a and 6.17b respectively, strictly repeating the procedure with the fourth order restricted moment.



(a) Plot of equation 4.8 for different dislocation densities. The limited crystal size  $\varepsilon_F$  was held constant while the dislocation density  $\rho$  was continuously increased.

(b) Plot of equation 4.8 for different crystallite sizes. The dislocation density was held constant while the crystallite size  $\varepsilon_F$  was continuously decreased.

**Figure 6.14**

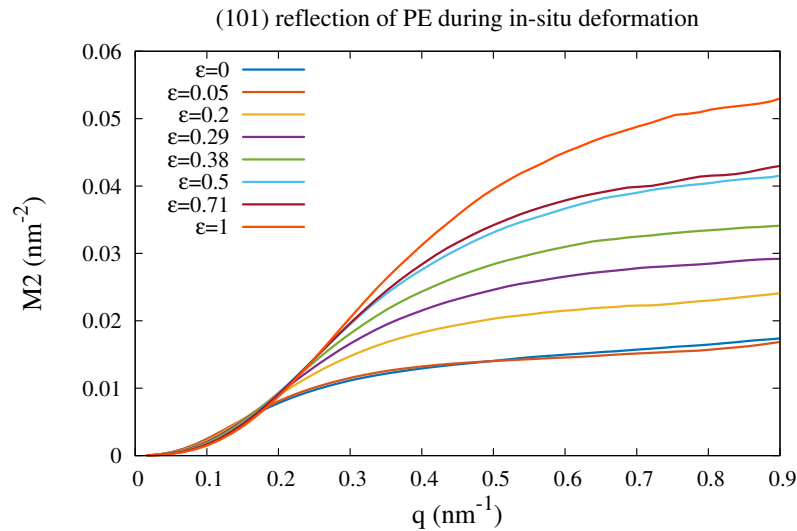


**Figure 6.15:** Development of the second order moment for different true strains.

$$\frac{M_4(q)}{q^2} = \frac{q}{3\pi^2\varepsilon_F} + \frac{\Lambda \langle \rho \rangle}{4\pi^2} + \frac{3\Lambda^2 \langle \rho^2 \rangle}{4\pi^2 q^2} \ln^2(q/q_1) \quad (4.9)$$

By comparing the experimentally determined fourth order moments from figure 6.16 with the theoretical plots in figure 6.17b, a size dominated line broadening, especially at deformations exceeding a true strain of 0.3 can definitely be excluded. Instead, by a comparison with figure 6.17a, it can be assumed that line broadening is primarily determined by local strains which originate from the presence of dislocations.

Based on the logarithmic behaviour of the second and fourth order restricted moments it

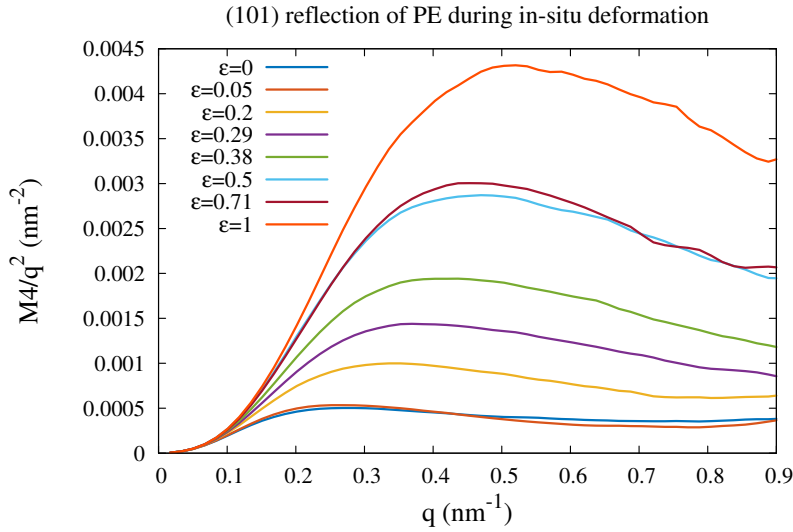
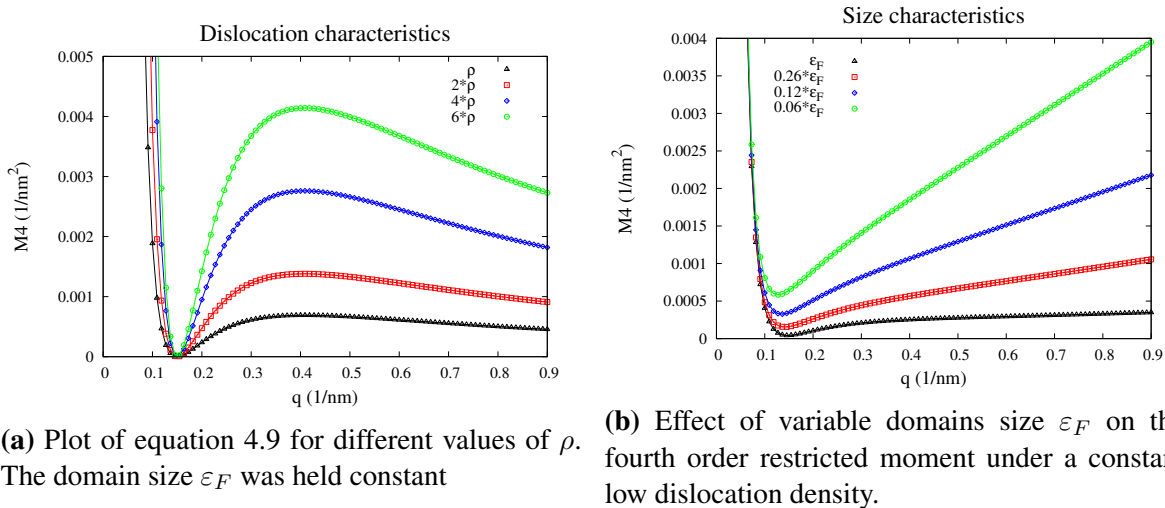


**Figure 6.16:** Development of the fourth order moment divided by  $q^2$  for different degrees of deformation. The logarithmic development points at the presence of dislocations.



**(a)** Plot of equation 4.9 for different values of  $\rho$ . The domain size  $\varepsilon_F$  was held constant

**(b)** Effect of variable domains size  $\varepsilon_F$  on the fourth order restricted moment under a constant low dislocation density.

**Figure 6.17**

can be assumed that dislocations are present at all stages of deformation. The increase in absolute values of the M2 and M4 signal indicates at a multiplication of dislocations with increasing strain. Therefore it can be expected that dislocations are involved in plastic deformation processes in PE, similarly as in the  $\alpha$ -phase of iPP. For a quantitative analysis of size and dislocation structure parameters of PE, the BGR has to be minimized by at least two orders of magnitudes. In this case, absolute values could be obtained in case of marginally deformed samples. Possible routes in achieving this goal may contain the production of highly crystalline PE samples. However, a reduction in relative intensity may be expected with increasing deformation due to decreasing crystallinity as it was observed in similar in-situ experiments (section 6.2 and 6.1). Crystallinity in PE can be increased up to 90 % by using low molecular weight

PE [139]. However, a disadvantage is its relative low strength. Alternatively, crystallinity of PE can be increased up to 99 % by crystallization under high pressure [136, 138, 140]. By applying this method not only crystallinity but also the lamellae thickness can be controlled to a certain extent by obtaining chain-extended crystals [125].



# Chapter 7

## Summary and Conclusions

This thesis aimed at the microstructural mechanisms involved in plastic deformation of three types of semicrystalline polymers (PP, PET, PE). Special attention was paid to the occurrence of dislocation based deformation mechanisms as these have significant consequences not only to the microstructure and strength characteristics of the crystalline phase but also to those of the amorphous phase via the interfaces (e.g. tie chains) acting as stress transmitters between the two phases. In order to find out just this interplay between these phases,

1. annealing experiments on samples plastically compressed beyond the temperature of glass transition,  $T_g$ , were performed. Both in-situ XRD investigations as well as “Multiple X-ray line Profile Analysis” (MXPA) measurements were done, which is a special method used for the quantification of dislocations also providing information on the coherent crystalline domain size.
2. In parallel, particularly in order to clarify more details of the mechanisms involved, DMTA investigations were done as they are sensitive to all kinds of molecular relaxations.
3. Plastic compression experiments were performed at temperatures below and beyond the glass temperature, again in parallel to in-situ XRD and MXPA measurements.

The results for  $\alpha$ -iPP comprised pronounced reductions of the initially high dislocation density at temperatures of 10°C and 85°C, which could be related to the mechanical  $\beta$ - and  $\alpha$ -relaxation, respectively, observed in the DMTA analysis. As the first reduction of the dislocation density at 10°C occurs just at the glass transition temperature  $T_g$ , it can be explained in terms of a softening of the amorphous phase, leading to a reduction in back-stresses on the crystallites thus enhancing the mobility of piled-up dislocations and thus their annealing. The reason for the marked decrease of the dislocation density at the  $\alpha$ -transition at 85°C is attributed to a general

annihilation process of dislocations. Here the whole activation energy of the process is provided thermally, in contrast to the previous reduction of dislocation density where the annihilation is assisted by the back-stresses, thus requiring less thermal energy. Considering the case of molecular chain twists as a possible defect model, a potential annihilation mechanism is that twists with a different algebraic sign cancel each other, or that they move through the crystal to the amorphous phase, both mechanisms resulting in a reduction of the dislocation density.

In-situ XRD/XPA annealing studies were also performed in PET. Here, only one but significant decrease in the dislocation density could be observed already at  $T = 25^{\circ}\text{C}$  which is markedly below the glass transition temperature. However, this result seems to be a consequence of the poor measuring power of the Williamson-Hall method as this only evaluates peak widths instead of full profile characteristics as done by the CMWP method [27, 103]. One can thus assume that the annealing characteristics in PET at the glass transition temperature occurs similarly to the case of PP. Nevertheless, it was found that PET showed a comparatively low dislocation density after its deformation to a true strain of  $\varepsilon=0.6$ . The most probable explanation to this is that the deformation temperature was well below the glass transition temperature. Here, the lamellar crystals may have less degrees of rotation due to the rigidity of the amorphous phase, thus decreasing the number of active crystalline slip systems and therefore also the number of dislocations generated.

At least such a mechanism has been found in  $\alpha$ -iPP by in-situ compression MXPA experiments with compression being performed not only beyond but also below the glass transition temperature in order to significantly increase the rigidity of the amorphous phase. Indeed, a pronounced increase in dislocation density was observed only during compression at room temperature, well above  $T_g$ . The only marginal increase in dislocation density found at compression below  $T_g$  is explained by the high rigidity of amorphous matrix at this temperature which restricts free adjustment of the crystalline lamellae allowing for easy deformation and/or dislocation generation. Changes in CSD size were found to be different for deformation beyond and below  $T_g$ , but much less significant than the differences in dislocation density evolution.

Last but not least, also PE was subject of investigations in this thesis. In order to perform investigations being analogous to those described above - in spite of the low number of Bragg reflections in this material - the so-called "momentum method" was applied, for the first time for a semicrystalline polymer. In principle this method allows to obtain the same physical parameters out of a single line profile, as MXPA does with at least four line profiles, provided that the relative background does not exceed a value of  $10^{-4}$  [107]. Although the latter condition could not be fulfilled due to the multiphase nature of a semicrystalline polymer, a qualitative discussion on the involved deformation mechanisms was still possible by comparing measured

second and fourth order restricted moments with theoretically calculated ones. At least for the case of PE, it was demonstrated that the logarithmic behaviour of the second and fourth order restricted moments not only indicates the presence of dislocations, but also their multiplication with increasing strain. At least it could be shown that exclusively applying the momentum XPA method in PE proved the operation of dislocation-based deformation mechanisms herein.

### **Resume**

The present thesis showed that in case of dislocation-mediated deformation mechanisms in semicrystalline polymers, the amorphous phase can play a substantial role with respect to dislocation dynamics. By increasing the mechanical rigidity of the amorphous phase, a change of plastic deformation mechanisms occurs, passing from a dislocation-mediated crystallographic slip to a mechanism operating by shear band production and/or microcracking. The rigidity of the amorphous phase strongly affects the free rotation of the crystalline lamellae, which can result in an extensive generation or in an impediment of dislocation generation not only in PP, but also in other semicrystalline polymers like PET and probably PE where dislocation-mediated deformation mechanisms are active. The rigidity of the amorphous phase can be systematically changed by selective annealing experiments at increasing temperatures thus launching increasing molecular relaxations. Therefore, it can be understood that dislocations increasingly annihilate with increasing annealing temperature especially when the annihilation is assisted by back stresses in the wake of the interface between the amorphous and crystalline phase.

### **Perspectives of the Thesis**

Future investigations may include DMTA experiments of the  $\gamma$ -phase of PP. Plastic deformation in  $\gamma$ -iPP is dominated by interlamellar shear including shear band formation, and not by dislocations [17, 48]. Hence, the  $\alpha$ -relaxation observed in the mechanical loss spectra should be considerably smaller in  $\gamma$ -iPP compared to  $\alpha$ -iPP. Further, it should be investigated whether the subpeaks of the  $\alpha$ -relaxation can be related to specific dislocation types, e.g. screw and/or edge dislocations which should have different activation energies due to their different line energies, and which may vary in their fractions during varying plastic deformation [22]. By controlled annealing of deformation induced dislocations or generation of dislocations at different temperatures, the dislocation density, hence the crystallographic order and subsequently also the physical properties may be controlled systematically. This may have some impact to mechanical applications since the strength can be controlled by the number of mobile dislocations being present in the material [16]. Moreover, on a longer term the control of dislocation generation and mobilization may also be of significance for electronic applications in conductive/conjugated semicrystalline polymers.



# Chapter 8

## Additional works

### 8.1 Influence of molecular weight on the $\gamma$ -phase formation in PP

The  $\gamma$ -phase of isotactic polypropylene is characterized by an unusual arrangement of the macromolecular chains. Instead of being arranged in a parallel manner, like it is the case in many other semicrystalline polymers, but also in the  $\alpha$ -phase of the same material for example, the chains are tilted by about  $80^\circ$  against each other. This particular chain packing leads to increased critical resolved shear stresses, thus, impeding the lamellar crystals to deform by the preferred crystallographic slip mechanisms, instead alternative mechanisms become active (section 3.2). As a consequence, the necessary stress to initiate plastic deformation is increased, resulting in a higher strength of the material by up to 60 % [17, 19, 48].

For this reason, understanding and finding parameters which influence or even facilitate the crystallization of  $\gamma$ -iPP is of high interest. In this chapter it was investigated in how far the molecular weight of the material under variation of crystallization temperature, time and pressure has an impact on the  $\gamma$ -phase crystallization. In 1961, Addink et al. discovered an additional Bragg-reflection in X-ray powder patterns of low molecular weight PP [38, 141], which could later be identified as an additional phase of PP, the  $\gamma$ -phase. Since its discovery  $\gamma$ -iPP has attracted much attention, not only from scientific, but also from technological point of view, because its exceptional chain packing prohibits any dislocation activity being present during plastic deformation, resulting in a pronounced increase in yield stress of about 60 % compared to the  $\alpha$ -phase of the same material [17]. Common methods in obtaining large volume fractions of  $\gamma$ -phase include high pressure crystallization ( $p > 200$  MPa) [50, 142, 143], the use of metallocene catalysts [144], very low molecular weight samples [44] or high molecular weight samples with a controlled number of stereodefects [145].

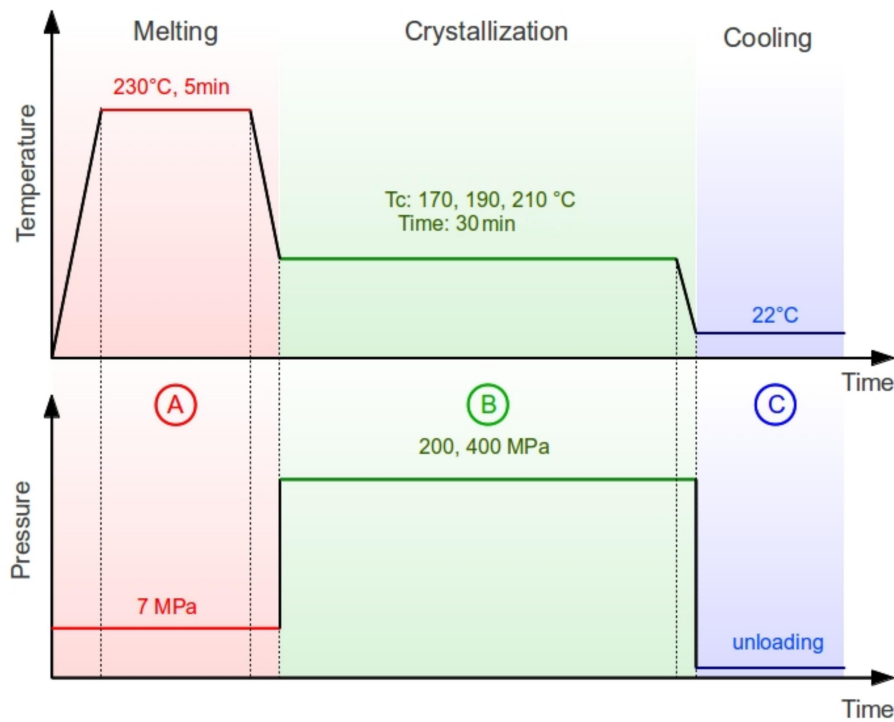
Since the influence of molecular weight ( $M_w$ ) on the formation of  $\gamma$ -iPP was investigated, three types of  $\alpha$ -iPP obtained from “Borealis AG” (Austria) with different  $M_w$  were used: (a) DM55Pharm with a  $M_w = 540$  kg/mol and a melt flow rate (MFR) of 2.8 g/10min at 230 °C/2.16 kg (b) HD120MO with  $M_w = 350$  kg/mol and MFR = 8 g/10min and (c) HF700SA with  $M_w = 240$  kg/mol with MFR = 21 g/10min at 230 °C/2,16 kg. For simplicity, these materials will be called DM, HD and HF respectively in the following. The  $\gamma$ -iPP samples were crystallized in a custom built pressure cell, described in section 4.1, while the necessary pressure of 200MPa was achieved by a “Shimadzu” ultimate testing machine.

Figure 8.1 shows the applied temperature and pressure program: (A) A pressure of 7 MPa was applied which ensured on the one hand that eventual air inclusion escape upon melting and on the other hand that a good thermal conductivity is established. This was followed by increasing the temperature to 230°C for 5 min, well above the melting point of 165 °C peak temperature obtained by DSC measurements. (B) Temperature was reduced to one of the three crystallization temperatures of 170 °C, 190 °C and 210 °C, subsequently increasing the pressure to 200 MPa. All samples were crystallized for 30 min. (C) Finally, the temperature was reduced to room temperature and the compression chamber was unloaded. The achieved cooling rate by ventilators was about 5 °C/min, however, when approaching crystallization temperature, the rate slightly decreased.

The temperature program is plotted over the theoretical phase diagram as calculated by Mezghani and Phillips [146] (figure 8.2), which shows that crystallization is carried out in the  $\gamma$ -domain for all crystallization temperatures.

Phase analysis was performed by WAXS measurements on a “GADDS D8” diffractometer using  $\text{CuK}_\alpha$  radiation and a nickel filter, operating at 50 kV and 50 mA. The spot size of the sample was 0.8 mm while measuring in reflection. A key step during phase analysis is to be aware that the phases can be distributed inhomogeneously within the sample. This means, if a diffraction pattern is recorded on a single spot on the sample surface, a higher  $\gamma$ -phase content can be obtained compared to measuring the same sample in a transmission setup. However, measuring in transmission, especially at large sample diameters, requires high energies such as synchrotron radiation which is not always applicable. Hence, for a reliable determination of the phase fractions, an oscillation alongside the whole sample height was performed during simultaneous X-ray diffraction, which allowed to investigate a larger sample volume.

Figure 8.3 shows the diffraction patterns for the three tested PP types. The positions of the Bragg-reflections in the  $\alpha$  and  $\gamma$ -phase are very close to each other, except the (130)  $\alpha$ -, and the (117)  $\gamma$ -reflection, are well separated. In order to determine the amount of  $\alpha$  and  $\gamma$ -phase quantitatively, the diffraction patterns were separated by modelling its individual phases and



**Figure 8.1:** Applied temperature program for the production of  $\gamma$ -iPP samples.

the background. All peaks were modelled using PearsonVII functions while the background was modelled by a polynomial fifth order. Figure 8.4 shows the reflections being involved in a PP diffraction pattern, a sample with almost equal amounts of  $\alpha$  and  $\gamma$ -phase was chosen. The  $\gamma$ -fraction  $K_\gamma$  was determined using the well known equation:

$$K_\gamma = \frac{I(117)_\gamma}{I(117)_\gamma + I(130)_\alpha}$$

where  $I(117)_\gamma$  and  $I(130)_\alpha$  are the integral intensities of the corresponding reflections. Hence the remaining  $\alpha$ -fraction is obtained by  $K_\alpha = 1 - K_\gamma$ .

The resulting  $\gamma$ -phase content for the investigated materials is shown in figure 8.5. The accuracy of the diffraction measurements should be relatively high, however, taking into account possible systematic errors during phase modelling, due to sample inhomogeneities or from the background subtraction an error of 5% may be assumed. This would correspond to the point size in figure 8.5. As expected, the initial amount of  $\gamma$ -phase in the as received material is marginally, and does not exceed 20%. The highest  $\gamma$ -phase content was obtained at a crystallization temperature of  $T_c=190$  °C, where almost pure  $\gamma$ -modified material could be achieved for all PP-types. Only at a molecular weight of  $M_w = 540$  kg/mol a smaller amount of  $\gamma$ -phase was obtained for temperatures of 210 °C and 170 °C. The lower  $\gamma$ -fraction at higher  $M_w$ 's in general can be explained by the increasing length of macromolecules which complicate the ar-

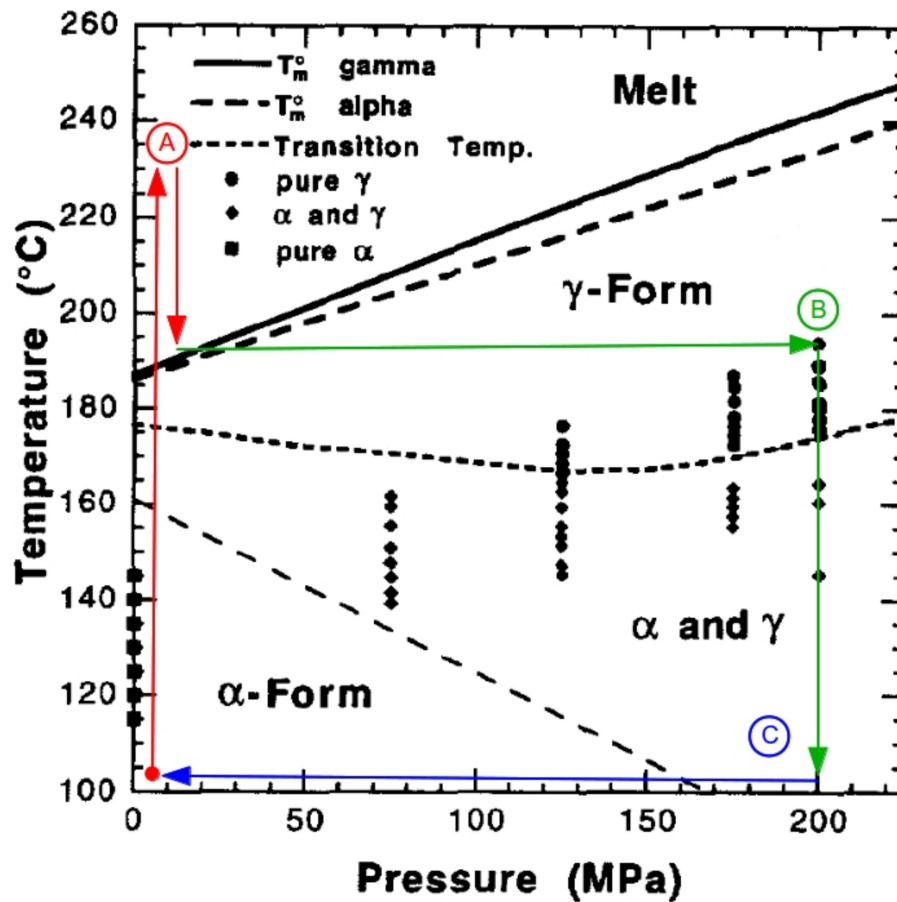


**Figure 8.2:** Theoretical phase diagram for PP for temperature as a function of pressure [146]. The points A,B and C represent the crystallization procedure.

rangement of chains to its non-parallel structure. Especially in case of the lower temperature experiment, chain diffusion is limited, so that a rearrangement to the orthorhombic crystal structure is hindered.

Crystallinity ( $X_c$ ) obtained from WAXS data did not differ significantly in case of high pressure crystallized samples, with  $X_c$  being in the range of 55 to 65 % (figure 8.6). However,  $X_c$  was higher in the as received materials, decreasing after high pressure crystallization. The decrease in  $X_c$  may result from the shorter crystallization time of 30 min compared to 60 min for the sample crystallized under atmospheric pressure. A summary of all parameters is given in table 8.1.

PP with medium molecular weight of the type HD120MO turned out to be the most suitable PP-type for crystallizing in the  $\gamma$ -modification, since a high  $\gamma$ -fraction was obtained almost independent of crystallization temperature. Hence, HD-PP was additionally crystallized at 400 MPa for 30 min at  $T_c=190^\circ\text{C}$  to investigate if an additional phase can be observed at pressures clearly exceeding 200 MPa. While only 51 % of  $\gamma$ -fraction were obtained at a pressure of 100

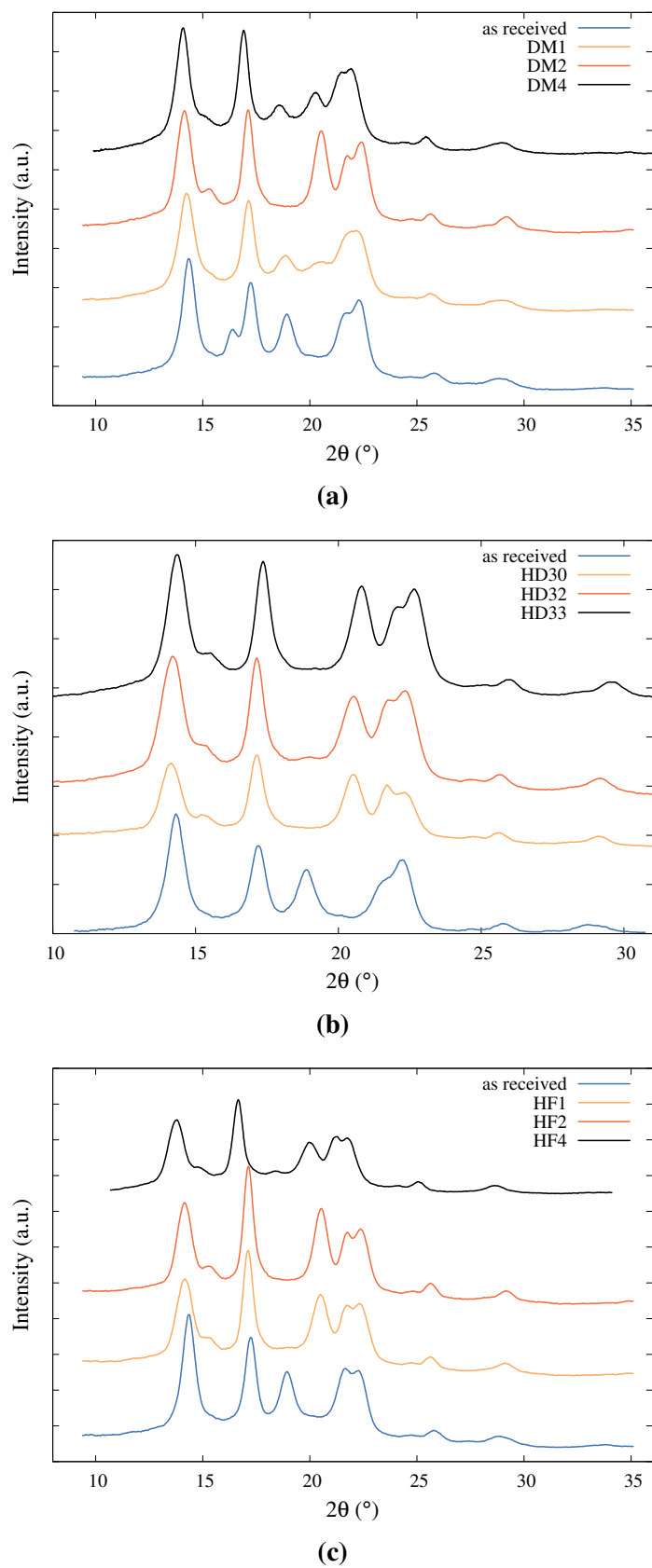


**Figure 8.3:** Diffraction patterns of high pressure crystallized PP samples with different molecular weight for (a) DM55Pharm, (b) HD120MO and (c) HF700SA.

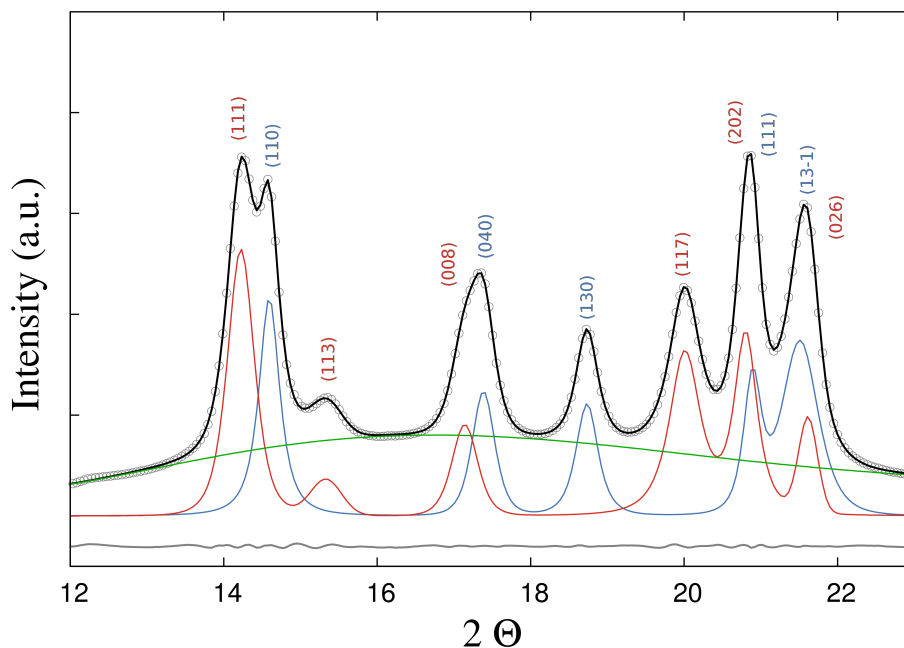


**Figure 8.4:** WAXS pattern of iPP with similar amounts of  $\alpha$  and  $\gamma$ -phase. Measured data ( $\circ$ ), fit (full line),  $\alpha$ -phase (blue line),  $\gamma$ -phase (red line), background (green line), residuals (gray line).

MPa, crystallization exclusively resulted in the  $\gamma$ -form at 200 MPa and above (figure 8.7 and 8.8). However, no additional phases could be observed crystallizing at a pressure of 400 MPa. Crystallinity as determined from WAXS depicts a slight decrease reaching 200 MPa and stays then relatively constant.

### Summary

PP with three different molecular weights were tested in their capability to crystallize in the  $\gamma$ -form with respect to different crystallization temperatures. PP of the type HD120MO with a medium Mw of 350 kg/mol turned out to be most suitable, since pure  $\gamma$ -iPP was obtained for all crystallization temperatures. However, applying a crystallization temperature of 190 °C resulted in high amounts of  $\gamma$ -fraction, not only for PP with medium Mw, but also for the low and high Mw-type, Mw = 240 kg/mol and Mw = 540kg/mol respectively. Apparently, the higher molecular weight hinders the rearrangement of macromolecules so that high amounts of  $\gamma$ -phase cannot be achieved for all crystallization temperatures. Interestingly, pure  $\gamma$ -iPP was obtained when crystallizing high Mw PP at  $T_c=190$  °C while the  $\gamma$ -fraction was lowered at a  $T_c$  of 170 °C and 210 °C. In case of  $T_c=170$  °C, chain diffusion may not be high enough at this temperature, however a similarly low amount of  $\gamma$ -phase was obtained at a higher temperature of  $T_c=210$  °C. Here, possibly the crystallization temperature is close to the melting temperature, so that the smaller amount of  $\gamma$ -phase just formed during cooling to room temperature.

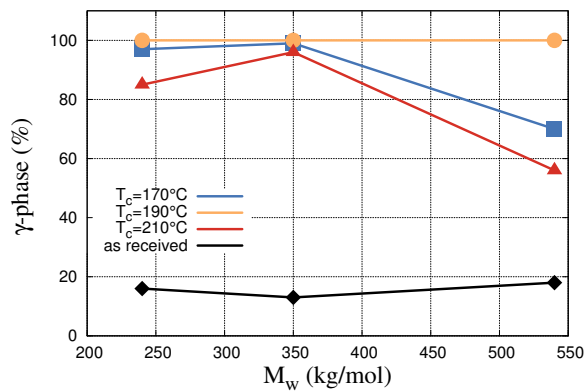


**Figure 8.5:** The highest  $\gamma$ -phase content was obtained for the material with medium Mw for all tested crystallization temperatures

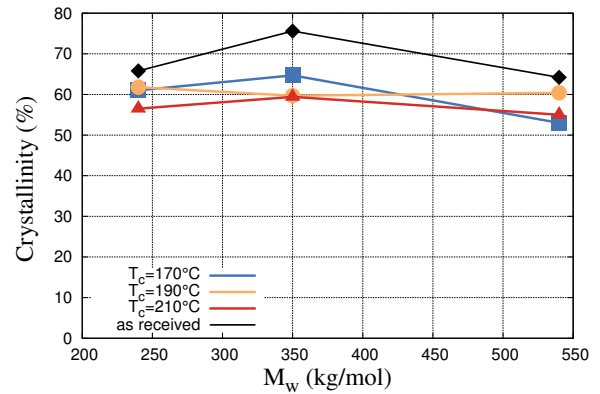


**Figure 8.6:** Obtained crystalline volume fractions  $X_c$  for the different types of PP. Except for the low Mw material,  $X_c$  decreased during high pressure crystallization.

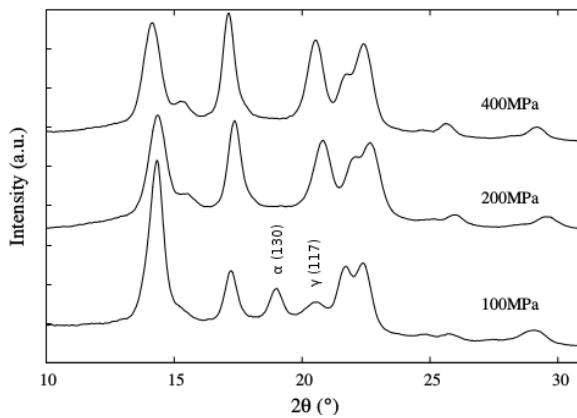


**Figure 8.7:** Additional phase formation could not be observed at a pressure of 400 MPa.

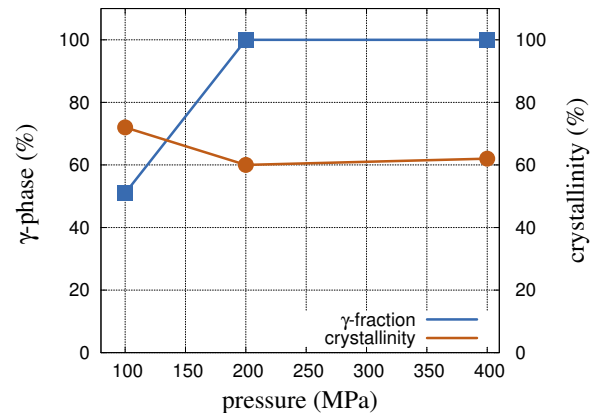


**Figure 8.8:**  $\gamma$ -phase content as a function of applied pressure during crystallization. Crystallization of PP (HD120MO) at 200 MPa and above, results in samples with pure  $\gamma$ -phase modification.

**Table 8.1:**  $\gamma$ -fraction and crystallinity obtained by different processing conditions at 200 MPa

sample	Mw(kg/mol)	Tc (°C)	Xc - X-ray (%)	$\gamma$ -fraction (%)
hf1	240	170	61	97
hf2	240	190	61.8	100
hf4	240	210	67	85
hd30	350	170	64.7	99
hd33	350	190	59.7	100
hd32	350	210	59.4	96
dm4	540	170	53	70
dm2	540	190	60.4	100
dm1	540	210	55	56



## 8.2 Derivation of the Gibbs-Thomson equation for semi-crystalline polymers

The Gibbs-Thomson equation [97, 147] is often used to determine the lamellar thickness  $\lambda$  by measuring the melting temperature of the material (which depends on the lamella thickness), provided that the surface energy  $\sigma_e$ , the enthalpy of melting for the crystalline phase  $\Delta h_f$  and the equilibrium melting temperature  $T_m^0$  are known. For infinite large lamellar crystals, the melting temperature  $T_m$  approaches the equilibrium melting temperature  $T_m^0$ . In case of semicrystalline polymers, the Gibbs-Thomson equation can be derived by fundamental thermodynamic concepts:

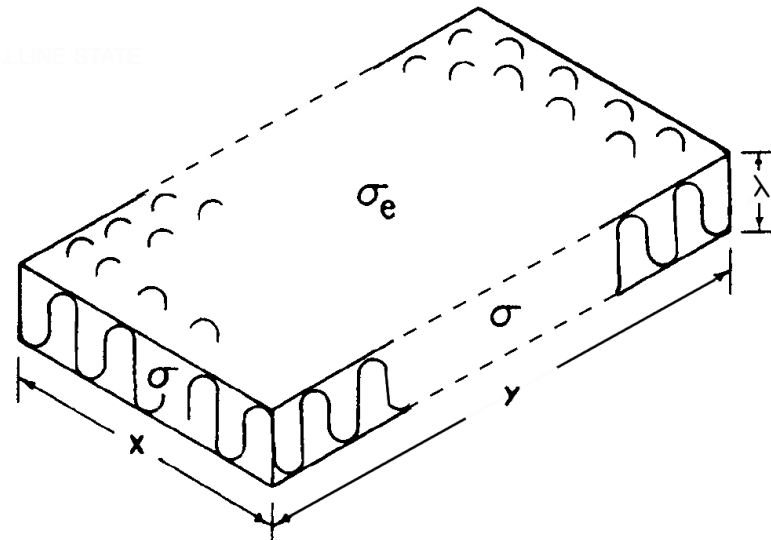


**Figure 8.9:** Schematic drawing of a lamellar crystal

$$\Delta G(t) = 2xy \cdot \sigma_e + (2\lambda x + 2\lambda y) \cdot \sigma - xy\lambda \cdot \Delta G_f \quad (8.1)$$

At the melting point  $T_m$  we have

$$\Delta G(T_m) = 0 \quad (8.2)$$

In case of large lateral dimensions it can be assumed that:

1)

$$x \cong y \text{ and}$$

2)

$$xy \gg (\lambda x + \lambda y)$$

Additionally it can be assumed that

$$\sigma_e \gg \sigma \quad (8.3)$$

Thus

$$\Delta G(T_m) = 2x^2 \cdot \sigma_e - \lambda x^2 \cdot \Delta G_f$$

Combining 8.2 and 8.3 we receive

$$\Delta G(T_m) = 2x^2 \cdot \sigma_e - \lambda x^2 \cdot \Delta G_f(T_m) = 0$$

$$\Delta G_f(T_m) = \frac{2x^2 \cdot \sigma_e}{\lambda x^2} = \frac{1}{\lambda} 2\sigma_e \quad (8.4)$$

in case of an infinite large crystal at  $T_m^0$  we obtain

$$\Delta G_f(T_m^0) = \Delta h_f(T_m^0) - T_m^0 \cdot \Delta S_f(T_m^0) = 0$$

$$\Delta S_f(T_m^0) = \frac{\Delta h_f(T_m^0)}{T_m^0} \quad (8.5)$$

In case of high melting temperatures  $\Delta h_f(T_m) = \Delta h_f(T_m^0)$  and  $\Delta S_f(T_m) = \Delta S_f(T_m^0)$ , thus

$$\Delta G_f(T_m) = \Delta h_f(T_m^0) - T_m \cdot \Delta S_f(T_m^0) = \Delta h_f(T_m^0) - T_m \frac{\Delta h_f(T_m^0)}{T_m^0} = \Delta h_f(T_m^0) \left(1 - \frac{T_m}{T_m^0}\right)$$

Using equation 8.4 one obtains

$$\frac{2}{\lambda} \sigma_e = \Delta h_f(T_m^0) \left(1 - \frac{T_m}{T_m^0}\right)$$

$$\frac{2\sigma_e}{\Delta h_f(T_m^0) \cdot \lambda} = 1 - \frac{T_m}{T_m^0}$$

$$\left(1 - \frac{2\sigma_e}{\Delta h_f(T_m^0) \cdot \lambda}\right) T_m^0 = T_m \quad (8.6)$$





## References

- [1] G. Menges. *Werkstoffkunde Kunststoffe*. Studentexte Kunststofftechnik. Hanser, 2002.
- [2] Patricia M. Wilson and David C. Martin. Quantitative measurements of polymer chain-end edge dislocation strain fields by high resolution electron microscopy. *Macromolecules*, 29(3):842–851, January 1996.
- [3] W.J. O’Kane and R.J. Young. The role of dislocations in the yield of polypropylene. *Journal of Materials Science Letters*, 14(6):433–435, 1995.
- [4] L. Lin and A. S. Argon. Rate mechanism of plasticity in the crystalline component of semicrystalline nylon 6. *Macromolecules*, 27:6903 – 6914, 1994.
- [5] O. Darras and R. Séguéla. Tensile yield of polyethylene in relation to crystal thickness. *Journal of Polymer Science: Part B: Polymer Physics*, 31:759–766, 1993.
- [6] Buckley Crist, Christopher J. Fisher, and Paul R. Howard. Mechanical properties of model polyethylenes: tensile elastic modulus and yield stress. *Macromolecules*, 22:1709–1718, 1989.
- [7] W. Wilke. Dislocations and paracrystallinity in polymers. *Colloid & Polymer Science*, V261(8):656–660, August 1983. 252.1974 - Sign.: 04051.002 Sign.: Tiefspeicher.
- [8] D.H. Reneker and J. Mazur. Dislocations, disclinations, dislocations, and chain twist in polyethylene crystals. *Polymer*, 24(11):1387 – 1400, 1983.
- [9] L. G. Shadrake and F. Guiu. Dislocations in polyethylene crystals: line energies and deformation modes. *Philos. Mag.*, 34(4):565–581, 1976.
- [10] R. J. Young. A dislocation model for yield in polyethylene. *Philosophical Magazine*, 30(1):85–94, 1974.
- [11] H. Gleiter and A. S. Argon. Plastic deformation of polyethylene crystals. *Philosophical Magazine*, 24(187):71–80, 1971.

- [12] J.M. Peterson. Peierls stress for screw dislocations in polyethylene. *J. Appl. Phys.*, 39:4920–4928, 1968.
- [13] James M. Peterson. Thermal initiation of screw dislocations in polymer crystal platelets. *Journal of Applied Physics*, 37(11):4047–4050, 1966.
- [14] Mohammad Zare Ghomsheh, Florian Spieckermann, Gerald Polt, Harald Wilhelm, and Michael Zehetbauer. Analysis of strain bursts during nanoindentation creep of high-density polyethylene. *Polymer International*, 64(11):1537–1543, 2015.
- [15] G. Polt, F. Spieckermann, H. Wilhelm, Ch. Fischer, E. Schafner, S. Bernstorff, and M. Zehetbauer. Crystalline plasticity in isotactic polypropylene below and above the glass transition temperature. *eXPRESS Polymer Letters*, 9:894–900, 2015.
- [16] Florian Spieckermann, Harald Wilhelm, Gerald Polt, Saïd Ahzi, and Michael Zehetbauer. Rate mechanism and dislocation generation in high density polyethylene and other semicrystalline polymers. *Polymer*, 55(5):1217 – 1222, 2014.
- [17] G. Polt, F. Spieckermann, H. Wilhelm, M.B. Kerber, E. Schafner, S. Bernstorff, and M. Zehetbauer. The role of dislocations in  $\gamma$ -ipp under plastic deformation investigated by x-ray line profile analysis. *Mechanics of Materials*, 67(0):126 – 132, 2013. Nanos-structured Materials.
- [18] Florian Spieckermann, Gerald Polt, Harald Wilhelm, Michael Kerber, Erhard Schafner, and Michael J. Zehetbauer. The role of dislocations for the plastic deformation of semicrystalline polymers as investigated by multireflection X-ray line profile analysis. *J. Appl. Polym. Sci.*, 125(6):4150–4154, 2012.
- [19] Gerald Polt. Mechanisms of plastic deformation in  $\gamma$ -isotactic polypropylene. Master’s thesis, Universtiy of Vienna, 2011.
- [20] F. Spieckermann, H. Wilhelm, E. Schafner, M. Kerber, S. Bernstorff, and M.J. Zehetbauer. Plasticity and x-ray line profile analysis of the semicrystalline polymer poly(3-hydroxybutyrate). *Journal of Physics: Conference Series*, 240(1):012146, 2010.
- [21] Florian Spieckermann, Harald Wilhelm, Michael Kerber, Erhard Schafner, Gerald Polt, Sigrid Bernstorff, Frédéric Addiego, and Michael Zehetbauer. Determination of lamella thickness distributions in isotactic polypropylene by X-ray line profile analysis. *Polymer*, 51(18):4195–4199, August 2010.

- [22] Florian Spieckermann. *Investigation of Deformation Induced Changes of the Microstructure of Semicrystalline Polymers and their Impact on Mechanical Properties*. PhD thesis, University of Vienna, 2010.
- [23] H. Wilhelm, A. Paris, E. Schafner, S. Bernstorff, J. Bonarski, T. Ungar, and M.J. Zehetbauer. Evidence of dislocations in melt-crystallised and plastically deformed polypropylene. *Mater. Sci. Eng., A*, 387-389:1018–1022, 2004.
- [24] T. Ungar. Microstructural parameters from x-ray diffraction peak broadening. *Scr. Mater.*, 51(8 SPEC. ISS.):777–781, 2004.
- [25] T. Ungár, I. Dragomir, Á. Révész, and A. Borbély. The contrast factors of dislocations in cubic crystals: the dislocation model of strain anisotropy in practice. *Journal of Applied Crystallography*, 32(5):992–1002, Oct 1999.
- [26] T. Ungár, J. Gubicza, G. Ribárik, and A. Borbély. Crystallite size distribution and dislocation structure determined by diffraction profile analysis: principles and practical application to cubic and hexagonal crystals. *J. Appl. Crystallogr.*, 34(3):298–310, Jun 2001.
- [27] T. Ungár and A. Borbély. The effect of dislocation contrast on x-ray line broadening: A new approach to line profile analysis. *Appl. Phys. Lett.*, 69(21):3173–3175, 1996.
- [28] T. Ungar. The meaning of size obtained from broadened x-ray diffraction peaks. *Advanced Engineering Materials*, 5(5):323–329, 2003.
- [29] T. Ungár. Characterization of nanocrystalline materials by x-ray line profile analysis. *Journal of Materials Science*, 42(5):1584–1593, 2007. cited By (since 1996) 24.
- [30] D. C. Bassett and A. M. Hodge. On the morphology of melt-crystallized polyethylene i. lamellar profiles. *Proceedings of the Royal Society of London. Series A, Mathematical and Physical Sciences (1934-1990)*, 377(1768):25–37, June 1981.
- [31] D.C. Bassett and R.H. Olley. On the lamellar morphology of isotactic polypropylene spherulites. *Polymer*, 25(7):935 – 943, 1984.
- [32] L. Lin and A. S. Argon. Structure and plastic deformation of polyethylene. *J. Mater. Sci.*, 29(2):294–323, January 1994.
- [33] A. Keller. A note on single crystals in polymers: Evidence for a folded chain configuration. *Philosophical Magazine*, 2(21):1171–1175, 1957.

- [34] [http://www.spring8.or.jp/en/news\\_publications/publications/scientific\\_results/soft\\_matter/topic7](http://www.spring8.or.jp/en/news_publications/publications/scientific_results/soft_matter/topic7), Revision as of Jun 20 17:11:30 CEST 2015.
- [35] <http://www.cemef.mines-paristech.fr/sections/recherche/equipes-recherche/structures-proprietes/structures-proprietes>, Revision as of Apr 11 22:34 CEST 2016.
- [36] P. H Geil. Polymer single crystals. *Interscience, New York*,, page 214, 1963.
- [37] F. J. Padden and H. D. Keith. Crystallization in thin films of isotactic polypropylene. *Journal of Applied Physics*, 37(11):4013–4020, 1966.
- [38] B. Lotz, J. C. Wittmann, and A. J. Lovinger. Structure and morphology of poly(propylenes): a molecular analysis. *Polymer*, 37(22):4979–4992, October 1996.
- [39] J Varga. Crystallization, melting and supermolecular structure of isotactic polypropylene. *Polypropylene: structure, blends and composites*, 1:56–115, 1994.
- [40] József Varga.  $\beta$ -modification of isotactic polypropylene: Preparation, structure, processing, properties, and application. *Journal of Macromolecular Science, Part B*, 41(4-6):1121–1171, 2002.
- [41] Ayret Mollova, René Androsch, Daniela Mileva, Markus Gahleitner, and Sergio S. Furnari. Crystallization of isotactic polypropylene containing beta-phase nucleating agent at rapid cooling. *European Polymer Journal*, 49(5):1057 – 1065, 2013.
- [42] B Lotz.  $\alpha$  and  $\beta$  phases of isotactic polypropylene: a case of growth kinetics ‘phase reentrecy’ in polymer crystallization. *Polymer*, 39(19):4561 – 4567, 1998.
- [43] Dima Libster, Abraham Aserin, and Nissim Garti. Advanced nucleating agents for polypropylene. *Polymers for Advanced Technologies*, 18(9):685–695, 2007.
- [44] B. Lotz, S. Graff, C. Straupé, and J.C. Wittmann. Single crystals of  $\gamma$ -phase isotactic polypropylene: combined diffraction and morphological support for a structure with non-parallel chains. *Polymer*, 32(16):2902 – 2910, 1991.
- [45] Ralf Thomann, Chun Wang, Jorg Kressler, and Rolf Mulhaupt. On the  $\gamma$ -phase of isotactic polypropylene. *Macromolecules*, 29(26):8425–8434, 1996.
- [46] A Turner-Jones. Development of the  $\gamma$ -crystal form in random copolymers of propylene and their analysis by dsc and X-ray methods. *Polymer*, 12(8):487–508, August 1971.

- [47] E. Lezak and Z. Bartczak. Plastic deformation of the  $\gamma$ -phase isotactic polypropylene in plane-strain compression at elevated temperatures. *Macromolecules*, 40(14):4933–4941, July 2007.
- [48] E. Lezak, Z. Bartczak, and A. Galeski. Plastic deformation of the  $\gamma$  phase in isotactic polypropylene in plane-strain compression. *Macromolecules*, 39(14):4811–4819, July 2006.
- [49] Przemyslaw Sowinski, Ewa Piorkowska, Severine A.E. Boyer, Jean-Marc Haudin, and Kinga Zapala. The role of nucleating agents in high-pressure-induced gamma crystallization in isotactic polypropylene. *Colloid and Polymer Science*, 293(3):665–675, 2015.
- [50] K. Mezghani and P. J. Phillips. The  $[\gamma]$ -phase of high molecular weight isotactic polypropylene. ii: The morphology of the  $[\gamma]$ -form crystallized at 200 mpa. *Polymer*, 38(23):5725–5733, November 1997.
- [51] Sergio Brückner, Stefano V. Meille, Vittorio Petraccone, and Beniamino Pirozzi. Polymorphism in isotactic polypropylene. *Progress in Polymer Science*, 16(2–3):361 – 404, 1991.
- [52] R. Hiss, S. Hobeika, C. Lynn, and G. Strobl. Network stretching, slip processes and fragmentation of crystallites during uniaxial drawing of polyethylene and related copolymers. *Macromolecules*, 32:4390–4403, 1999.
- [53] Z. Bartczak and A. Galeski. Plasticity of semicrystalline polymers. *Macromolecular Symposia*, 294(1):67–90, 2010.
- [54] Z. Bartczak. Influence of molecular parameters on high-strain deformation of polyethylene in the plane-strain compression. part ii. strain recovery. *Polymer*, 46:10339–10354, 2005.
- [55] A. Galeski, A. S. Argon, and Robert E. Cohen. Changes in the morphology of bulk spherulitic nylon 6 due to plastic deformation. *Macromolecules*, 21(9):2761–2770, September 1988.
- [56] Andrew Phillips, Peng-wei Zhu, and Graham Edward. Simple shear deformation of polypropylene via the equal channel angular extrusion process. *Macromolecules*, 39(17):5796–5803, 2006.
- [57] D. P. Pope and A. Keller. Deformation of oriented polyethylene. *Journal of Polymer Science: Polymer Physics Edition*, 13(3):533–566, 1975.

- [58] E. F. Oleinik. Plasticity of semicrystalline flexible-chain polymers at the microscopic and mesoscopic levels. *Polymer science. Series C*, 45:17–117, 2003.
- [59] C. A. Garber and E. S. Clark. Morphology and deformation behavior of “row-nucleated” polyoxymethylene film. *Journal of Macromolecular Science, Part B*, 4(3):499–517, 1970.
- [60] A. S. Argon. *The Physics of Deformation and Fracture of Polymers*. Cambridge University Press, 2013. Cambridge Books Online.
- [61] T. Kazmierczak, A. Galeski, and A.S. Argon. Plastic deformation of polyethylene crystals as a function of crystal thickness and compression rate. *Polymer*, 46(21):8926–8936, October 2005.
- [62] A.S. Argon, A. Galeski, and T. Kazmierczak. Rate mechanisms of plasticity in semicrystalline polyethylene. *Polymer*, 46(25):11798–11805, November 2005.
- [63] S. Nikolov and D. Raabe. Yielding of polyethylene through propagation of chain twist defects: Temperature, stem length and strain-rate dependence. *Polymer*, 47(5):1696–1703, February 2006.
- [64] A. Peterlin. Molecular model of drawing polyethylene and polypropylene. *Journal of Materials Science*, 6(6):490–508, June 1971.
- [65] A. Galeski, Z. Bartczak, A. S. Argon, and R. E. Cohen. Morphological alterations during texture-producing plastic plane strain compression of high-density polyethylene. *Macromolecules*, 25(21):5705–5718, October 1992.
- [66] P. J. Flory and D. Y. Yoon. Molecular morphology in semicrystalline polymers. *Nature*, 272(5650):226–229, March 1978.
- [67] R. Séguéla. Plasticity of semi-crystalline polymers : crystal slip versus melting-recrystallization. *e-polymers*, 7:382–401, 2007.
- [68] A. Galeski. Strength and toughness of crystalline polymer systems. *Prog. Polym. Sci.*, 28(12):1643–1699, December 2003.
- [69] R. V. Mises. Mechanik der plastischen formänderung von kristallen. *ZAMM - Zeitschrift für Angewandte Mathematik und Mechanik*, 8(3):161–185, 1928.
- [70] H. D. Keith and W. Y. Chen. On the origins of giant screw dislocations in polymer lamellae. *Polymer*, 43(23):6263–6272, 2002.

- [71] W.J. Barnes and F.P. Price. Morphology of polymer crystals: Screw dislocations in polyethylene, polymethylene oxide and polyethylene oxide. *Polymer*, 5(0):283 – 292, 1964.
- [72] D. Breuer, P. Klimanek, and W. Pantleon. X-ray determination of dislocation density and arrangement in plastically deformed copper. *J. Appl. Crystallogr.*, 33:1284–1294, 2000.
- [73] A. Galeski, Z. Bartczak, T. Kazmierczak, and M. Slouf. Morphology of undeformed and deformed polyethylene lamellar crystals. *Polymer*, 51(24):5780–5787, November 2010.
- [74] R. Séguéla. Dislocation approach of the plastic deformation of semicrystalline polymers: Kinetic aspects for polyethylene and polypropylene. *J. Polym. Sci., Part B: Polym. Phys.*, 40:593–601, 2002.
- [75] D. Hull and D.J. Bacon. *Introduction to Dislocations*. Elsevier Science, 2001.
- [76] N. W. J. Brooks and M. Mukhtar. Temperature and stem length dependence of the yield stress of polyethylene. *Polymer*, 41(4):1475–1480, February 2000.
- [77] Richard H. Boyd. Relaxation processes in crystalline polymers: molecular interpretation — a review. *Polymer*, 26(8):1123 – 1133, 1985.
- [78] R Séguéla, V Gaucher-Miri, and S Elkoun. Plastic deformation of polyethylene and ethylene copolymers: Part i homogeneous crystal slip and molecular mobility. *J. Mater. Sci.*, 33(5):1273–1279, March 1998.
- [79] Kevin P. Menard. *Dynamic Mechanical Analysis: A Practical Introduction*. Taylor & Francis, 2008.
- [80] Leslie Howard Sperling. *Introduction to physical polymer science*. John Wiley & Sons, 2015.
- [81] I.M. Ward and J. Sweeney. *An Introduction to the Mechanical Properties of Solid Polymers*. Wiley, 2004.
- [82] JoelR. Fried. Sub-tg transitions. In JamesE. Mark, editor, *Physical Properties of Polymers Handbook*, pages 217–232. Springer New York, 2007.
- [83] Hongyi Zhou and Garth L. Wilkes. Orientation anisotropy of the mechanical  $\alpha$  relaxation of high-density polyethylene films having a well-defined stacked lamellar morphology. *Macromolecules*, 30(8):2412–2421, 1997.

- [84] Mario Hoyos, Pilar Tiemblo, and José Manuel Gómez-Elvira. The role of microstructure, molar mass and morphology on local relaxations in isotactic polypropylene. the  $\alpha$  relaxation. *Polymer*, 48(1):183 – 194, 2007.
- [85] E. Suljovrujic, S. Trifunovic, and D. Milicevic. The influence of gamma radiation on the dielectric relaxation behaviour of isotactic polypropylene: The  $\alpha$  relaxation. *Polymer Degradation and Stability*, 95(2):164 – 171, 2010.
- [86] Z. H. Stachurski and I. M. Ward. Mechanical relaxations in polyethylene. *Journal of Macromolecular Science, Part B*, 3(3):445–494, 1969.
- [87] R. G. Matthews, A. P. Unwin, I. M. Ward, and G. Capaccio. A comparison of the dynamic mechanical relaxation behavior of linear low- and high-density polyethylenes. *Journal of Macromolecular Science, Part B*, 38(1-2):123–143, 1999.
- [88] D. H. Reneker, B. M. Fanconi, and J. Mazur. Energetics of defect motion which transports polyethylene molecules along their axis. *Journal of Applied Physics*, 48(10):4032–4042, 1977.
- [89] Marc Mansfield and Richard H. Boyd. Molecular motions, the  $\alpha$  relaxation, and chain transport in polyethylene crystals. *Journal of Polymer Science: Polymer Physics Edition*, 16(7):1227–1252, 1978.
- [90] S. A. Jawad and M. H. Alhaj-Mohammad.  $\beta$ -relaxation of drawn isotactic polypropylene in terms of a simplified two phase model. *Polymer International*, 35(4):395–398, 1994.
- [91] Raymond F. Boyer. The relation of transition temperatures to chemical structure in high polymers. *Rubber Chemistry and Technology*, 36(5):1303–1421, 1963.
- [92] TF Schatzki. Glass transitions in ethylene copolymers. *J. Polym. Sci*, 57:496–498, 1962.
- [93] Howard W. Starkweather, Peter Avakian, Robert R. Matheson, John J. Fontanella, and Mary C. Wintersgill. Ultralow temperature dielectric relaxations in polyolefins. *Macromolecules*, 25(25):6871–6875, 1992.
- [94] J Brandrup and EH. Immergut. Polymer handbook. *New York: Wiley*, 1975.
- [95] G.W. Ehrenstein, G. Riedel, and P. Trawiel. *Praxis der thermischen Analyse von Kunststoffen*. Hanser, 2003.
- [96] B. Wunderlich. The heat capacity of polymers. *Thermochimica Acta*, 300(1–2):43 – 65, 1997. A Collection of Invited Papers in Celebration of Volume 300.

- [97] John D. Hoffman, G. Thomas Davis, and Jr. Lauritzen, John I. The rate of crystallization of linear polymers with chain folding. In N.B. Hannay, editor, *Treatise on Solid State Chemistry*, pages 497–614. Springer US, 1976.
- [98] B. E. Warren and B. L. Averbach. The separation of cold-work distortion and particle size broadening in x-ray patterns. *J. Appl. Phys.*, 23(4):497–497, April 1952.
- [99] B. E. Warren and B. L. Averbach. The effect of cold-work distortion on X-ray patterns. *J. Appl. Phys.*, 21(6):595–599, June 1950.
- [100] M.A. Krivoglaz. *Theory of X-Ray and Thermal Neutron Scattering by Real Crystals*. Plenum Press, 1969.
- [101] M. Wilkens. The determination of density and distribution of dislocations in deformed single crystals from broadened X-ray diffraction profiles. *Phys. Status Solidi A*, 2(2):359–370, 1970.
- [102] M. Wilkens. X-ray line broadening and mean square strains of straight dislocations in elastically anisotropic crystals of cubic symmetry. *Phys. Status Solidi A*, 104(1):K1–K6, 1987.
- [103] G. Ribárik, T. Ungár, and J. Gubicza. *MWP-fit*: a program for multiple whole-profile fitting of diffraction peak profiles by *ab initio* theoretical functions. *Journal of Applied Crystallography*, 34(5):669–676, Oct 2001.
- [104] T. Ungár and G. Tichy. The effect of dislocation contrast on X-ray line profiles in untextured polycrystals. *Phys. Status Solidi A*, 171(2):425–434, 1999.
- [105] G. K. Williamson and W. H. Hall. X-ray line broadening from filed aluminium and wolfram. *Acta Metallurgica*, 1(1):22–31, January 1953.
- [106] I. Groma. X-ray line broadening due to an inhomogeneous dislocation distribution. *Phys. Rev. B*, 57(13):7535–, April 1998.
- [107] I. Groma and F. Szekely. Analysis of the asymptotic properties of x-ray line broadening caused by dislocations. *Applied Crystallography*, 33:1329–1334, 2000.
- [108] A. Borbely and I. Groma. Variance method for the evaluation of particle size and dislocation density from x-ray bragg peaks. *Applied Physics Letters*, 79(12):1772–1774, September 2001.

- [109] A.J.C. Wilson. The effects of dislocations on x-ray diffraction. *Il Nuovo Cimento (1955-1965)*, 1(2):277–283, 1955.
- [110] A J C Wilson. On variance as a measure of line broadening in diffractometry general theory and small particle size. *Proceedings of the Physical Society*, 80(1):286–, 1962.
- [111] H. Amenitsch, S. Bernstorff, and P. Laggner. High flux beamline for small angle x-ray scattering at elettra. *Review of Scientific Instruments*, 66(2):1624–1626, 1995.
- [112] A P Hammersley. Esrf98ha01t , fit2d v9.129 reference manual v3.1. Technical report, ESRF Internal Report, 1998.
- [113] A. P. Hammersley, S. O. Svensson, M. Hanfland, A. N. Fitch, and D. Hausermann. Two-dimensional detector software: From real detector to idealised image or two-theta scan. *High Pressure Research*, 14(4-6):235–248, 1996.
- [114] A.P. Hammersley, S.O. Svensson, and A. Thompson. Calibration and correction of spatial distortions in 2d detector systems. *Nuclear Instruments and Methods in Physics Research Section A: Accelerators, Spectrometers, Detectors and Associated Equipment*, 346(1–2):312 – 321, 1994.
- [115] H. Wilhelm. Phd thesis, university of vienna, in preparation.
- [116] John W. Eaton, David Bateman, and Soren Hauberg. *GNU Octave version 3.0.1 manual: a high-level interactive language for numerical computations*. CreateSpace Independent Publishing Platform, 2009. ISBN 1441413006.
- [117] Jeff Racine. gnuplot 4.0: a portable interactive plotting utility. *Journal of Applied Econometrics*, 21(1):133–141, 2006.
- [118] Marcin Wojdyr. *Fityk*: a general-purpose peak fitting program. *Journal of Applied Crystallography*, 43(5 Part 1):1126–1128, Oct 2010.
- [119] Michael Kerber. *X-ray Line Profile Analysis in Theory and Experiment*. PhD thesis, University of Vienna, 2012.
- [120] R. de P. Daubeny and C. W. Bunn. The crystal structure of polyethylene terephthalate. *Proceedings of the Royal Society of London A: Mathematical, Physical and Engineering Sciences*, 226(1167):531–542, 1954.
- [121] X.F Lu and J.N Hay. Isothermal crystallization kinetics and melting behaviour of poly(ethylene terephthalate). *Polymer*, 42(23):9423 – 9431, 2001.

- [122] Aspy Mehta, Umesh Gaur, and Bernhard Wunderlich. Equilibrium melting parameters of poly(ethylene terephthalate). *Journal of Polymer Science: Polymer Physics Edition*, 16(2):289–296, 1978.
- [123] ER Walter and FP Reding. Variations in unit cell dimensions in polyethylene. *Journal of Polymer Science*, 21(99):561–562, 1956.
- [124] D.C. Bassett. Chain-extended polyethylene in context: a review. *Polymer*, 17(6):460 – 470, 1976.
- [125] D. C. Bassett and B. Turner. On the phenomenology of chain-extended crystallization in polyethylene. *Philosophical Magazine*, 29(4):925–956, 1974.
- [126] B.E. Read. Mechanical relaxation in isotactic polypropylene. *Polymer*, 30(8):1439 – 1445, 1989.
- [127] R.F. Boyer, D.J. Meier, Midland Macromolecular Institute, and Dow Chemical Company. *Molecular Basis of Transitions and Relaxations*. Midland macromolecular monographs. Gordon and Breach Science Publishers, 1978.
- [128] B.E. Read, G.D. Dean, and P.E. Tomlins. Effects of physical ageing on creep in polypropylene. *Polymer*, 29(12):2159 – 2169, 1988.
- [129] Óscar Prieto, José M. Pereña, Rosario Benavente, Ernesto Pérez, and María L. Cerrada. Viscoelastic relaxation mechanisms of conventional polypropylene toughened by a plastomer. *Journal of Polymer Science Part B: Polymer Physics*, 41(16):1878–1888, 2003.
- [130] A. Amash and P. Zugenmaier. Thermal and dynamic mechanical investigations on fiber-reinforced polypropylene composites. *Journal of Applied Polymer Science*, 63(9):1143–1154, 1997.
- [131] N.G. McCrum. The kinetics of the  $\alpha$  and  $\beta$  relaxations in isotactic polypropylene. *Polymer*, 25(3):299 – 308, 1984.
- [132] S. K. Roy, T. Kyu, and R. S. John Manley. Physical and dynamic mechanical properties of ultradrawn polypropylene films. *Macromolecules*, 21(2):499–504, 1988.
- [133] C. Jourdan, J. Y. Cavaille, and J. Perez. Mechanical relaxations in polypropylene: A new experimental and theoretical approach. *Journal of Polymer Science Part B: Polymer Physics*, 27(11):2361–2384, 1989.

- [134] Li Yin, Jianfeng Chen, Xiaoniu Yang, and Enle Zhou. Structure image of single crystal of polyethylene. *Polymer*, 44(21):6489–6493, October 2003.
- [135] D. Bacon and K. Tharmalingam. Computer simulation of polyethylene crystals. *J. Mater. Sci.*, 18(3):884–893, 1983.
- [136] T. Kazmierczak and A. Galeski. Transformation of polyethylene crystals by high-pressure annealing. *J. Appl. Polym. Sci.*, 86:1337–1350, 2002.
- [137] Phillip H. Geil, Franklin R. Anderson, Bernhard Wunderlich, and Tamio Arakawa. Morphology of polyethylene crystallized from the melt under pressure. *Journal of Polymer Science Part A: General Papers*, 2(8):3707–3720, 1964.
- [138] L. Melillo and B. Wunderlich. Extended-chain crystals. *Kolloid-Zeitschrift und Zeitschrift für Polymere*, 250(5):417–425, 1972.
- [139] L. J. Tung and S. Buckser. The effects of molecular weight on the crystallinity of polyethylene. *The Journal of Physical Chemistry*, 62(12):1530–1534, 1958.
- [140] R Bruce Prime and Bernhard Wunderlich. Extended-chain crystals. iii. size distribution of polyethylene crystals grown under elevated pressure. *Journal of Polymer Science Part A? 2: Polymer Physics*, 7(12):2061–2072, 1969.
- [141] E.J. Addink and J. Beintema. Polymorphism of crystalline polypropylene. *Polymer*, 2:185 – 193, 1961.
- [142] R. Anderson Campbell, J. S. Lin, and Paul J. Phillips. The  $\gamma$ -phase of high-molecular-weight polypropylene: 1. morphological aspects. *Polymer*, 34:4809–4816, 1993.
- [143] Stefano V. Meille, Paul J. Phillips, , Khaled Mezghani, and Sergio Brückner\*.  $\alpha - \gamma$  disorder in isotactic polypropylene crystallized under high pressure. *Macromolecules*, 29(2):795–797, 1996.
- [144] Finizia Auriemma and Claudio De Rosa. Crystallization of metallocene-made isotactic polypropylene: Disordered modifications intermediate between the  $\alpha$  and  $\gamma$  forms. *Macromolecules*, 35:9057–9068, 2002.
- [145] Yan Cao, Ryan M. Van Horn, Chi-Chun Tsai, Matthew J. Graham, Kwang-Un Jeong, Bojie Wang, Finizia Auriemma, Claudio De Rosa, Bernard Lotz, and Stephen Z. D. Cheng. Epitaxially dominated crystalline morphologies of the  $\gamma$ -phase in isotactic polypropylene. *Macromolecules*, 42:4758–4768, 2009.

- [146] K. Mezghani and P. J. Phillips. The  $\gamma$ -phase of high molecular weight isotactic polypropylene: Iii. the equilibrium melting point and the phase diagram. *Polymer*, 39(16):3735–3744, July 1998.
- [147] L.H. Sperling. *Introduction to Physical Polymer Science*. John Wiley & Sons, Inc. New York Chichester Brisbane Toronto Singapore, 1992.



# Appendix

## Program codes

Listing 8.1: fit\_PP.sh

```
1 #!/bin/bash
2
3 #generates a *.fit file for fityk in order to fit the individual peaks of a
  measured PP pattern
4
5 command -v xclip >/dev/null 2>&1 || { echo -e >&2 "The program \"xclip\" is
  required, please install:\n sudo apt-get install xclip\n Aborting.";
  exit 1;} #check if the program xclip is installed
6
7 if [[ $# != 1 ]] ;then
8   echo "Usage: $0 DatafileFile "
9   exit 1
10 fi
11
12
13 fitykfile=fit_PP.fit
14 gnuplotfile=toplot.gnu
15 wdir=`pwd`
16 #datafiles=()
17 #datafiles=( `zenity --file-selection --filename="$pwd" --title="Select
  data Files" ` )
18 datafiles=$1
19
20
21 if [[ -e "$~/.fityk/configs/agiPP_color" ]]; then #check if fityk config
  file exists
22   break
23   else
24     cp $wdir/agiPP_color ~/.fityk/configs/
```

```

25 fi
26
27 delta_bgnodes=0.1
28 bgnodes=()
29
30
31
32 echo -e "@+ <'$1'" >> $fitykfile
33 echo -e "@0: delete(y<100)" >> $fitykfile #delete all data points less than
    100"
34 echo -e "@0: print all: x, y > '$wdir/$1_temp'" >> $fitykfile
35
36 cfityk -q $fitykfile
37
38 mv $1_temp $1
39 rm $fitykfile
40
41 exec 3>&1
42 exec 1>$gnuplotfile
43
44 echo "set term wxt"
45 echo "set mouse doubleclick 0"
46 echo "set mouse mouseformat \"background node = %5.2f, (Intensity=%10.2f),
    single click on background to use it as node\" "
47 echo "set mouse clipboardformat \"%2.2f\" "
48 echo "plot \"./$1\" w l"
49
50 exec 1>&3 3>&-
51
52 gnuplot -p $gnuplotfile
53 clear
54 echo "Choose 2theta values for the background-nodes by single clicking (
    ENTER...next node, (c)ontinue, (q)uit)"
55
56 while true; do
57 read -p "" node
58
59 if [ "$node" == "q" ]; then
60 echo -e "Program closed"
61 exit 0
62 elif [ "$node" == "c" ]; then
63 echo -e "Following background-nodes are used: ${bgnodes[@]}"
64 break

```

```
65     else
66     node='xclip -out -selection c'
67     bgnodes+=$(node)
68     fi
69     echo -e "Background nodes: ${bgnodes[@]}"
70 done
71
72 #FIXME make preview in gnuplot by fitting polynomial
73
74 exec 3>&1
75 exec 1>$fitykfile
76
77 echo -e "# Import File"
78 echo -e "@+ <'$1'"
79
80 echo -e "#delete all data points less than 100"
81 echo -e "@0: delete(y<100)"
82
83 echo -e "#find minimum of data File ( use only y values larger than 3000)"
84 echo -e "#@0: \${mindat}=min(y if x<14)"
85
86
87 echo -e "#set initial (peak)-parameters"
88 echo -e "\$hwhm=0.12"
89 echo -e "\$dx=0.2"
90 echo -e "\$xscale=0.9"
91
92 echo -e "A = a and not a #deselect all"
93
94 for i in ${bgnodes[@]}; do
95     echo -e "A = a or ( $i-$delta_bgnodes < x and x < $i+$delta_bgnodes )"
96 done
97
98
99 echo -e "guess Polynomial5"
100
101 echo -e "fit"
102
103 echo -e "# fix background parameters"
104 echo -e "\$_1 = {\$_1}"
105 echo -e "\$_2 = {\$_2}"
106 echo -e "\$_3 = {\$_3}"
107 echo -e "\$_4 = {\$_4}"
```

```

108 echo -e "\$_5 = {\$_5}"
109 echo -e "\$_6 = {\$_6}"
110
111
112 echo -e "#g111"
113 echo -e "\$g111_x_max=argmax(y if x > 13.4 and x < 15.0) #find the x value
      of the first peak maximum (should correspond to a110 or g111) and use
      it as reference position"
114 echo -e "\$g111_y_max=max(y if x > 13.4 and x < 15.0)"
115 echo -e "%g111 = Pearson7(height=~{\$g111_y_max*0.8}, hwhm=~{\$hwhm},
      center=~{\$g111_x_max})"
116 echo -e "F += %g111"
117
118
119 echo -e "#a110"
120 echo -e "\$a110_y_max=\$g111_y_max"
121 echo -e "%a110 = Pearson7(height=~{\$a110_y_max*0.8}, hwhm=~{\$hwhm},
      center=~{\$g111_x_max+0.29*\$xscale})"
122 echo -e "F += %a110"
123
124 echo -e "#g113"
125 echo -e "\$g113_y_max=max(y if x > \$g111_x_max+1.21-\$dx and x < \
      \$g111_x_max+1.21+\$dx)"
126 echo -e "%g113 = Pearson7(height=~{\$g113_y_max*0.8}, hwhm=~{\$hwhm},
      center=~{\$g111_x_max+1.21*\$xscale})"
127 echo -e "F += %g113"
128
129 echo -e "#g008"
130 echo -e "\$g008_y_max=max(y if x > \$g111_x_max+2.87-\$dx and x < \
      \$g111_x_max+2.87+\$dx)"
131 echo -e "%g008 = Pearson7(height=~{\$g008_y_max*0.8}, hwhm=~{\$hwhm},
      center=~{\$g111_x_max+2.87*\$xscale})"
132 echo -e "F += %g008"
133
134 echo -e "#a040"
135 echo -e "\$a040_y_max=\$g008_y_max"
136 echo -e "%a040 = Pearson7(height=~{\$a040_y_max*0.8}, hwhm=~{\$hwhm},
      center=~{\$g111_x_max+3.07*\$xscale})"
137 echo -e "F += %a040"
138
139 echo -e "#a130"
140 echo -e "\$a130_y_max=max(y if x > \$g111_x_max+4.7-\$dx and x < \
      \$g111_x_max+4.7+\$dx)"

```

```

141 echo -e "%a130 = Pearson7(height=~{\$a130_y_max*0.8}, hwhm=~{\$hwhm},
      center=~{\$g111_x_max+4.70*\$xscale})"
142 echo -e "F += %a130"
143
144 echo -e "#g117"
145 echo -e "\$g117_y_max=max(y if x > \$g111_x_max+6.23-\$dx and x < \
      \$g111_x_max+6.23+\$dx)"
146 echo -e "%g117 = Pearson7(height=~{\$g117_y_max*0.8}, hwhm=~{\$hwhm},
      center=~{\$g111_x_max+6.23*\$xscale})"
147 echo -e "F += %g117"
148
149 echo -e "#g202"
150 echo -e "\$g202_y_max=max(y if x > \$g111_x_max+7.42-\$dx and x < \
      \$g111_x_max+7.42+\$dx)"
151 echo -e "%g202 = Pearson7(height=~{\$g117_y_max*0.4}, hwhm=~{\$hwhm},
      center=~{\$g111_x_max+7.42*\$xscale})"
152 echo -e "F += %g202"
153
154 echo -e "#a111"
155 echo -e "\$a111_y_max=\$g202_y_max"
156 echo -e "%a111 = Pearson7(height=~{\$a111_y_max*0.4}, hwhm=~{\$hwhm},
      center=~{\$g111_x_max+7.45*\$xscale})"
157 echo -e "F += %a111"
158
159 echo -e "#a13m1"
160 echo -e "\$a13m1_y_max=\$g202_y_max"
161 echo -e "%a13m1 = Pearson7(height=~{\$a13m1_y_max*0.4}, hwhm=~{\$hwhm},
      center=~{\$g111_x_max+7.97*\$xscale})"
162 echo -e "F += %a13m1"
163
164 echo -e "#g026"
165 echo -e "\$g026_y_max=\$g202_y_max"
166 echo -e "%g026 = Pearson7(height=~{\$g026_y_max*0.6}, hwhm=~{\$hwhm},
      center=~{\$g111_x_max+8.02*\$xscale})"
167 echo -e "F += %g026"
168
169
170 echo -e "A = a or (1. < x and x < 55.)"
171 echo -e "plot [][]"
172
173
174 exec 1>&3 3>&-
175

```

```

176 #shotwell ./a_g_iPP_PEAKS.png &
177 fityk -g agiPP_color $fitykfile 2>/dev/null
178
179 rm $gnuplotfile $fitykfile

```

**Listing 8.2:** peak\_subtraction.sh

```

1 #!/bin/bash
2
3 # Generates a Script for fityk to subtract the here entered functions from
  the datafile
4
5 fitykscript=subpeak.fit
6 finalpattern=export_$1
7 wdir=`pwd` #working directory
8
9
10 #check if Script is used right
11
12 if [[ $# != 2 ]] ;then
13     echo "Usage: $0 DatafileFile session.fit-File "
14     exit 1
15 fi
16
17
18 #check if fitykscript does already exist
19
20 if [ ! -f ./ $fitykscript ]; then #if file subpeak does not exist, then ...
21     touch $fitykscript #generate fityk script with the functions to
  subtract
22 else
23     echo "File $fitykscript does already exist, overwrite? (\\"y\\" for yes)";
  read question1;
24     if [ "$question1" == "y" ]; then
25         >$fitykscript #empty the fitykscript
26     fi
27 fi
28
29
30 echo -e "@+ < '$1'" >> $fitykscript #import data
31 echo -e "exec '$2'" >> $fitykscript #execute *session.fit file to the
  corresponding diff pattern from $1
32

```

```

33 peakarray=() #define array
34
35 echo -e "Use Peaklist? ('y' for yes)"; read question2
36 #FIXME put the peaklist in fixed folder and use it if yes is pressed
37 if [ "$question2" == "y" ]; then
38     #peakarray=( 'cat "$wdir/peaklist.dat"' ) #Use this option if the
        peaklist is already in the current folder
39     peaklist=( 'zenity --file-selection --filename="$pwd" --title="Select
        data Files"' )
40     #peakarray=( 'cat "$peaklist"' )
41 else
42
43     while true; do
44
45         echo -n "Enter Peaknames to subtract and press 'Enter' ('c' for continue ,
            'q' for exit Program):"; read Name;
46         if [ "$Name" == "c" ]; then                #if "c" is pressed the program
            exits the if loop
47             echo -e "Peaks to subtract: \n'echo ${peakarray[@]}'"
48             break
49         elif [ "$Name" == "q" ]; then                #The program exits when
            pressing q
50             echo -e "Program closed"
51             exit 0
52         else
53             peakarray+=($Name)                #add peakname to the array
54         fi
55     done
56 done
57
58 fi
59
60
61 for i in ${peakarray[@]}; do
62     echo -e "Y=y-%$i(x) \n" >> $fitykscrip
63     echo -e "delete %$i \n" >> $fitykscrip
64 done
65
66 echo -e "@0: print all: x, y > '$wdir/$finalpattern'" >> $fitykscrip #
        Export subtracted profile to working directory
67 #echo -e "@0: print all: x, F(x) > '$wdir/$finalpattern'" >> $fitykscrip
        #Export the remaining !!MODELLED PHASE!!
68

```

```

69 #fityk $fitykscript 2>/dev/null #oppress error messages
70 cfityk -q $fitykscript
71
72
73 #plot the subtracted profile with gnuplot
74 echo "plot \"./$1\" w p lc 2 title \"data\", \"./$1\" w l lc 2 notitle \"
    data\", \"./$finalpattern\" w l lc 1 title \"modeled phase\" " | gnuplot
    -p
75
76 echo "_____ "
77 echo "DONE..."
78
79 rm $fitykscript
80
81 exit 0

```

**Listing 8.3:** prepare\_peak\_index.sh

```

1 #!/bin/bash
2
3
4 if [[ $# != 1 ]] ;then
5     echo "Usage: $0 Fityk *.peaks-File "
6     exit 1
7 fi
8
9 #wdir=pwd #working directory
10 #filename=hd120mo25_e86ln
11
12 #touch $1_NaN
13 sed -e "s/x/NaN/g" $1 > $1_NaN
14 mv $1_NaN $1
15 cat $1 | grep %a > $1_phase_temp
16 cat $1_phase_temp | cut -f2,3 > $1_center_height
17 cat $1_phase_temp | cut -d\ -f1 | cut -c 3- > $1_hkl
18 paste $1_center_height $1_hkl > ./${(basename "$1" .peaks)}.peak-index.dat
19 rm $1_phase_temp $1_center_height $1_hkl

```

**Listing 8.4:** grep\_fitparams\_from\_wh.sh

```

1 #!/bin/bash
2
3 #extract contrast factors from the williamson_hall_analysis*.dat for each
  profile and save them in a seperate file for the use of MBK
4 #Author: Gerald Polt
5 #Version: 0.0.1
6 #usage: grep_fitparams_from_wh <File>
7
8
9 #extract contrast factors from the williamson_hall_analysis*.dat for each
  profile and save them in a seperate file for the use of Multieval with
  deformation steps in filename
10
11 if [[ $# != 1 ]] ;then                #Check if script is used right
12     echo "Usage: $0 File "
13     exit 1
14 fi
15
16 #grep contrast fit parameters a1–an ($4–$n) and save them in temp file:
17 cat $1 | egrep -v "#l^$" | awk 'BEGIN { FS=" " } {print "a1="$4, "a2="$5, "
  a3="$6, "a4="$7, "a5="$8}' > $1.tmp #l sed 's/e+/*10^/g'
18
19 #grep first column (deformation steps) save them in profile.txt
20 cat $1 | egrep -v "#l^$" | awk 'BEGIN { FS=" " } {print $1*100}' | bc >
  profiles.txt
21
22 #declare an array profiles out of file profiles.txt
23 declare -a profiles
24 profiles=( `cat "profiles.txt"` )
25
26 FILE=$1.tmp
27         # read $FILE using the file descriptors
28 exec 3<&0
29 exec 0<$FILE
30
31 l=$(cat profiles.txt | head -n 1)      #first *temp file will be named after
  the first deformation step
32 v=1
33
34 while read line                        #read one line from the tmp file
35 do

```

```

36 echo $line >> $1.tmp          # use $line variable to process line
37 l=$(( ${profiles[0+$v]} ))    # use second element from array "
    profiles" to create file *.temp
38 v=$(( $v + 1 ))
39 done
40 exec 0<&3
41
42
43 rows=$(awk '{print NF}' ${profiles[0]}.temp | sort -nu)    #count number
    of rows from first *.temp file (can only be five according to cat $1 ...
44
45 #linenumber=$(cat $1.tmp | wc -l)    #count number of lines
46
47
48
49 echo -n "Please type in the Header-String inkl. _:"
50 read Header
51 echo -n "Please type in the Tail-String (e.g. _filename.dat.ini.fix) :"
52 read Tail
53
54
55 for j in `seq 1 1 $rows`        #make lines to rows for each file
56 do for k in ${profiles[@]}
57 do cat $k.temp | cut -d' ' -f$j | paste -s >> $Header${k}$Tail #list
    *.temp file | cut row j and save to Heade... paste command
    is optional
58 done
59 done
60
61
62
63 rm *.temp $1.tmp profiles.txt

```

# List of Abbreviations

$T_g$	Glass transition temperature
AFM	Atomic Force Microscopy
CMWP-fit	Convolutional Multiple Whole Profile fitting
CRSS	Critical Resolved Shear Stress
CSD-size	Coherently Scattering Domain-size
DMA	Dynamic Mechanical Analysis
DMTA	Dynamic Mechanical Thermal Analysis
DSC	Differential Scanning Calorimetry
DTA	Differential Thermal Analysis
FWHM	Full Width at Half Maximum
HDPE	High Density Polyethylene
iPP	Isotactic polypropylene
iPS	isotactic Polystyrene
LDPE	Low Density Polyethylene
LN2	Liquid Nitrogen
MFR	Melt Flow Rate
M <sub>w</sub>	Molecular weight
MWH	Modified Williamson-Hall

MXPA	Multireflection X-ray Profile Analysis
P3HB	Poly(3-hydroxybutyrate)
PE	Polyethylene
PET	polyethylene terephthalate
POM	Polyoxymethylene
PP	Polypropylene
SAXS	Small Angle X-ray Scattering
SEM	Scanning Electron Microscope
WAXS	Wide Angle X-ray Scattering
WH	Williamson-Hall
X <sub>c</sub>	Crystallinity
XLPA	X-ray Line Profile Analysis

# List of Figures

3.1	Morphological hierarchy of a semicrystalline polymer . . . . .	6
3.2	Optical micrograph of spherulites . . . . .	6
3.3	Electron micrograph of a thin $\alpha$ -iPP film . . . . .	7
3.4	Unit cell packing of $\gamma$ -iPP . . . . .	7
3.5	Transition points of the stress strain curve of a semicrystalline polymer. . . . .	8
3.6	Plastic deformation mechanisms in semicrystalline polymers . . . . .	9
3.7	Deformation modes of the amorphous phase within a spherulite . . . . .	10
3.8	Microfibrils pulled out at the crack of polyoxymethylene (POM) single crystals	12
3.9	Peterlin's micronecking model . . . . .	12
3.10	Schmid's law . . . . .	14
3.11	Possible types of slip within a lamella . . . . .	14
3.12	Coarse slip and fine slip . . . . .	15
3.13	Scheme of an edge dislocation . . . . .	17
3.14	Scheme of a screw dislocation . . . . .	17
3.15	Yield stress as a function of stem length . . . . .	20
3.16	Complex modulus . . . . .	23
3.17	Propagation of a chain twist defect . . . . .	25
3.18	Shortening of chain loops by reorganization of the crystal interface . . . . .	25
3.19	Three and five bond crankshaft motion . . . . .	26
4.1	Compression chamber used for the production of $\gamma$ -samples . . . . .	28
4.2	Construction drawing of the compression chamber . . . . .	28

4.3	Miniature compression machine . . . . .	28
4.4	Heating stage mounted to the vacuum chamber . . . . .	28
4.5	Inel detector used in the synchrotron setup . . . . .	34
4.6	Two dimensional Pilatus detector . . . . .	34
4.7	Raw data of $\alpha$ -iPP recorded with the <i>PILATUS</i> detector . . . . .	35
4.8	Integrated raw data . . . . .	35
5.1	Sample stage nounted to the EPS block . . . . .	38
5.2	Sample mounted to the stage in a bath of liquid nitrogen . . . . .	38
5.3	Cooled sample stage mounted to the EPS block . . . . .	39
5.4	Transmission setup . . . . .	39
5.5	Waterfall plot of diffraction patterns at different annealing temperatures . . . . .	40
5.6	Diffraction patterns as function of annealing temperature and peak shift . . . . .	40
5.7	The development of the dislocation density as a function of annealing temperature	41
5.8	Development of the domain size as a function of the annealing temperature for $\alpha$ -iPP . . . . .	41
5.9	. . . . .	42
5.10	Loss and storage modulus measured at test frequencies of 0.5, 1 and 10 Hz . . . . .	42
5.11	DSC traces of PET after different processing conditions . . . . .	44
5.12	Diffraction patterns of PET at different annealing temperatures . . . . .	44
5.13	Dislocation density development in PET . . . . .	45
5.14	Development of the CSD-size in PET . . . . .	45
5.15	WAXS pattern of undeformed iPP below $T_g$ . . . . .	47
5.16	WH and MWH-plot for the undeformed and deformed sample cooled below $T_g$	48
5.17	WH and MWH-plot for the undeformed and deformed sample above $T_g$ . . . . .	48
5.18	Development of the dislocation density of $\alpha$ -iPP at room temperature and below its glass transition . . . . .	49
5.19	Coherently scattering domain size (CSD-size) as a function of true strain . . . . .	49

5.20	Comparison of diffraction patterns obtained for the undeformed and highly strained PE sample . . . . .	50
5.21	Development of the second order moment for different true strains. . . . .	51
5.22	Development of the fourth order moment divided by $q^2$ for different degrees of deformation. . . . .	51
6.1	Comparison of the loss tangent signal and the evolution of the dislocations density as a function of annealing temperature . . . . .	54
6.2	Propagation of a chain twist defect . . . . .	55
6.3	Shortening of chain loops by reorganization of the crystal interface . . . . .	55
6.4	Loss factor curves for the undeformed and deformed samples . . . . .	56
6.5	Storage modulus measured at different frequencies . . . . .	56
6.6	Loss tangent versus temperature of deformed samples for different test frequencies	58
6.7	Arrhenius plot of the $\alpha$ and $\beta$ -relaxation for the undeformed and deformed samples. . . . .	58
6.8	Development of the domain size as a function of the annealing temperature for $\alpha$ -iPP . . . . .	59
6.9	Comparison of the evaluation methods, MXPA and WH . . . . .	60
6.10	CSD-size and dislocation density development in PET . . . . .	60
6.11	Development of the dislocation density of $\alpha$ -iPP at room temperature and below its glass transition . . . . .	62
6.12	Effect of relative intensity on the development of the fourth order restricted moment . . . . .	65
6.13	BGR for the (110) reflection as a function of true strain . . . . .	65
6.14	Effect of varying dislocation densities and crystallite sizes on the second order moment . . . . .	67
6.15	Development of the second order moment for different true strains. . . . .	67
6.16	Development of the fourth order moment divided by $q^2$ for different degrees of deformation. The logarithmic development points at the presence of dislocations.	68
6.17	Effect of varying dislocation densities and crystallite sizes on the fourth order moment . . . . .	68

8.1	Applied temperature program for the production of $\gamma$ -iPP samples. . . . .	77
8.2	Theoretical phase diagram for PP for temperature as a function of pressure . . .	78
8.3	Diffraction patterns of high pressure crystallized PP samples with different molecular weight for (a) DM55Pharm, (b) HD120MO and (c) HF700SA. . . . .	79
8.4	WAXS pattern of iPP with similar amounts of $\alpha$ and $\gamma$ -phase . . . . .	80
8.5	Amount of $\gamma$ -phase as a function of molecular weight . . . . .	81
8.6	Obtained crystalline volume fractions $X_c$ for the different types of PP . . . . .	81
8.7	Diffraction patterns of PP crystallized at different pressures . . . . .	81
8.8	$\gamma$ -phase content as a function of applied pressure during crystallization . . . . .	81
8.9	Schematic drawing of a lamellar crystal . . . . .	83

# List of Tables

5.1	Lamellae thickness, crystallinity and glass transition for PET before and after annealing obtained by DSC . . . . .	43
6.1	Comparison of activation energies for the $\alpha$ and $\beta$ -relaxation process in polypropylene. . . . .	57
6.2	Activation energies for the $\alpha$ - and $\beta$ -relaxation for the undeformed and deformed sample . . . . .	58
8.1	$\gamma$ -fraction and crystallinity obtained by different processing conditions at 200 MPa . . . . .	81



# Curriculum Vitae

**Mag. rer. nat. Gerald Polt**

Date of birth: March 1, 1984

Place of birth: Eisenstadt, Austria

## Education

- since 2011     Doctorate studies at University of Vienna, Faculty of Physics
- 2005 – 2011   Diploma studies in Physics at University of Vienna, diploma thesis entitled “Mechanisms of Plastic Deformation in  $\gamma$ -Isotactic Polypropylene”
- 1999 – 2004   Secondary College for Mechanical Engineering – Special Training Focus: Aeronautical Engineering *HTL-Flugtechnik - Eisenstadt*
- 1998 – 1999   Secondary College for Mechanical Engineering – Special Training Focus: Materials Engineering *HTL-Werkstofftechnik -Eisenstadt*
- 1994 – 1998   Grammar School, Bundesrealgymnasium, Eisenstadt
- 1990 – 1994   Elementary School, Volksschule, St. Margarethen

## Professional experience

- since 09/2015       Employed at “Isosport - Innovative Plastics Solutions” - Research and Development Department
- 03/2011 – 09/2014   Research associate at the University of Vienna within the FWF Project “Dislocations in Semicrystalline Polymers”
- 08/2009             Employee at Laboratory for Polymer Engineering LKT-TGM, Vienna

**Publications**

1. Polt G., Spieckermann F., Wilhelm H., Fischer Chr., Schafler E., Bernstorff S., Zehetbauer M., Crystalline Plasticity In Isotactic Polypropylene Below And Above the Glass Transition Temperature, *express Polymer Letters*, 2015, 9, 894–900; DOI: 10.3144/expresspolymlett.2015.81
2. Failamani F., Grytsiv A., Giester G., Polt G., Heinrich P., Michor H., Bauer E., Zehetbauer M., Rogl P., Ba<sub>5</sub>V,Nb<sub>12</sub>Sb<sub>19+x</sub>, novel variants of the Ba<sub>5</sub>Ti<sub>12</sub>Sb<sub>19+x</sub>-type: crystal structure and physical properties *Phys. Chem. Chem. Phys.*, The Royal Society of Chemistry, 2015, 17, 24248-24261; DOI: 10.1039/C5CP04000K
3. Zare Ghomsheh M., Spieckermann F., Polt G., Wilhelm H., Zehetbauer M., Analysis of strain bursts during nanoindentation creep of high density polyethylene, *Polymer International*, John Wiley and Sons, Ltd, 2015, 64, 1537-1543; DOI: 10.1002/pi.4967
4. Spieckermann F., Wilhelm H., Polt G., Ahzi S., Zehetbauer M., Rate mechanism and dislocation generation in high density polyethylene and other semicrystalline polymers, *Polymer*, 2014, 55, 1217 - 1222; DOI: 10.1016/j.polymer.2014.01.020
5. Polt G., Spieckermann F., Wilhelm H., Kerber M., Schafler E., Bernstorff S., Zehetbauer M., The role of dislocations in  $\gamma$ -iPP under plastic deformation investigated by X-ray line profile analysis, *Mechanics of Materials*, 2013, 67, 126 - 132; DOI: 10.1016/j.mechmat.2013.05.010
6. Spieckermann F., Polt G., Wilhelm H., Kerber M., Schafler E., Zehetbauer M. J., The role of dislocations for the plastic deformation of semicrystalline polymers as investigated by multireflection X-ray line profile analysis, *J. Appl. Polym. Sci.*, Wiley Subscription Services, Inc., A Wiley Company, 2012, 125, 4150-4154; DOI: 10.1002/app.36570
7. Spieckermann F., Wilhelm H., Kerber M., Schafler E., Polt G., Bernstorff S., Addiego F., Zehetbauer M., Determination of lamella thickness distributions in isotactic polypropylene by X-ray line profile analysis, *Polymer*, 2010, 51, 4195-4199; DOI: 10.1016/j.polymer.2010.07.009

**Conference contributions****Talks**

- 24/09/2014 6<sup>th</sup> International Conference on Polymer Behavior (ICPB6) “Thermal Stability of Deformation Induced Dislocations in PP”, Vienna, Austria
- 10/09/2013 Advances in Polymer Science and Technology (APST) 3 “The thermal stability of dislocations in  $\alpha$  – phase polypropylene”, Linz, Austria
- 15/10/2012 5<sup>th</sup> International Conference on Polymer Behavior (ICPB5) “Dislocation kinetics in plastically deformed alpha and gamma Polypropylene”, Aveiro, Portugal
- 24/08/2012 16<sup>th</sup> International Conference on Strength of Materials (ICSMA 16) “Dislocation Contrast Factors of Semicrystalline Polymers”, Bangalore, India
- 22/09/2011 European Materials Research Society (E-MRS) 2011 Fall Meeting Symposium C “Micromechanisms of plastic deformation in gamma-isotactic polypropylene”, Warsaw, Poland
- 22/09/2010 4<sup>th</sup> International Conference on Polymer Behavior (ICPB4) “Mechanisms of Plasticity in  $\gamma$ -Polypropylene”, Lodz, Poland

**Poster presentations**

- 11/03/2013 8<sup>th</sup> European NESY Winter-School and Symposium on Neutrons and Synchrotron Radiation “Investigating the thermal stability of dislocations in semicrystalline polymers using synchrotron radiation“, Planneralm, Austria
- 20/08/2012 16<sup>th</sup> International Conference on Strength of Materials (ICSMA 16) ”Plastic deformation and thermal stability of Polyethylene-Terephthalate (PET)“, Bangalore, India
- 03/04/2012 International Conference on Deformation, Yield and Fracture of Polymers (DYFP) 2012 ”Effects of dislocations in  $\gamma$ -phase polypropylene and comparison with other semi-crystalline polymers“, Kerkrade, Netherlands

**Conference organisation**

Member of the organizing committee of the 6<sup>th</sup> International Conference on Polymer Behavior (ICPB6), September 22–26, 2014, University of Vienna.



## Acknowledgements

This work would not have been possible without the strong support of my colleagues from the group Physics of Nanostructured Materials who assisted me in any kind of scientific problems. I greatly enjoyed the time being part of this wonderful team.

Especially thanked is Prof. Michael Zehetbauer for his precious support as the supervisor of this thesis, but also for many fruitful discussions. His knowledge of plasticity in general, but especially with respect to dislocation kinetics often led to new experimental approaches.

I am very grateful to Dr. Florian Spieckermann and Dipl.Ing. Harald Wilhelm who not only introduced me to the field of polymer science, but also offered me the possibility to join an enthusiastic and motivated polymer team. Without their strong support and ideas this work would have never reached this stage.

For additional assistance I want to thank Dr. Michael Kerber and Prof. Erhard Schafner for their help regarding the computer software and questions concerning X-ray Line Profile Analysis.

I want to pass my gratitude also to our recent members in the polymer team, Cornelia von Baeckmann and Mohammad Zare Ghomsheh who well supported my work through their skillness in some experiments and sample preparation.

Dr. Sigrid Bernstorff is thanked for her methodic advice during several synchrotron campaigns at the synchrotron light laboratory ELETTRA in Trieste, Italy.

I want to express my thanks to Mag. Marius Reinecker and Dr. Viktor Soprunyuk for their help with the DMA measurements, and to Prof. Alexander Bismarck for the possibility to use some measuring devices of his lab whenever I needed them.

I gratefully acknowledge the financial support from the FWF (Fonds zur Förderung der wissenschaftlichen Forschung – Austrian Science Fund) under project P22913 “Dislocations in Semicrystalline Polymers”.

I also want to thank Mrs Regina Pinter whose administrative skills prevented me in getting lost in paperwork.

Most importantly I have to thank my parents, my family and Daniela for their continuous support in every situation and reminding me in what is really important in life.

